Electromechanical Performance Comparison of Low-voltage Ride-through Methods for Variable Speed Wind Turbines

by

Andrew Zhou

A thesis submitted in partial fulfillment of the requirements for the degree of

Master of Science

in

Energy Systems

Department of Electrical and Computer Engineering
University of Alberta

Abstract

The increasing penetration of the renewable wind energy systems and the decommissioning of the traditional fuel systems has resulted in an increasingly strict grid codes to circumvent issues with the grid's stability and reliability. The low-voltage ride-through (LVRT) requirement is one of the most commonly enforced grid codes for variable speed wind turbines. The LVRT grid code requires wind turbines to be grid-connected during a fault to provide reactive power ancillary services and offer fast system restart once the fault is cleared. Today, the two most predominant variable speed wind turbines are the type 3 doubly-fed induction generator (DFIG) and the type 4 permanent magnet synchronous generator (PMSG). The DFIG is very popular in the industry because of its reduced converter rating, which results in higher efficiency and decreased converter costs. The PMSG is now growing in popularity because of its fully rated converter, which can decouple the machine dynamics from the grid. Because of the differences in the structure of these two types of wind turbine generators, they will respond differently to LVRT. For the PMSG, the main concern of LVRT is the charging of the DC-link because the grid power is significantly reduced, while the generator power remains almost unchanged. For the DFIG, the stator winding is directly connected to the grid; this means that when the grid voltage is suddenly reduced, the DFIG will experience severe transients because of its electrical dynamics resulting in large stator and rotor fault currents.

There are many LVRT solutions proposed for the PMSG and the DFIG, many of which will impact the mechanical drivetrain system resulting in additional stress. The main contribution of this research is the evaluation of the damage and the stress-life impact of these LVRT solutions. Operational and maintenance cost covers a significant portion of the capital investment of the wind turbine, so the additional stress resulting from LVRT may procure additional maintenance cost for the entire wind farm. Therefore, it essential to analyze the lifetime effects that may result from LVRT, so that wind turbine manufacturers and wind farm owners can

make a more informed financial decision when selecting the type of wind turbine to purchase and the LVRT method to implement to meet the grid code.

Preface

This thesis is an original work by Andrew Zhou. As detailed in the following, the research work described in some chapters of this thesis has been accepted or submitted for publication as a scholarly article in which Prof. Yunwei Li and Prof. Yasser A.-R. I. Mohamed are the supervisory authors and have contributed to concepts formation and the manuscript composition.

Materials in Chapters 3 of this thesis have been published as A. Zhou, Y. Li, and Y. Mohamed, "Mechanical Stress Comparison of PMSG Wind Turbine LVRT Methods," accepted in IEEE Transaction on Energy Conversion, August 2020.

Materials in Chapters 4 of this thesis have been submitted as A. Zhou, Y. Li, and Y. Mohamed, “Type 3 and Type 4 Wind Turbines Low-voltage Ride-through Overview and Electromechanical Performance Comparison,” to IET Renewable Power Generation, June 2020

Materials in Chapters 5 of this thesis have been published in "Mechanical Stress Comparison of PMSG Wind Turbine LVRT Methods," accepted in IEEE Transaction on Energy Conversion, August 2020 and submitted as “Type 3 and Type 4 Wind Turbines Low-voltage Ride-through Overview and Electromechanical Performance Comparison,” to IET Renewable Power Generation, June 2020

Acknowledgements

I would like to express my deepest appreciation to my M. Sc. supervisors, Professor Yunwei (Ryan) Li and Professor Yasser A.-R. I. Mohamed, for their continuous support and guidance. Their extensive knowledge and encouragement have helped me overcome many challenges throughout my research studies. It is my greatest honor to be a student under the guidance of Dr. Li and Dr. Mohamed.

I would also like to express my thanks to the lab members of Dr. Li's research group, as they have provided me with a lot of assistance with technical problems. Their expertise in electrical engineering has greatly enriched my M. Sc. research journey.

Finally, I would like to thank my parents for their continuous support and patience throughout my studies.

Table of Contents

List of Figures

List of Abbreviations

AC	Alternating current
BTB	Back-to-back
CSC	Current source converter
DC	Direct current
DCC	DC chopper
DFIG	Doubly-fed induction generator
DSO	Distribution system operator
EM	Electromagnetic
FCS	Finite-control-set
FEA	Finite element analysis
FOC	Field-oriented control
GCR	Grid code requirement
GL	Germanischer Lloyd
GSC	Grid side converter
LVRT	Low-voltage ride-through
MPC	Model predictive control
MPP	Maximum power point
MPPT	Maximum power point tracking
MSC	Machine-side converter
OMC	Operation and management cost
OTSR	Optimum tip speed ratio
PCC	Point of common coupling
PI	Proportional integral
PLL	Phase-locked loop
PMSG	Permanent magnet synchronous generator
RCB	Rotor crowbar
RFC	Rainflow counting
RSC	Rotor side converter
SCIG	Squirrel-cage induction generator

SEIRI	Stored energy in rotor inertia
SN	Stress-cycle
SPWM	Sinusoidal pulse width modulation
SRCB	Series rotor crowbar
SVM	Space vector modulation
SVOC	Stator voltage-oriented control
THD	Total harmonic distortion
TSO	Transmission system operator
TSR	Tip speed ratio
VOC	Voltage-oriented control
VSC	Voltage source converter
WECS	Wind energy conversion system
WT	Wind turbine
ZDC	Zero *d*-axis current

List of Symbols

C_{dc}	DC-link capacitance
V_{dc}	DC-link voltage
ΔP, P_{dc}	Power difference between MSC/RSC and GSC
V_{dcf}, t_f	Final DC-link voltage at the final time
V_{dc0}, t_0	Initial DC-link voltage at the initial time
J_t	Inertia of the turbine blade and hub
J_g	Inertia of the generator
ω_t	Turbine blade speed
ω_g	Generator speed
T_w	Wind turbine blade torque
T_s	Shaft torque
T_e	Electromagnetic torque
N_{gb}	Gearbox ratio
K_s	Cumulative shaft stiffness
D_s	Cumulative shaft mutual damping
θ_d	Angle of twist
W_h	Cumulative weight of the hub and the turbine blades
F_b	Normal force of the main bearing
F_g	Normal force of the generator
L_{hb}	Length between the center of mass of the hub to the main bearings
L_{bg}	Length between the main bearings and the gearbox
M_b	Bending moment
$M_{b,max}$	Maximum bending moment at the main bearing

σ	Bending stress
c	Vertical distance from the shaft's neutral axis
I	Area moment of inertia
K_f	Bending fatigue stress-concentration factor
τ	Torsional stress
r	Radial distance from the neutral axis
J	Polar moment of inertia
K_{fs}	Torsional fatigue stress-concentration factor
τ_a	Alternating torsional stress
τ_m	Midrange torsional stress
σ_a	Alternating bending stress
σ_m	Midrange bending stress
σ_a^{VM}	Alternating von Mise's stress
σ_m^{VM}	Midrange von Mise's stress
N	Number of cycles at a given alternating stress range
$\Delta\sigma_a$	Alternating stress range
$\Delta\sigma_e^*$	Modified endurance limit
N_e	Number of cycles before failure at the endurance limit
m_1	Logarithmic slope of the modified SN curve for stress ranges larger than $\Delta\sigma_e^*$
D_{ac}	Accumulated damage
$\Delta\sigma_i$	i^{th} stress range
n_i,	Measured number of stress cycle at the i^{th} stress range
N_i	Predicted number of stress cycle until failure for the i^{th} stress range
v_{sd}, v_{sq}	dq-axis stator voltages
i_{sd}, i_{sq}	dq-axis stator currents directed towards the MSC

L_{sd}, L_{sq}	dq-axis stator winding inductance
ω_r	Electrical rotor speed
λ_r	The rotor flux linkage produced by the rotor's permanent magnets
P	Number of pole pairs
v_{td}, v_{tq}	dq-frame GSC terminal voltages
i_{td}, i_{tq}	dq-frame GSC output current directed towards the grid
v_{gd},v_{gq}	dq-frame grid voltages
ω_{gr}	Grid frequency
R_g	GSC filter resistance
L_g	GSC filter inductance
V_{sd}, V_{sq}	dq-axis stator voltages in the Laplace domain
I_{sd}, I_{sq}	dq-axis stator currents in the Laplace domain
$\wp_{sd}$, $\wp_{sq}$	d- and q-axis stator current control loop plant model
D_{sd}, D_{sq}	d- and q-axis stator current control loop disturbances
ℓ_{sd}, ℓ_{sq}	d- and q-axis stator current open-loop gain
k_{ps}, k_{is}	Stator current PI control parameters
τ_i	Closed-loop time constant
g_s	MSC current control cost function
i^*_{sd}, i^*_{sq}	dq-axis stator current references
V_{td}, V_{tq}	dq-axis GSC terminal voltages in the Laplace domain
I_{gd}, I_{gq}	dq-axis grid currents in the Laplace domain
$\wp_{td}$, $\wp_{tq}$	d- and q-axis GSC current control loop plant model
D_{td}, D_{tq}	d- and q-axis GSC current control loop disturbances
ℓ_{td}, ℓ_{tq}	d- and q-axis GSC current open-loop gain
k_{ps}, k_{is}	GSC current PI control parameters
g_t	GSC current control cost function

i_{td}^*, i_{tq}^*	dq-axis GSC current references
P_w	Power that is extracted from the wind
C_p	Rotor efficiency
β	WT pitch angle
λ	Tip speed ratio
r_b	Turbine blade radius
ρ	Air density
v_w	Wind speed
λ_o	Optimal tip speed ratio
H_ω	Transfer function between the speed and EM torque
G_T	EM torque closed-loop gain
$\wp_\omega$	Generator speed plant model
ℓ_ω	Generator speed control open-loop gain
$k_{p\omega}$, $k_{i\omega}$	Generator speed PI control parameters
$\omega_{c\omega}$	Generator speed controller crossover frequency
P_t	GSC output power
P_s, Q_s	Stator output power and reactive power
P_g, Q_g	Grid power and reactive power
H_g	Transfer function between the DC-link voltage and the grid active power
G_p	Active grid power closed-loop gain
$\wp_g$	GSC controlled DC-link voltage plant model
ℓ_g	GSC controlled DC-link voltage open-loop gain
$\angle\ell_g$	Phase of the GSC controlled DC-link voltage open-loop gain
ω_{cv}	DC-link voltage controller crossover frequency
P_{ch}	Power dissipated by the DC chopper
R_{ch}	Chopper resistance

$\wp_{ch}$	DC chopper plant model
k_{pch}	DC chopper P control parameter
D	DC chopper duty cycle
$\wp_s$	MSC controlled DC-link voltage plant model
ℓ_s	MSC controlled DC-link voltage open-loop gain
$\angle\ell_g$	Phase of the MSC controlled DC-link voltage open-loop gain
P_{s0}	Normal operation WT power
α	Predetermined ratio used to obtained desired DCC power
P_{gdc}	DC component of the grid power
P_{gc}	Cosine sinusoidal component of the grid power
P_{gs}	Sine sinusoidal component of the grid power
v_{gd}^{+}, v_{gq}^{+}	Positive sequence *dq*-frame grid voltage
v_{gd}^{-}, v_{gq}^{-}	Positive sequence *dq*-frame grid voltage
i_{gd}^{+}, i_{gq}^{+}	Positive sequence *dq*-frame grid current
i_{gd}^{-}, i_{gq}^{-}	Negative sequence *dq*-frame grid current
V_0	Rated RMS grid voltage
I_0	Rated RMS grid current
P_0	Rated grid power
$P_{ch\text{Max}}$	Maximum DCC power
v_{rd}, v_{rq}	*dq*-axis rotor voltage
i_{rd}, i_{rq}	*dq*-axis rotor currents
λ_{sd}, λ_{sq}	*dq*-axis stator flux linkages
λ_{rd}, λ_{rq}	*dq*-axis rotor flux linkages
R_r	Rotor winding resistance
L_{ls}	DFIG stator leakage inductance
L_{lr}	DFIG rotor leakage inductance
L_m	DFIG magnetizing inductance

ω_{sl}	DFIG slip speed
ω_s	Stator frequency
g_r	RSC current control cost function
i^*_{rd} and i^*_{rq}	*dq*-axis rotor current reference values
P_r	Rotor power that is directed towards the rotor winding
P_{gr}	Grid power contributed from the rotor winding
g_{rcb}	Rotor crowbar control signal
P_{r0}	Normal operation rotor power
S_{SCB}	Switching state of the series rotor crowbar
R_{SCB}	Resistance of the series rotor crowbar

Chapter 1

Introduction

1.1 Background

Renewable energy is becoming increasingly important to reduce greenhouse gas emissions and to achieve sustainable energy for future generations. As of now, wind power plays a substantial role in achieving a sustainable carbon-free power system. Harnessing the power of the winds that are generated from the sun heating the Earth's surface, wind turbines convert the kinetic energy of wind into electrical energy, which makes it both a sustainable and a clean source of fuel [2], [3]. Wind turbines can even be placed offshore to minimize land occupation and to access faster and more consistent wind speeds [4].

Today, wind power is one of the fastest-growing renewable energy source having an upward trend in wind farm installations. In 2018, 51.3 GW of wind capacity had been installed for a total wind capacity of 591 GW [1]. Variable speed wind turbines (WTs) are the main contributors to wind power generation, and the two main types of variable speed WTs are the type 3 doubly-fed induction generators (DFIGs) and the type 4 permanent magnet synchronous generators (PMSGs). The stator winding of the DFIG is directly connected to the grid, while the rotor winding is interfaced to the grid with a wind energy conversion system (WECS), as shown in Fig 1.1. DFIGs are widely popular because the rotor winding power is about 30% of the total nominal power, so only a partially rated WECS is necessary for DFIGs, which leads to a higher efficiency and lower converter cost [5], [6]. In contrast, for the PMSG, the stator winding is interfaced to the grid using a fully rated WECS, as shown in Fig 1.2. Currently, the PMSG is growing in

popularity because the gearbox is not necessary by using direct drive PMSGs, and the generator and grid dynamics can be decoupled with the fully rated converter [7], [8].

However, a major flaw of wind renewable energy is that its power output is not as consistent as conventional fuel-based energy systems, which results in intermittency [9]. Without enough fuel-based energy systems to support renewable energy systems, these intermittencies will lead to fluctuations in the grid voltage. Therefore, the increasing penetration of renewable energy and the decommissioning of conventional fuel-based energy systems raises concerns regarding grid stability and reliability, so stricter grid codes must be set in place to facilitate the transition towards a renewable energy dominant energy system [7]–[9].

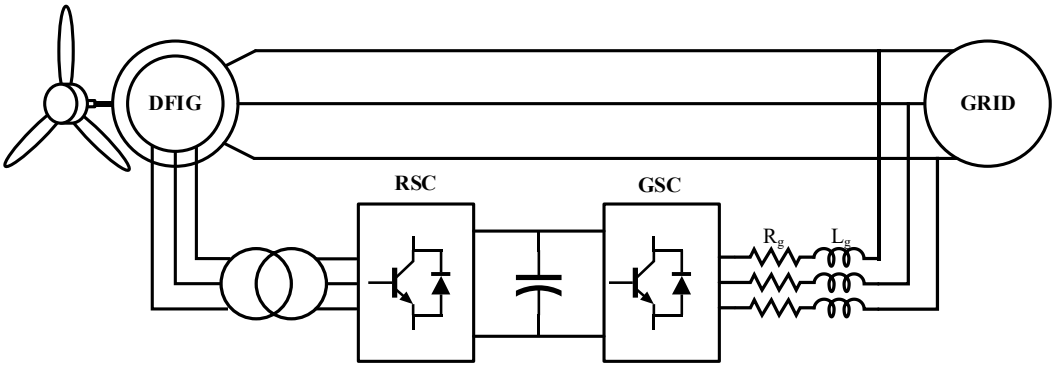

Fig. 1.1. Doubly-fed induction generator wind turbine structure.

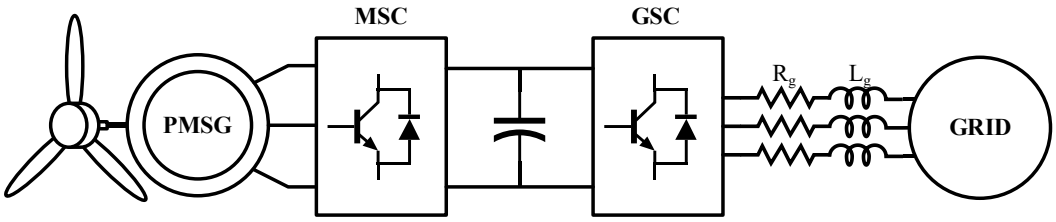

Fig. 1.2. Permanent magnet synchronous generator wind turbine structure.

1.2 Research Motivation

The low-voltage ride-through (LVRT) capability of wind turbines is an

important grid code requirement (GCR) that is enforced in many countries, which requires wind turbines to be grid-connected during voltage dips to provide reactive power ancillary service and to facilitate fast system restart [7], [8], [10], [11]. However, there are some challenges to achieving LVRT for variable speed WTs. When the grid voltage dips, the power that can be transferred to the grid is severely restricted to prevent overcurrent on the transmission system and the WECS. In response to the grid power, the excess generator power must either be reduced or dissipated to prevent charging the DC-link [7], [8], [10]–[15]. Additionally, the direct stator to grid connection of the DFIG results in severe transient dynamics causing large fault currents that may damage the WECS [16]–[20].

The PMSG and DFIG are both very popular choices for variable speed wind turbines, and there are several LVRT solutions for the PMSG and the DFIG. Therefore, it would be valuable to compare the LVRT performances for each type of WT using their various LVRT solutions, so that wind farm owners can choose which type of WT with which LVRT method is better financially suitable for them.

Many LVRT methods are known to trigger mechanical transient responses on the drivetrain system [8], [10], [11], [21]. These mechanical dynamics on the drivetrain causes additional fatigue on the drivetrain, which may increase the operation and maintenance cost (OMC) of the entire wind farm. The estimated net present OMC of WTs over 20 years amounts to 27% of the capital investment, and spare parts account for 60% of the total OMC [22]. Therefore, it is important to analyze the significance of the mechanical stress caused by each LVRT method, so wind farm owners and manufacturers can be more informed about the risk of additional OMC associated with each LVRT method.

1.3 Research Objectives

The objective of this research is to assess the electromechanical performance and the stress life implication of various LVRT solutions for the PMSG and the DFIG. The research objectives are as follows:

- The implementation of the PMSG LVRT methods: the DC chopper (DCC) method, the stored energy in rotor inertia (SEIRI) method, and the hybrid combination of the two [8], [10], [11], [14].
- The implementation of the DFIG LVRT methods: the DCC with the machine flux weakening method, the parallel rotor crowbar (RCB) method, and the series rotor crowbar (SRCB) method [6], [16], [17], [23].
- The assessment of the stress-life implication on the main shaft resulting from LVRT methods that induces mechanical transients.
- The performance comparison of the PMSG LVRT solutions with the DFIG LVRT solutions.

1.4 Thesis Contributions

The thesis contributions to low-voltage ride-through of wind energy systems are the following

1) Comparison of the electromechanical performance of DFIG and PMSG LVRT method

The PMSG and DFIG are both very popular choices for variable speed wind turbines, and there are various LVRT solutions with different benefits for each type of WTs. Therefore, it is essential to assess and compare the performances of the LVRT methods for each WT, so that wind farm owners and WT manufacturers can decide which type of WT and which LVRT method is better suited for their investment. This thesis provides an overview of the PMSG and the DFIG LVRT solutions and compares the dynamic performances of each LVRT method.

2) Damage analysis of the wind turbine shaft caused by LVRT methods

The PMSG and the DFIG both have LVRT solutions that impact the mechanical system by altering the electromagnetic (EM) torque. For the PMSG, the EM torque is reduced for the inertia-based methods to prevent DC-link overvoltage. Whereas, for the DFIG, the EM torque is reduced by the stator voltage dip and the control of the rotor current to mitigate overcurrent. The reduction in the EM torque results in additional stress on the drivetrain. Therefore, this thesis has initiated the damage

analysis of the main drivetrain shaft using rainflow counting (RFC) and Palmgren-Miner's rule to quantify the lifetime impact of various LVRT methods, so that wind farm owners and manufacturers can be more informed about the potential risk of additional drivetrain OMC resulting from LVRT.

1.5 Thesis Layout

The thesis will be organized as follows:

Chapter 2 provides a literature survey of the LVRT grid code requirements for various countries and the challenges of LVRT for DFIG- and PMSG-based WTs. Then, an overview is provided for the PMSG and the DFIG LVRT solutions that will be studied in this thesis. Afterwards, the WT drivetrain model and the stress-life analysis method will be introduced.

Chapter 3 presents the control and the performance analysis of the PMSG LVRT solutions being: the DCC method, the SEIRI method, and the hybrid method. Stress-life analysis is performed on the mechanical performance to demonstrate the OMC implications of each PMSG LVRT method.

Chapter 4 presents the control and the performance analysis of the DFIG LVRT solutions being: the DCC with the machine flux weakening method, the RCB method, and the SRCB method. Stress-life analysis is performed on the mechanical performance to demonstrate the OMC implications of each DFIG LVRT method.

Chapter 5 compares the electromechanical performance of the LVRT methods of the DFIG and the PMSG to illustrate the benefits and disadvantages of each type WT and their corresponding LVRT solutions.

Chapter 6 presents the thesis summary, the conclusions, and the future works of this thesis.

Chapter 2

Literature Survey and Background

2.1 Introduction

The main topics of this thesis is the electromechanical performance assessment of and the stress-life analysis of various LVRT methods for the PMSG and the DFIG. This chapter provides the literature survey of the main topics of this thesis. First, the LVRT grid code regulations for various countries are reviewed and some challenges of LVRT for the PMSG and DFIG are discussed. Then, an overview is provided for the three PMSG and the three DFIG LVRT solutions that will be assessed in this thesis. Then, the WT drivetrain modelling is introduced, and the stress-life analysis method of the WT is studied.

2.2 Review of low-voltage ride through regulations

The growth of wind power generation has been increasing to fulfill the global demands for renewable alternative energy. However, the increasing penetration of WTs is resulting in stricter GCR for WTs to ensure the grid's reliability and stability. One of the most important GCR for WT is LVRT, which requires WTs to be grid-connected during voltage dips to provide ancillary reactive power support and to offer fast system recovery [7], [8], [10], [11].

2.2.1 LVRT grid code requirement

There are various LVRT profiles to meet the demand of each country's distribution system operator (DSO) and transmission system operator (TSO) [10]. Various country's LVRT grid code can be seen in Fig. 2.1, which specifies the duration WTs must be grid-connected for a given magnitude of voltage dip. The WTs must remain grid-connected unless the duration of the voltage dip greater than

the value specified by the curve.

The E. ON LVRT grid code that is indicated in red is typically used as a benchmark for testing the performance of the LVRT enhancement strategies. The most severe LVRT case for WTs under the E. ON grid code is when the voltage drops to 0 pu lasting 150 ms. During the LVRT, the WT is usually also required to provide reactive power support. Fig. 2.2 illustrates the allocation of the rated current towards reactive power depending the voltage dip severity for the E. ON grid code [8], [10], [11]. When the grid voltage dips below 0.9 pu, the WT is required to allocate 20% of the rated current as reactive current. As the voltage dip increases, the grid demands more reactive current. When the grid voltage is less than 0.5 pu, 100% of the rated current is allocated towards reactive current.

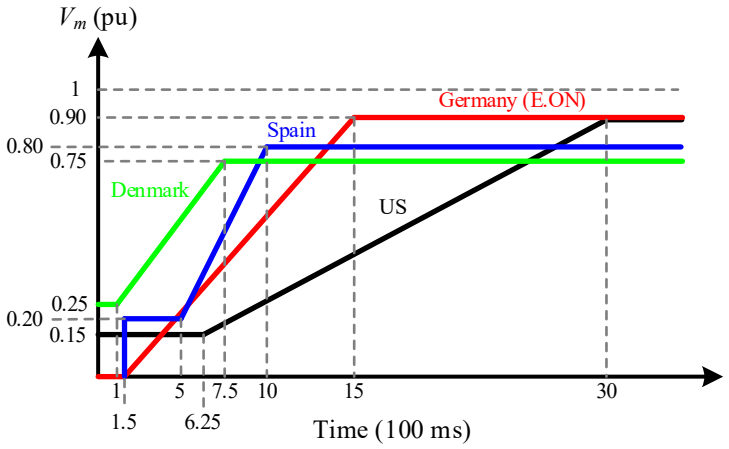

Fig. 2.1. LVRT profile for various countries

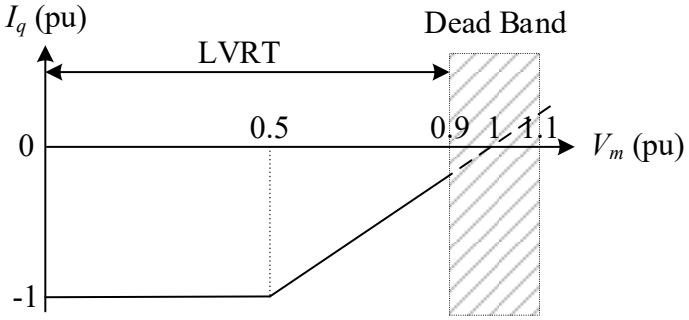

Fig. 2.2. E. ON reactive current requirement

2.2.2 Challenges of LVRT for PMSGs and DFIGs

When the grid voltage dips, the GSC's power output to the grid must decrease

to prevent overcurrent of the grid-side converter's (GSC) switching devices and the transmission lines. This coupled with the reactive power ancillary service of the LVRT requirement will severely limit the grid's output power.

For voltage source converter (VSC) based WECS, the DC-link is formed using capacitors, so the DC-link dynamics can be expressed by

$$\frac{1}{2}C_{dc}\frac{d}{dt}V_{dc}^{\ 2}=\Delta P$$

Equation Chapter (Next) Section 1Equation Chapter (Next) Section 1(2.1)

where C_{dc} is the DC-link capacitance, V_{dc} is the DC-link voltage, and ΔP is the difference between the machine-side converter's (MSC) or rotor-side converter's (RSC) power input and GSC's output power. Integrating (2.1) yields

$$\int_{t_0}^{t_f}\Delta P dt=\frac{1}{2}C_{dc}(V_{dcf}^{\ 2}-V_{dc0}^{\ 2}) \tag{2.2}$$

where V_{dcf} is the final DC-link voltage at the final time t_f and V_{dc0} is the initial DC-link voltage at the initial time t_0.

For the PMSG based WECS, the output power of the GSC is approximately equal to the grid power and the input power of the MSC is approximately equal to the stator power. During a voltage dip, the input power of the MSC is almost unchanged because the full rated WECS decouples the dynamics between the grid and the machine, but the output power of the GSC is significantly reduced. Therefore, a large positive power difference will be experienced by the DC-link. Since the DC-link capacitance is typically small to reduce the size of the WECS, a large power imbalance can lead to a drastic increase in the DC-link voltage causing overvoltage. Therefore, the main goal of LVRT for the PMSG-based WECS is to mitigate overvoltage of the DC-link capacitor.

For the DFIG-based WECS, the GSC's output power is also reduced during voltage dips to meet the grid's current demand and to protect the switching devices

of the GSC. Unlike the PMSG, the DFIG's direct stator to grid connection causes severe electrical transients in response to grid disturbances, such as grid voltage drops, which results in a weak LVRT capability [16], [19], [20]. Furthermore, because of the coupling between the stator and rotor winding, the rotor winding will also experience large rotor current transients leading to overcurrent of the RSC. When the transient rotor power enters the RSC, the DC-link of the DFIG WECS experiences large power imbalances leading to overvoltage. Therefore, for DFIGs, the purpose of LVRT is not only to prevent DC-link voltage, but also to limit the overcurrent of the RSC switching devices.

2.2.3 Overview of the LVRT methods found in PMSGs and in DFIGs

A. PMSG LVRT Methods

Conventionally, for the PMSG, the LVRT is achieved by installing a DC crowbar or chopper (DCC) on the DC-link to protect the capacitor from overvoltage by absorbing the excess power [13] – [15] (Fig. 2.3). When the DCC is turned on, the chopper resistor is placed in parallel to the DC-link capacitor, and because the chopper resistance is much smaller than the impedance of the capacitor under DC conditions, the excess power is redirected to the chopper where it is dissipated. The disadvantage of the DCC is that a large resistor bank is required to dissipate a large capacity of power and a cooling system is needed to dissipate the heat generated by the DCC, which increases the cost of the WT.

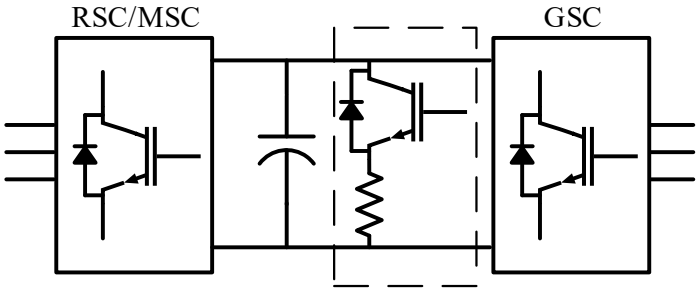

Fig. 2.3. DC chopper LVRT method

Alternatively, another LVRT strategy for PMSG-based WECS is to reduce the

stator power to match the grid power, which stores the captured wind power in the rotor's inertia. The SEIRI LVRT method has been gaining popularity because it does not require additional hardware. Instead, the SEIRI alters the control of the MSC from maximum power point tracking (MPPT) to regulating the DC-link voltage under LVRT [8], [10], [11], [16]. This reduces the stator power to match the grid power causing the captured wind power to be stored as rotational energy in the WT's inertia. The stored power will be released back to the grid once the fault is cleared. However, the SEIRI method introduces mechanical dynamics from rapidly decreasing the EM torque, which increases the stress on the drivetrain and causes overspeeding of the generator [16].

The hybrid combination of the SEIRI and the DCC method is another alternative LVRT method that can provide some of the benefits of both methods. The hybrid method is suitable approach for traditional wind turbines that are already equipped with a fully rated DCC circuit. One benefit of the hybrid method is that the transient power difference between the stator and grid, which is caused by the relatively slow response time of the SEIRI method, can be dissipated through the DCC to reduce DC-link overvoltage [14]. In addition, the SEIRI method has limited power storage capacity because the rotor will overspeed over long LVRT durations. With the hybrid method, the SEIRI method can be turned off once overspeeding occurs, and the DC-link voltage can still be held at the rated value by utilizing the DCC. Whereas, for newly built wind turbines with the SEIRI LVRT method, the hybrid method can be implemented using a partially rated crowbar. However, the SEIRI method cannot be turned off. In additional to reducing transient overvoltage of the DC-link, the hybrid method can also allow the stator power to reduce in stages while regulating the DC-link voltage at the rated value. This can reduce the mechanical transient on the shaft by decreasing the severity of the EM torque reduction, and the rotor acceleration can also be reduced because less power is stored in the rotor's inertia.

B. DFIG LVRT Methods

For the DFIG-based WECS, the overcurrent of the RSC is required to be limited along with preventing the DC-link overvoltage. The DCC is also a popular

protective device used to protect the DC-link capacitor from overvoltage for DFIG-based WECS. However, for type 3 WECS, the overcurrent on the WECS, which is caused by the direct stator to grid connection, cannot be prevented using the DCC method [17]. One control method to limit the rotor overcurrent is the demagnetizing method by weakening the machine's flux [17], [23].

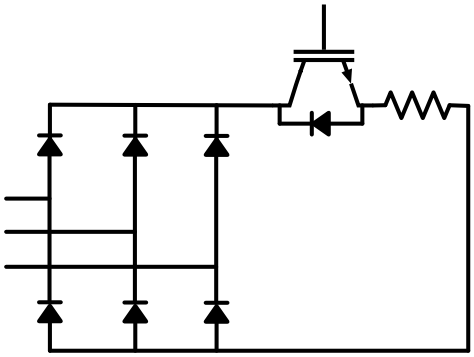

Fig. 2.4. Rotor crowbar LVRT method

However, conventionally for DFIG, overcurrent is limited by installing a parallel rotor crowbar circuit to the rotor winding of the DFIG [6], [16], [17], [23]–[26]. The RCB is a three-phase diode bridge connected with a chopper circuit located on the DC-side, as shown in Fig. 2.4. When LVRT occurs, the RSC is disabled by removing its gate pulses. Simultaneously, the RCB is activated to absorb the large fault currents [16], [17], [23]. However, one disadvantage of the RCB method is that disabling the RSC changes the DFIG into a squirrel-cage induction generator (SCIG) that absorbs reactive power from the grid [17], [18], [23], [26]. Thus, the RCB LVRT method cannot provide the reactive power compensation required from the LVRT grid code requirements. Moreover, although the RCB can be used to reduce the overcurrent of the RSC, the DC-link voltage may still increase slightly during the LVRT [16]. Therefore, an additional DCC may be required in coordination with the RCB to limit the overvoltage of the DC-link capacitor [17], [23].

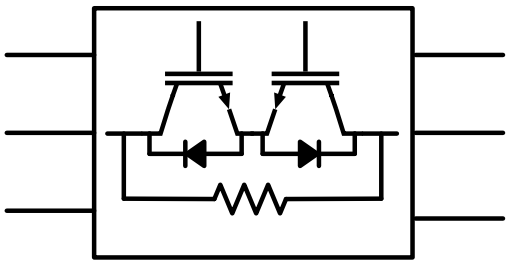

Fig. 2.5. Rotor side series crowbar LVRT method

Alternatively, another hardware-based DFIG LVRT method is the series rotor crowbar (SRCB) shown in Fig. 2.5 [16]. The SRCB is a 3-phase breaker with parallel resistors in each phase, which is placed in series between the RSC and the rotor winding. Normally, the SRCB is switched on bypassing the parallel resistors. When a fault is detected, the SRCB is turned off, which puts the resistors in series with the RSC and rotor winding [16]. The additional series resistance increases damping of the rotor circuit, which reduces the rotor overcurrent along with the stator overcurrent due to coupling.

2.3 Mechanical analysis of wind turbines under LVRT

The PMSG and DFIG both have LVRT methods that alters the EM torque, which introduces mechanical dynamics on the drivetrain. These mechanical dynamics causes additional fatigue on the drivetrain, which should be investigated because it may degrade the WT's lifetime and increase the OMC of the WT. The OMC over the lifespan of the WT covers a significant portion of the capital investment. Therefore, performing lifetime analysis of the LVRT methods that induces stress on the drivetrain is important to minimize OMC to maximize the profitability of wind farms. To analyze the fatigue on the WT, a more accurate drivetrain model is required, such as the two-mass model because lumping the drivetrain masses into the one-mass model conceals the transient dynamics of the drivetrain. Then, the stresses acting on the rotating shaft are identified and the impact of these stresses on shaft's lifetime are investigated. Finally, the lifetime analysis method is introduced to analyse the fatigue resulting from the mechanical

dynamics caused by the LVRT methods.

2.3.1 Modelling of the wind turbine drivetrain

The investigation of the inertia-based LVRT method, such as the SEIRI method, has been commonly researched using a lumped single-mass drivetrain model. However, reducing the stator power to meet the grid's power demand also reduces the EM torque that is applied to the drive-train system, which causes mechanical dynamic responses. Because of the presence of the mechanical transients, a better representation of the wind turbine drivetrain is required to better analyze the effects of these LVRT methods. The most accurate model for the wind turbine is the six-mass model, which encompasses the masses for the three-turbine blades, the rotor hub, the gear box, and the generator, as shown in Fig 2.6 [27].

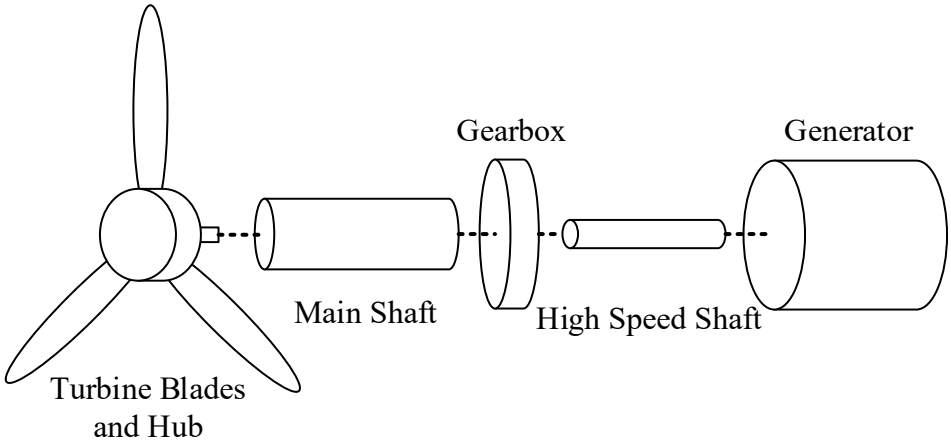

Fig. 2.6. Six-mass wind turbine model

Although a six-mass model provides the highest accuracy, a two-mass model is widely used to model the WT drivetrain and is sufficiently accurate to analyze the transient responses caused by the EM torque reduction [28], [29]. First, the six-mass model can be simplified by combining the turbine blades and the rotor hub into an aggregate model forming a three-mass model. Then, the two-mass model is derived from the three-mass model by combining the mass of the gearbox with the generator, as shown in Fig. 2.7.

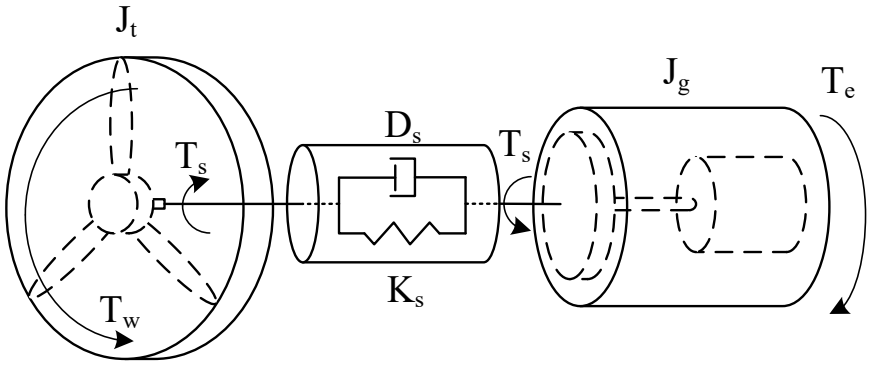

Fig. 2.7. Simplified Two-mass wind turbine model

Ignoring the self-damping component for both masses, the two-mass drivetrain dynamics can be expressed by

$$J_t \frac{d}{dt}\omega_t = T_w - T_s \tag{2.3}$$

$$J_g \frac{d}{dt}\omega_g = \frac{T_s}{N_{gb}} - T_e \tag{2.4}$$

$$T_s = K_s\theta_d + D_s \frac{d}{dt}\theta_d \tag{2.5}$$

$$\frac{d}{dt}\theta_d = \omega_t - \frac{\omega_m}{N_{gb}} \tag{2.6}$$

where J_t and J_g are the inertias of the turbine and the generator, respectively. ω_t and ω_g are the turbine blade speed and generator speed, respectively. T_w, T_s, and T_e are the wind turbine blade torque, the shaft torque, and the EM torque, respectively. N_{gb} is the gearbox ratio, K_s is the cumulative shaft stiffness, D_s is the cumulative shaft mutual damping. Lastly, θ_d is the angle of twist of the shaft, and its derivative is the speed difference between the two masses.

2.3.2 Stresses acting on the drivetrain system during LVRT

In practice, there will be multiaxial stresses acting on the shaft, but for simplicity, the stress analysis will assume that a biaxial stress acts on the shaft,

which is separated into a bending and a torsional stress component, as seen in Fig. 2.8.

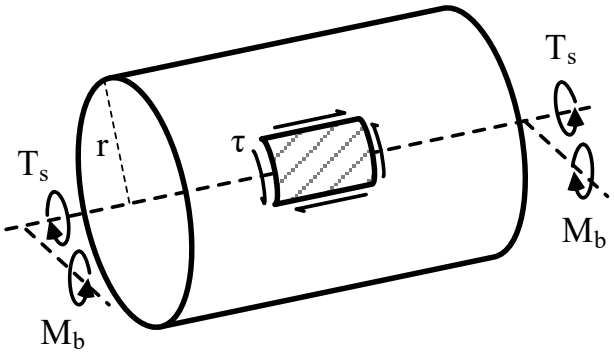

Fig. 2.8. Stresses acting on a rotating shaft.

Although the effect of the wind loading also contributes to the bending stress, to simplify the stress analysis, it is assumed that the bending stress is solely caused by the bending moment induced by the weights of the hub and the turbine blade and the normal forces acting on the main bearings and the gearbox for a three-point drivetrain configuration [30]. These simplifying assumptions will marginally reduce the effective stress on the shaft.

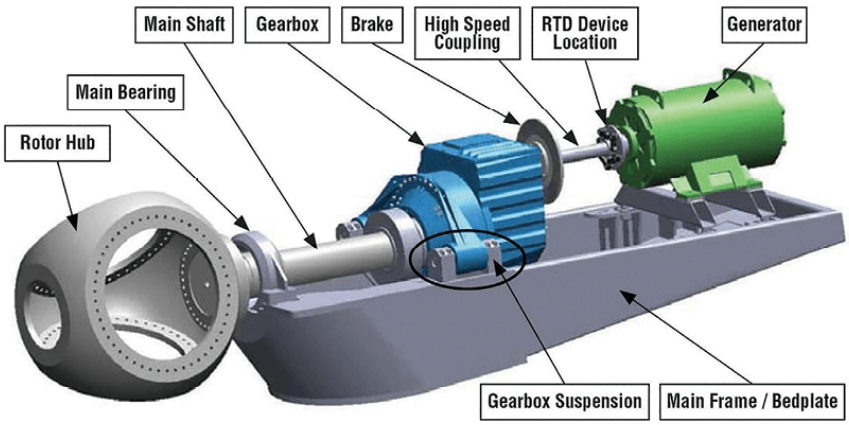

Fig. 2.9. Wind turbine three-point drivetrain model [40]

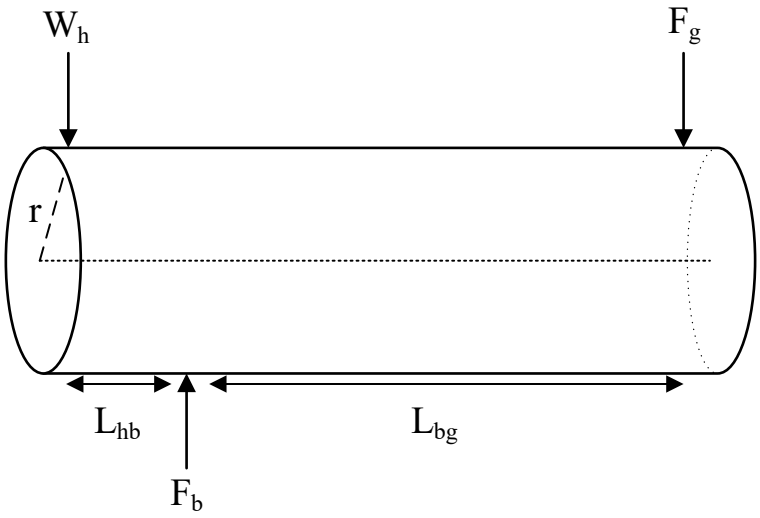

Fig. 2.10. Forces applied on the main shaft of the wind turbine

Fig. 2.9 illustrates a typical three-point WT drivetrain system configuration. At a given instance of time, the rotating shaft can be treated as a cylindrical beam, and the instantaneous forces acting on the main shaft is illustrated in Fig. 2.10. Where W_h is the cumulative weight of the hub and the turbine blades, F_b is the normal force of the main bearing, and F_g is the normal force of the generator. L_{hb} is the length between the center of mass of the hub to the main bearings and L_{bg} is the length between the main bearings and the gearbox. F_g is directed downwards to counteract the moment induced by the weights and F_b is directed upwards to counteract the downward forces cumulatively induced by W_h and F_g. The shear and moment diagram of the main shaft is depicted in Fig. 2.11.

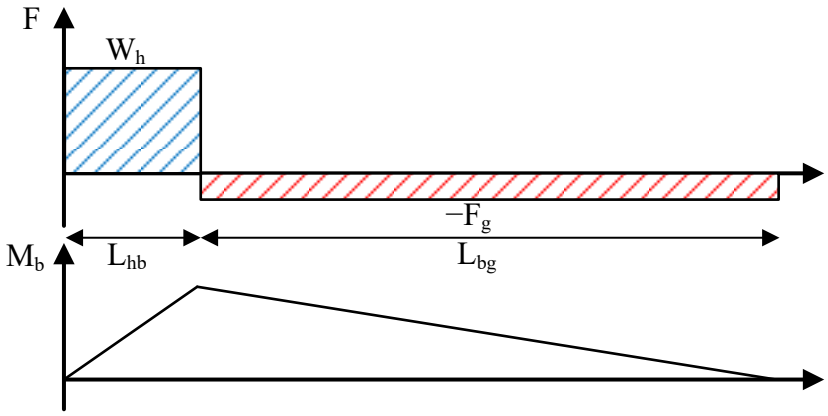

Fig. 2.11. The shear force and bending moment diagram of the main shaft.

The normal forces of the gear box can be calculated by equating the area of the blue shaded rectangle with the area of the red shaded rectangle

$$F_g = \frac{W_h L_{hb}}{L_{bg}} \tag{2.7}$$

From this, the normal force on the main bearings is

$$F_b = W_h + F_g = W_h \left(1 + \frac{L_{hb}}{L_{bg}} \right) \tag{2.8}$$

The bending moment M_b is obtained by integrating the area under the shear force diagram, and the maximum bending moment occurs at the main bearing and is equal to

$$M_{b,\max} = W_h L_{hb} \tag{2.9}$$

At a given instance of time, the bending stress of a stress element on the beam is given in [31] by

$$\sigma = K_f \frac{M_b c}{I} \tag{2.10}$$

where c is the vertical distance from the shaft's neutral axis, I is the area moment of inertia, and K_f is the bending fatigue stress-concentration factor. The stress elements at the top and bottom of the shaft have the largest vertical distance from the neutral axis and the bending moment is maximized at the main bearing. Therefore, the maximum bending stress will occur on the stress elements at the top and bottom of the shaft where the main bearings are located. As the shaft rotates, the vertical distance from the neutral axis for a given stress element will change sinusoidally over time forming an alternating bending stress.

The torsional stress results from the torque applied on the shaft, and is given in [31] by

$$\tau = K_{fs} \frac{T_s r}{J} \tag{2.11}$$

where r is the radial distance from the neutral axis, J is the polar moment of inertia, and K_{fs} is the torsional fatigue stress-concentration factor. The torsional stress maximizes at the outer shell of the shaft and is usually a midrange or average stress.

Methods for stress cycle analysis are well defined for uniaxial stress loading, but these methods are not readily transferable to multiaxial stress loading, as in the case of the drivetrain system. A classical method of performing stress cycle analysis on multiaxial stress is by obtaining the von Mises's equivalent uniaxial stresses, which is given in [31] by

$$\sigma_a^{VM} = \sqrt{\sigma_a^2 + 3\tau_a^2} \tag{2.12}$$

$$\sigma_m^{VM} = \sqrt{\sigma_m^2 + 3\tau_m^2} \tag{2.13}$$

where τ_a and τ_m are the alternating and midrange torsional stress, respectively. σ_a and σ_m are respectively the alternating and midrange bending stress, respectively. σ_a^{VM} and σ_m^{VM} are the von Mises equivalent uniaxial alternating and midrange stress, respectively.

However, the sign of the equivalent uniaxial alternating stress is suppressed but is required for stress-cycle counting [32]. Therefore, to restore the sign, the approximation that the von Mises equivalent stress will assume the sign of the uniaxial alternating bending stress is made because the bending stress is larger than the torsional stress

$$\sigma_a^{VM}(t) = \text{sgn}(\sigma_a(t)) \cdot \sqrt{\sigma_a{}^2(t) + 3\tau_a{}^2(t)} \tag{2.14}$$

2.3.3 Accumulated damage estimation method

The most recognized stress cycle counting method of uniaxial stress is known as rainflow counting (RFC), which is used in conjunction with the material's characteristic stress cycle (SN) curve and the Palmgren-Miner's rule to estimate the

fatigue life [33]. As the name RFC may suggest, it is derived from the analogy of rain flowing down the roof edges of a pagoda. Where, the loading history resembles that of a pagoda roof when the loading history is rotated such that the time axis is pointed vertically downwards, as illustrated in Fig. 2.12(a) [34]. From the loading history, RFC extracts the number of closed loading reversals or half-cycles and the associated stress range from an arbitrary uniaxial load in a post-processing manner [33], [34].

The SN curves are a material-specific curve-fit of the stochastic stress-cycle data generated from applying a constant stress range on multiple identical test specimens and measuring the number of cycles until failure over various magnitudes of stress range. The curve-fit is then generated using the mean life of the stress-cycle data, so operating points lying on the SN curve will have a 50% chance of failing.

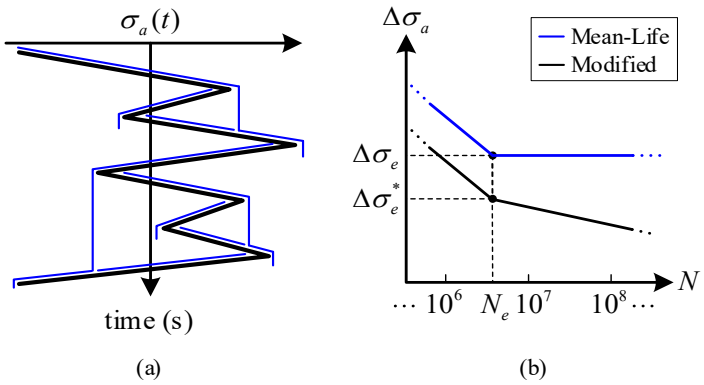

Fig. 2.12. (a) Rainflow counting and (b) the mean-life SN curve and the modified SN curve for non-welded and rolled parts

The mean life SN curve is then modified for non-welded forged and rolled parts according to the procedure specified in Section 5.B.3 of the wind turbine guidelines compiled by Germanischer Lloyd (GL) [35]. Fig. 2.12(b) illustrates a generic mean-life SN curve and the GL modified SN curve for a steel component, shown respectively in blue and black. The modified curve is a piece-wise function with a general form given by

$$N = \begin{cases} N_e(\Delta\sigma_e^*/\Delta\sigma_a)^{m_1}, & \Delta\sigma_a \geq \Delta\sigma_e^* \\ N_e(\Delta\sigma_e^*/\Delta\sigma_a)^{2m_1-1}, & \Delta\sigma_a < \Delta\sigma_e^* \end{cases} \tag{2.15}$$

where $\Delta\sigma_a$ is the applied alternating stress range, $\Delta\sigma_e^*$ is the modified endurance limit, N_e is the number of cycles before failure at the endurance limit, and m_1 is the logarithmic slope of the modified SN curve for stress ranges larger than $\Delta\sigma_e^*$. Since the modified SN curve is below the mean-life SN curve, the material is predicted to have a shorter fatigue life under the same stress loading history.

Palmgren-Miner's rule assumes that damage accumulation is linear, so the accumulated damage can be obtained from the summation of the fractional damage at each operating stress range. Therefore, the accumulated damage is a percentage reduction towards the total lifetime of a material and is expressed in [33] by

$$D_{ac} = \sum_{i=1}^{k} \frac{n_i}{N_i} \tag{2.16}$$

where D_{ac} is the accumulated damage, n_i is the measured number of stress cycle, and N_i is the number of stress cycle until failure for the i^{th} stress range.

In summary, RFC is applied on the loading history to obtain the number of cycles n_i and the corresponding stress ranges $\Delta\sigma_i$. Next, the maximum allowable number of cycles N_i is obtained from the SN curve for each stress range $\Delta\sigma_i$. Lastly, the Palmgren-Miner's rule is applied to assess the damage accumulation.

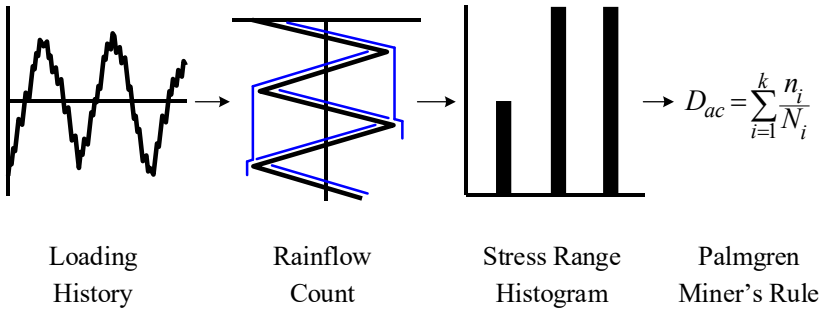

Fig. 2.13. The overall RFC damage estimation procedure.

Chapter 3

Comparison of PMSG LVRT Methods

3.1 Introduction

The PMSG has a fully rated WECS that interfaces the stator winding to the grid, which decouples the grid and machine dynamics. Typically, VSC are used in WECS, and the most common WECS topology is the back-to-back (BTB) two-level VSC. For PMSGs with a VSC-based WECS, LVRT causes DC-link overvoltage because the grid power is severely limited during a voltage dip, while the stator power is almost unchanged. The most common LVRT strategy used for PMSG WTs is the DCC, which is a hardware-based solution where a chopper resistor is attached to the DC-link to dissipate the excess stator power. Alternatively, the research community has proposed the control-based SEIRI LVRT method that reduces the stator power to match the grid power and stores the excess power in the inertia of the rotor. Lastly, the hybrid combination of the DCC and the SEIRI LVRT method can be established by having the DCC method be open-loop controlled, while the SEIRI method is closed-loop controlled.

This chapter will provide an overview of the modelling of the PMSG and its control under normal operations. The control of the DCC, the SEIRI, and the hybrid LVRT methods are then presented. To analyze the performance of each LVRT method, the grid tied PMSG will be simulated on MATLAB/Simulink using the simulation parameters given in Table 3.1. The electrical and mechanical performance of each LVRT method will be analyzed under symmetrical and asymmetrical voltage dips to 0.1 pu.

3.2 PMSG modelling and normal operation control

The PMSG is constructed with permanent magnets affixed to the rotor to

generate the rotor magnetic flux. This removes the need for a rotor winding, which reduces the size and weight of the generator, but comes at the cost of expensive permanent magnets [36]. The stator voltage dynamic of a PMSG is typically given in the synchronous (dq) frame using field-oriented control (FOC) given by

$$v_{sd} = -R_s i_{sd} - L_{sd}\frac{d}{dt} i_{sd} + \omega_r L_{sq} i_{sq}$$

Equation Chapter (Next) Section 1(3.1)

$$v_{sq} = -R_s i_{sq} - L_{sq}\frac{d}{dt} i_{sq} - \omega_r L_{sd} i_{sd} + \omega_r \lambda_r \tag{3.2}$$

where v_{sd} and v_{sq} are the dq-axis stator voltages, i_{sd} and i_{sq} are the dq-axis stator currents directed towards the MSC, R_s is the stator winding resistance, L_{sd} and L_{sq} are the dq-axis stator winding inductance, ω_r is the electrical rotor speed, and λ_r is the rotor flux linkage produced by the rotor's permanent magnets. The EM torque is related to the stator current and is given by

$$T_e = \frac{3}{2} P(\lambda_r i_{sq} - (L_{sd} - L_{sq}) i_{sd} i_{sq}) \tag{3.3}$$

where P is the number of pole pairs. For nonsalient PMSG WTs, the d- and q-axis stator winding inductance are equal, so the EM torque is directly related to the q-axis stator current.

$$T_e = \frac{3}{2} P \lambda_r i_{sq} \tag{3.4}$$

The stator is usually directly connected to the terminal of the MSC because the stator resistance and inductance act as an RL filter that smooths out the stator current, so the MSC's AC terminal voltage is equal to the stator voltage and can be adjusted to control the stator current.

The GSC is connected to the grid through a filter, such as an RL filter, to smooth

the pulse width modulation (PWM) waveforms outputted from the converter. The GSC terminal voltage dynamics can be expressed in the *dq*-frame using voltage-oriented control (VOC) given as

$$v_{td} = v_{gd} + R_g i_{td} + L_g \frac{d}{dt} i_{td} - \omega_{gr} L_g i_{tq} \tag{3.5}$$

$$v_{tq} = v_{gq} + R_g i_{tq} + L_g \frac{d}{dt} i_{tq} + \omega_{gr} L_g i_{td} \tag{3.6}$$

where v_{td} and v_{tq} are the *dq*-frame GSC terminal voltages, i_{td} and i_{tq} are the *dq*-frame GSC output current directed towards the grid. v_{gd} and v_{gq} are the *dq*-frame grid voltages, ω_{gr} is the grid frequency, R_g is the converter filter resistance, and L_g is the converter filter inductance.

3.2.1 MSC and GSC control

A. Machine-side converter control

1. *MSC conventional PI control*

The VSC-based WECS is typically current-mode controlled, which regulates the AC output current to its reference value by adjusting the AC terminal voltage of the VSC and can be achieved using a proportional integral (PI) controller with the procedure described in [37].

As mentioned previously, the stator winding is directly connected to the MSC, so the terminal voltage of the MSC is equal to the stator voltage and can be adjusted to control the stator current. Applying the Laplace transform to (3.1) and (3.2) transfers the time-domain equations to the frequency-domain expressed by

$$V_{sd} = -R_s I_{sd} - sL_s I_{sd} + \omega_r L_s I_{sq} \tag{3.7}$$

$$V_{sq} = -R_s I_{sq} - sL_s I_{sq} - \omega_r L_s I_{sd} + \omega_r \lambda_r \tag{3.8}$$

where s is the operator variable in the Laplace domain, are the *dq*-axis stator voltages in the Laplace domain, and I_{sd} and I_{sq} are the *dq*-axis stator currents in the

Laplace domain.

The *d*- and *q*-axis plant model can be formulated from (3.7) and (3.8) to be

$$\wp_{sd}(s) = \frac{I_{sd}}{V_{sd} - D_{sd}} = \frac{-1}{L_s s + R_s} \tag{3.9}$$

$$\wp_{sq}(s) = \frac{I_{sq}}{V_{sq} - D_{sq}} = \frac{-1}{L_s s + R_s} \tag{3.10}$$

With the corresponding *d*- and *q*-axis disturbances defined as

$$D_{sd}(s) = \omega_r L_s I_{sq} \tag{3.11}$$

$$D_{sq}(s) = -\omega_r L_s I_{sd} + \omega_r \lambda_r \tag{3.12}$$

Using PI-based control and the plant model expressed in (3.9) and (3.10), the *dq*-axis current control loops are implemented as described in Fig. 3.1 and 3.2.

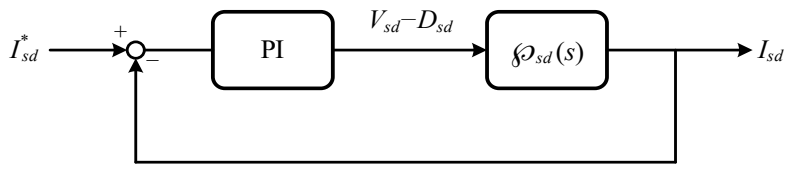

Fig. 3.1. The *d*-axis stator current control loop.

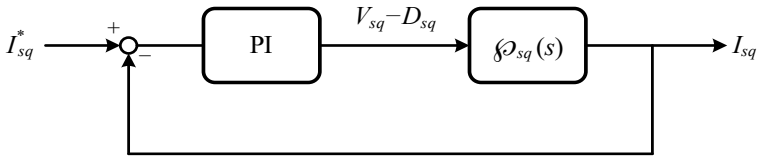

Fig. 3.2. The *q*-axis stator current control loop.

From the plant model described in (3.9) and (3.10), the open-loop gain using a PI controller is

$$\ell_{sd}(s) = \ell_{sq}(s) = -\frac{k_{ps}}{L_s s}\frac{s + k_{is}/k_{ps}}{s + R_s/L_s} \tag{3.13}$$

To achieve a positive loop gain and pole-zero cancellation for (3.13), the PI control parameter should be designed as

$$k_{ps} = -L_s/\tau_i \tag{3.14}$$

$$k_{is} = -R_s/\tau_i \tag{3.15}$$

where τ_i is the closed-loop time constant resulting in a control bandwidth that is $1/\tau_i$. According to [37], the time constant should be designed considerably small for fast control response time, but large enough so that the control bandwidth is a magnitude smaller than the switching frequency of the VSC when given in radians per second.

From the *dq*-frame current control loops expressed in Fig. 3.1 and Fig. 3.2, the PI controller outputs the stator voltage along with the disturbance. However, the MSC can only adjust the MSC terminal voltage, which is the stator voltage. Therefore, the disturbance needs to be fed to the PI output to isolate for the desired stator voltage, which can then be used to generate the PWM through the sinusoidal PWM (SPWM) or space vector modulation (SVM).

2. *MSC model predictive control*

Another way to control the MSC is by using finite-control-set model predictive control (FCS-MPC), which is a subset of model predictive control (MPC). FCS-MPC can be used when the system has a finite number of states, which is the case for power converters [8], [10]. FCS-MPC provides fast control response time and can incorporate nonlinearities and constraints by adjusting the control law [8]. To control the MSC using FCS-MPC, first the stator dynamics expressed in (3.1) and (3.2) are discretized. When the sampling time is small, the forward Euler method can be used to discretize the time directives in the continuous time model by

$$\frac{d}{dt}f(t) \approx \frac{f[k+1]-f[k]}{T_{sm}} \tag{3.16}$$

where T_{sm} is the sampling period and k represents k^{th} sampling period. Now, applying forward Euler's method to (3.1) and (3.2) and solving for the k+1$^{\text{th}}$ instance of i_{sd} and i_{sq} yields

$$i_{sd}[k+1] = \left(1 - \frac{R_s T_{sm}}{L_s}\right) i_{sd}[k] + \omega_r T_{sm} i_{sq}[k] - \frac{T_{sm}}{L_s} v_{sd}[k] \tag{3.17}$$

$$i_{sq}[k+1] = \left(1 - \frac{R_s T_{sm}}{L_s}\right) i_{sq}[k] - \omega_r T_{sm} i_{sd}[k] + \frac{T_{sm}}{L_s}\left(\omega_r \lambda_r - v_{sq}[k]\right) \tag{3.18}$$

There is a total of eight switching states for the two-level VSC corresponding to six active voltage vectors and two zero voltage vectors. This means that there are eight outcomes for $v_{sd}[k]$ and $v_{sq}[k]$ and eight possible outcomes for $i_{sd}[k+1]$ and $i_{sq}[k+1]$ by extension. The control law is in the form of a cost function, and the constraints can be added to the control law by adding terms to the cost function. Among the eight possible k+1$^{\text{th}}$ stator currents, the one that minimizes the cost function is the one that is chosen for the k^{th} switching interval. One possible cost function for the MSC is

$$g_s = (i_{sd}[k+1] - i_{sd}^*)^2 + (i_{sq}[k+1] - i_{sq}^*)^2 \tag{3.19}$$

where i_{sd}^* and i_{sq}^* are the stator current reference values. This cost function chooses the stator voltage vector that generates $i_{sd}[k+1]$ and $i_{sq}[k+1]$ that matches closest to the references value.

B. Grid-side converter control

1. *MSC conventional PI control*

Like the MSC, the VSC-based GSC is also current-controlled, and the terminal voltage of the GSC controls the grid current. Applying the Laplace transform to

(3.5) and (3.6) transfers the grid dynamics in the time-domain to the frequency-domain expressed by

$$V_{td} = V_{gd} + R_g I_{gd} + sL_g I_{gd} - \omega_{gr} L_g I_{gq} \tag{3.20}$$

$$V_{tq} = V_{gq} + R_g I_{gq} + sL_g I_{gq} + \omega_{gr} L_g I_{gd} \tag{3.21}$$

where V_{td} and V_{tq} are the dq-axis GSC terminal voltages in the Laplace domain, and I_{gd} and I_{gq} are the dq-axis grid currents in the Laplace domain. The d- and q-axis plant model that yields from (3.20) and (3.21) are

$$\wp_{td}(s) = \frac{I_{td}}{V_{td} - D_{td}} = \frac{1}{L_g s + R_g} \tag{3.22}$$

$$\wp_{tq}(s) = \frac{I_{tq}}{V_{tq} - D_{tq}} = \frac{1}{L_g s + R_g} \tag{3.23}$$

With the corresponding d- and q-axis disturbances defined as

$$D_{td}(s) = V_{gd} - \omega_{gr} L_g I_{gq} \tag{3.24}$$

$$D_{tq}(s) = V_{gq} + \omega_{gr} L_g I_{gd} \tag{3.25}$$

The dq-axis current control loops using PI-based control are implemented as described in Figs. 3.3 and 3.4.

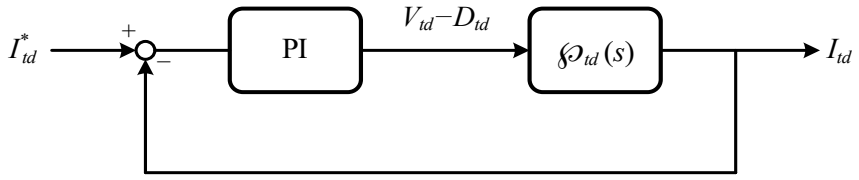

Fig. 3.3. The d-axis GSC terminal current control loop

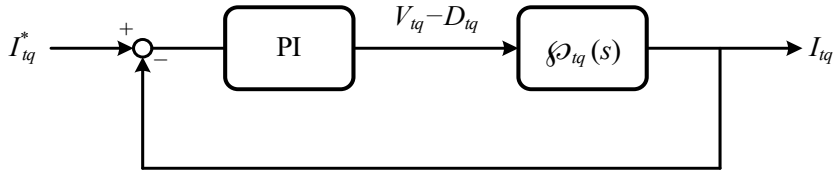

Fig. 3.4. The *q*-axis GSC terminal current control loop

The resultant open-loop gain using the PI controller is

$$\ell_{td}(s) = \ell_{tq}(s) = \frac{k_{pt}}{L_g s} \frac{s + k_{it} / k_{pt}}{s + R_g / L_g} \tag{3.26}$$

For pole-zero cancellation of (3.26), the PI control parameters are designed as

$$k_{pt} = L_g / \tau_i \tag{3.27}$$

$$k_{it} = R_g / \tau_i \tag{3.28}$$

Like in the case for the MSC, the disturbance needs to be fed to the PI controller's output to isolate for the desired GSC terminal voltage, which can then be used to generate the PWM signals either through SPWM or SVM.

2. *GSC model predictive control*

To control the GSC using FCS-MPC, the GSC terminal dynamics expressed in (3.5) and (3.6) are discretized using the forward Euler method. Solving for the k+1$^{\text{th}}$ instance of i_{td} and i_{tq} of the discretized grid model yields

$$i_{td}[k+1] = \left(1 - \frac{R_g T_{sm}}{L_g}\right) i_{td}[k] + \omega_{gr} T_{sm} i_{tq}[k] + \frac{T_{sm}}{L_g}\left(v_{td}[k] - v_{gd}[k]\right) \tag{3.29}$$

$$i_{tq}[k+1] = \left(1 - \frac{R_g T_{sm}}{L_g}\right) i_{tq}[k] - \omega_{gr} T_{sm} i_{td}[k] + \frac{T_{sm}}{L_g}\left(v_{tq}[k] - v_{gq}[k]\right) \tag{3.30}$$

Since the GSC is also a two-level VSC, there are eight outcomes for $v_{td}[k]$ and $v_{tq}[k]$ and eight possible outcomes for $i_{td}[k+1]$ and $i_{tq}[k+1]$ by extension. For the GSC, the cost function can be expressed by (3.31), which selects the GSC terminal voltage vector that generates $i_{td}[k+1]$ and $i_{tq}[k+1]$ that matches closest to the GSC terminal current references values, i^*_{td} and i^*_{tq}.

$$g_t = (i_{td}[k+1] - i^*_{td})^2 + (i_{tq}[k+1] - i^*_{tq})^2 \tag{3.31}$$

3.2.2 Outer control loops under normal operations

A. Machine-side converter MPPT

During normal operation, the purpose of the MSC is to maximize the WTs power output, which is commonly known as MPPT. The maximum power that can be extracted from the wind is a fraction of the total kinetic wind power, and the percentage that is extracted is known as the rotor efficiency. The power that is extracted from the wind is given in [38] by

$$P_w = \frac{1}{2} C_p(\beta, \lambda) \rho \pi r_b^2 v_w^3 \tag{3.32}$$

$$\lambda = \frac{\omega_t r_b}{v_w} \tag{3.33}$$

where C_p is the rotor efficiency, which is a function of the pitch angle, β, and the tip speed ratio (TSR), λ. r_b is the turbine blade radius, ρ is the air density, and v_w is the wind speed. The theoretical maximum rotor efficiency, C_p, is 59.3%, which occurs when the ratio between the downwind and upwind speed is 1/3. However, for practical wind turbines, the rotor efficiency, C_p, is significantly lower than the ideal 59.3%. A typical Betz function that is used to model a wind turbine's rotor efficiency is given in [37] by

$$C_p(\beta, \lambda) = 0.5176\left(\frac{116}{\lambda_i} - 0.4\beta - 5\right) e^{\frac{-21}{\lambda_i}} + 0.0068\lambda \tag{3.34}$$

$$\lambda_i = \left(\frac{1}{\lambda + 0.08\beta} - \frac{0.035}{\beta^3 + 1} \right)^{-1} \tag{3.35}$$

Fig. 3.5 illustrates the Betz function. The maximum rotor efficiency is 48% occurring when the pitch angle β=0° and the TSR λ=8.1.

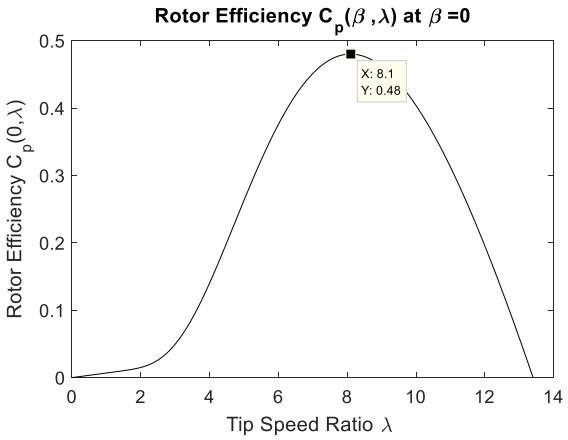

Fig. 3.5. The Betz function at β=0°

For a given pitch angle, β, the TSR, λ, that maximizes the rotor efficiency, C_p, is known as the optimal TSR (OTSR), λ_o. For the Betz function described in (3.34) with a pitch angle of β=0°, the OTRSR is λ_o=8.1. Because the rotor efficiency is maximized at the OTSR, one way to perform MPPT is to maintain the OTSR by adjusting the speed of the turbine blade. In steady state conditions, the generator speed is equal to turbine's speed multiplied by the gearbox ratio, so the generator speed needed to maintain OTSR using (3.33) is

$$\omega_g = N_{gb} \lambda_o \frac{v_w}{r_b} \tag{3.36}$$

The generator dynamics of the two-mass model in (2.4) given in the frequency-domain is

$$T_e = -sJ_g \omega_g + \frac{T_s}{N_{gb}} \tag{3.37}$$

From (3.37), the transfer function between the generator speed and EM torque is

$$H_{\omega}(s) = \frac{\omega_g}{T_e} = -\frac{1}{sJ_g} \tag{3.38}$$

Because of the linear relationship between T_e and i_{sq} expressed in equation (3.4), the EM torque closed-loop gain is equal to the current closed-loop gain given by

$$G_T(s) = \frac{T_e}{T_e^*} = \frac{i_{sq}}{i_{sq}^*} = \frac{1}{\tau_i s + 1} \tag{3.39}$$

Combining (3.38) and (3.39) yields the generator speed plant model as

$$\wp_{\omega}(s) = \frac{\omega_g}{T_e^*} = -\frac{1}{sJ_g(\tau_i s + 1)} \tag{3.40}$$

The generator speed control loop using a PI controller is shown in Fig. 3.6

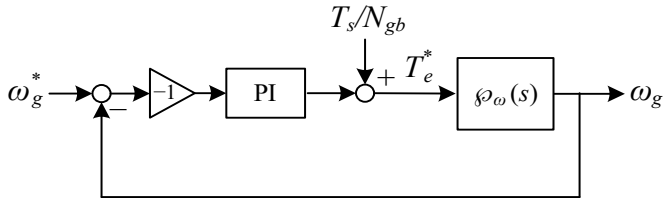

Fig. 3.6. The generator speed control loop.

The open-loop gain of the generator speed control loop using a PI controller is

$$\ell_{\omega}(s) = \frac{k_{p\omega}s + k_{i\omega}}{s} \frac{1}{sJ_g(\tau_i s + 1)} \tag{3.41}$$

The integral controller can be set to zero to maximize control robustness, and the

proportional controller is designed to attain a unity open-loop gain at the crossover frequency of the generator speed, $\omega_{c\omega}$, is given by

$$k_{p\omega} = J_g \left| j\omega_{c\omega} \left(j\tau_i \omega_{c\omega} + 1 \right) \right| \tag{3.42}$$

$$k_{i\omega} = 0 \tag{3.43}$$

Because the mechanical system is much slower than the electrical system, the crossover frequency is chosen to be much smaller, and in this case, it was selected to be one-hundred fiftieth of the inner loop control bandwidth.

$$\omega_{c\omega} = \frac{1}{150\tau_i} \tag{3.44}$$

B. Grid-side converter DC-link voltage control

As mentioned previously, the GSC is used to control the DC-link voltage, which ensures that the power generated at the stator is transferred to the grid. The following DC-link voltage control is design based on [37]. For the PMSG, the DC-link voltage dynamic is given by

$$\frac{1}{2} C \frac{d}{dt} V_{dc}^{\ 2} = P_s - P_t \tag{3.45}$$

where P_t is the GSC output power and P_s is the stator input power. To control the DC-link using the GSC, the GSC output power will be controlled. The GSC output power given in the *dq*-frame is

$$P_t = \frac{3}{2} \left(v_{td} i_{td} + v_{tq} i_{tq} \right) \tag{3.46}$$

Using the GSC terminal voltage dynamics given in (3.5) and (3.6), the terminal power can be obtained as follows

$$\frac{3}{2}v_{td}i_{td} = \frac{3}{2}\left(v_{gd}i_{td} + R_g{i_{td}}^2 + L_g i_{td}\frac{d}{dt}i_{td} - \omega L_g i_{tq}i_{td} \right) \tag{3.47}$$

$$\frac{3}{2}v_{tq}i_{tq} = \frac{3}{2}\left(v_{gq}i_{tq} + R_g{i_{tq}}^2 + L_g i_{tq}\frac{d}{dt}i_{tq} + \omega L_g i_{td}i_{tq} \right) \tag{3.48}$$

Adding (3.47) to (3.48) yields the GSC power output.

$$P_t = \frac{3}{2}\left(v_{gd}i_{td} + v_{gq}i_{tq} + R_g({i_{td}}^2 + {i_{tq}}^2) + L_g i_{td}\frac{d}{dt}i_{td} + L_g i_{tq}\frac{d}{dt}i_{tq} \right) \tag{3.49}$$

The grid power and reactive power in the *dq*-frame is expressed by

$$P_g = \frac{3}{2}\left(v_{gd}i_{td} + v_{gq}i_{tq} \right) \tag{3.50}$$

$$Q_g = \frac{3}{2}\left(-v_{gd}i_{tq} + v_{gq}i_{td} \right) \tag{3.51}$$

Under VOC, the phase-locked loop (PLL) sets the *q*-axis component of the grid voltage to zero, then solving for i_t yields

$$i_{td} = \frac{2P_g}{3v_{gd}} \tag{3.52}$$

$$i_{tq} = -\frac{2Q_g}{3v_{gd}} \tag{3.53}$$

Substituting (3.52) and (3.53) into (3.49) and assuming the grid filter resistance is negligible produces

$$P_t = P_g + \frac{2L_g P_g}{3v_{gd}^2}\frac{dP_g}{dt} + \frac{2L_g Q_g}{3v_{gd}^2}\frac{dQ_g}{dt} \tag{3.54}$$

Now substituting (3.54) into the DC-link voltage dynamic in (3.45) yields

$$\frac{1}{2}C_{dc}\frac{d}{dt}V_{dc}^{\ 2} = P_s - \left(P_g + \frac{2L_gP_g}{3v_{gd}^2}\frac{dP_g}{dt}\right) - \frac{2L_gQ_g}{3v_{gd}^2}\frac{dQ_g}{dt} \tag{3.55}$$

Because of the nonlinearity term, (3.55) needs to be linearized around the operating point (P_{g0}, Q_{g0}) resulting in

$$\frac{1}{2}C_{dc}\frac{d}{dt}\tilde{V}_{dc}^{\ 2} = \tilde{P}_s - \left(\tilde{P}_g + \frac{2L_gP_{g0}}{3v_{gd}^2}\frac{d\tilde{P}_g}{dt}\right) - \frac{2L_gQ_{g0}}{3v_{gd}^2}\frac{d\tilde{Q}_g}{dt} \tag{3.56}$$

Assuming the reactive power injected into the grid is Q_{g0}=0 VAR, and taking the Laplace transform of (3.56) produces

$$\frac{1}{2}C_{dc}s\tilde{V}_{dc}^{\ 2} = \tilde{P}_s - \left(\tau_g s + 1\right)\tilde{P}_g \tag{3.57}$$

$$\tau_g = \frac{2L_gP_{g0}}{3V_{gd}^2} \tag{3.58}$$

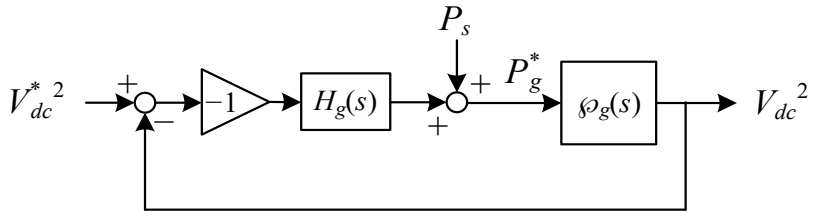

Fig. 3.7. The GSC DC-link voltage control loop.

Ignoring the stator power on (3.57), the transfer function between the DC-link voltage and the grid active power is

$$H_g(s) = \frac{\tilde{V}_{dc}^{\ 2}}{\tilde{P}_g} = -\frac{2}{C_{dc}}\frac{\tau_g s + 1}{s} \tag{3.59}$$

Because of the linear relation between P_g and i_{td} expressed in equation (3.52), the active grid power closed-loop gain is equal to the current closed-loop gain given by

$$G_p(s) = \frac{\tilde{P}_g}{\tilde{P}_g^*} = \frac{i_{gd}}{i_{gd}^*} = \frac{1}{\tau_i s + 1} \tag{3.60}$$

Therefore, combing (3.59) and (3.60), the overall DC-link voltage plant model is

$$\wp_g(s) = \frac{\tilde{V}_{dc}^{\,2}}{\tilde{P}_g^*} = -\frac{2(\tau_g s + 1)}{C_{dc} s(\tau_i s + 1)} \tag{3.61}$$

With the plant model, the DC-link voltage open-loop gain of the control loop that is described in Fig. 3.7 is

$$\ell_g(s) = -H_g(s)\wp_g(s) \tag{3.62}$$

where H_g is the DC-link voltage controller. If H_g is designed as an integrator that has unity gain at the designed crossover frequency, ω_{cv}, then the integration parameter will be

$$k_{iv} = \left| \frac{C_{dc}\omega_{cg}^{\,2}(j\tau_i\omega_{cv} + 1)}{2(j\tau_g\omega_{cv} + 1)} \right| \tag{3.63}$$

To design the value of k_{iv}, the crossover frequency is needs to be smaller than the inner loop bandwidth, so it is chosen to be a fifth of the inner current loop bandwidth. Because the phase margin decreases with smaller values of τ_g, the closed-loop system may become unstable [37]. The minimum value of τ_g for the GSC occurs when the grid power is zero during LVRT, which results in τ_g=0 from (3.58). When τ_g=0, the open-loop gain with just the integrator compensator is

$$\ell_g(s) = \frac{2k_{iv}}{C_{dc}s^2(\tau_i s + 1)} \tag{3.64}$$

With the designed crossover frequency, the phase of the open-loop gain at the crossover frequency is $\angle \ell_g(j\omega_{cv}) = -169^\circ$, so the phase margin is only 11°. Therefore, a lead compensator is required to ensure system stability for the worse case of $\tau_g=0$ by boosting the phase margin. The lead compensator is designed as

$$H_g(s) = h_g \frac{s + p_g/\alpha_g}{s + p_g} \tag{3.65}$$

$$\alpha_g = \frac{1+\sin(\delta_g)}{1-\sin(\delta_g)}, \quad \alpha_g > 1 \tag{3.66}$$

$$p_g = \sqrt{\alpha_g}\,\omega_{cv} \tag{3.67}$$

where δ_g is the design specific filter angle that increases the phase margin for the case of $\tau_g=0$, and h_g is the filter gain designed such that the open-loop gain at the cross over frequency is unity.

3.3 PMSG LVRT control strategies

For VSC-based PMSGs, the main concern during LVRT is the overvoltage of the DC-link capacitor. In this thesis, the LVRT methods that are studied for the PMSG are the DCC, the SEIRI, and the hybrid method. The DCC is a hardware-based method that dissipates the excess power by switching in a resistor in parallel with the DC-link. The SEIRI is a control-based method that stores the excess power in the wind turbine's inertia by altering the control of the MSC from MPPT to DC-link control. Finally, the hybrid method is a hardware- and control-based approach that combines the DCC method with SEIRI method.

3.3.1 DC crowbar LVRT Method

The WECS with a DCC can be modelled with the equivalent circuit given in Fig. 3.8, and the electrical dynamics of the equivalent circuit can be written as

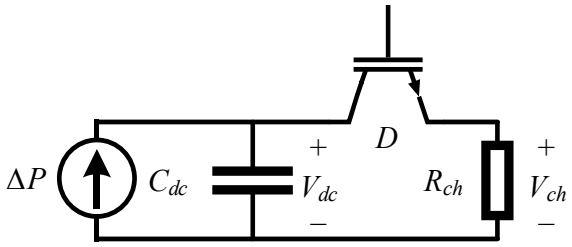

Fig. 3.8. The DCC equivalent circuit model.

$$\frac{1}{2}C_{dc}\frac{d}{dt}V_{dc}^{\ 2} = \Delta P - P_{ch} \tag{3.68}$$

where P_{ch} is the power dissipated by the DCC and R_{ch} is the chopper resistance. For the PMSG WECS, the power difference is $\Delta P = P_s - P_g$. From (3.68), the DCC plant model is

$$\wp_{ch}(s) = \frac{V_{dc}^{\ 2}}{P_{ch}} = \frac{-2}{C_{dc}s} \tag{3.69}$$

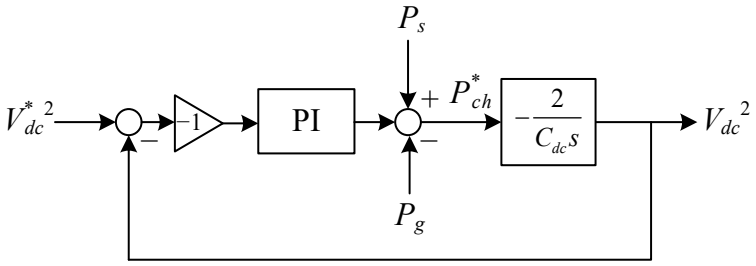

Fig. 3.9. The DCC LVRT DC-link voltage control loop.

Using this plant model, the control loop using a PI controller is given in Fig. 3.9. The integral parameter is set to zero to maximize the control robustness, and the proportional parameter is set to achieve unity gain at the control bandwidth of $1/\tau_i$

$$k_{pch} = \frac{-C_{dc}}{2\tau_i} \tag{3.70}$$

The DCC is activated using duty cycle control. When the switching period is small, the DC-link voltage can be assumed to be constant over each switching interval, so the average chopper power can be written as

$$P_{ch} = \frac{1}{T}\int_{t_0}^{t_0+T} \frac{{V_{ch}}^2}{R_{ch}} dt = \frac{D{V_{dc}}^2}{R_{ch}} \tag{3.71}$$

where T is the switching period and D is the duty cycle. Therefore, the required duty cycle can be calculated from the reference chopper power that is outputted from DCC controller by

$$D^* = \frac{P_{ch}^* R_{ch}}{{V_{dc}}^2} \tag{3.72}$$

Since the duty cycle may not necessarily be constant, the duty cycle will be sampled every two-switching period.

3.3.2 SEIRI LVRT Method

The SEIRI LVRT method uses the MSC to control the DC-link voltage to prevent overvoltage during LVRT. The DC-link voltage dynamic is still given by (3.45), and the method used to develop the GSC's DC-link controller can also be used to implement the MSC's DC-link controller. The MSC controls the DC-link by adjusting the stator power, which can be expressed as

$$P_s = \frac{3}{2}\left(v_{sd} i_{sd} + v_{sq} i_{sq}\right) \tag{3.73}$$

Using the stator voltage dynamics given in (3.1) and (3.2), the stator power can be obtained as follows

$$\frac{3}{2} v_{sd} i_{sd} = \frac{3}{2}\left(-R_s {i_{sd}}^2 - L_s i_{sd} \frac{d}{dt} i_{sd} + \omega_r L_s i_{sq} i_{sd}\right) \tag{3.74}$$

$$\frac{3}{2} v_{sq} i_{sq} = \frac{3}{2}\left(-R_s {i_{sq}}^2 - L_s i_{sq} \frac{d}{dt} i_{sq} - \omega_r L_s i_{sd} i_{sq} + \omega_r \lambda_r i_{sq}\right) \tag{3.75}$$

Adding (3.74) with (3.75) yields the MSC power output.

$$P_s = \frac{3}{2}\left(-R_s(i_{sd}{}^2 + i_{sq}{}^2) - L_s i_{sd}\frac{d}{dt}i_{sd} - L_s i_{sq}\frac{d}{dt}i_{sq} + \omega_r \lambda_r i_{sq} \right) \tag{3.76}$$

A common method to control salient pole PMSG is using zero *d*-axis control (ZDC), so i_{sd}=0. Assuming the stator resistance is small, and using the linear relationship between the stator *q*-axis current and the EM torque in (3.4), then (3.76) can be written as

$$P_s \approx -\frac{2L_s T_e}{3(P\lambda_r)^2}\frac{d}{dt}T_e + T_e\omega_g \tag{3.77}$$

where the generator speed ω_g is equal to the angular stator frequency multiplied by number of pole-pair, *P*. Now substituting (3.77) into the DC-link voltage dynamic in (3.45) produces

$$\frac{1}{2}C_{dc}\frac{d}{dt}V_{dc}{}^2 \approx T_e\omega_g - \frac{2L_s T_e}{3(P\lambda_r)^2}\frac{d}{dt}T_e - P_g \tag{3.78}$$

Because of the nonlinearity term, (3.78) needs to be linearized to around the operating point (T_{e0}, ω_{m0}) producing

$$\frac{1}{2}C_{dc}\frac{d}{dt}\tilde{V}_{dc}{}^2 \approx \tilde{T}_e\omega_{g0} + T_{e0}\tilde{\omega}_g - T_{e0}\omega_{g0} - \frac{2L_s T_{e0}}{3(P\lambda_r)^2}\frac{d}{dt}\tilde{T}_e - \tilde{P}_g \tag{3.79}$$

Now taking the Laplace transform of (3.79), and using $P_{s0}\approx T_{e0}\omega_{g0}$ gives

$$\frac{1}{2}C_{dc}s\tilde{V}_{dc}{}^2 \approx T_{e0}(\tilde{\omega}_g - \omega_{g0}) + \tilde{T}_e\omega_{g0}(\tau_s s + 1) - \tilde{P}_g \tag{3.80}$$

$$\tau_s = -\frac{2L_s P_{s0}}{3(P\omega_{g0}\lambda_r)^2} \tag{3.81}$$

From (3.80), the transfer function between $\tilde{V}_{dc}^{\,2}$ and $\tilde{T}_{e0}\omega_{g0}$ is

$$H_s(s) = \frac{\tilde{V}_{dc}^{\,2}}{\tilde{T}_e\omega_{g0}} = \frac{2}{C_{dc}}\frac{\tau_s s+1}{s} \tag{3.82}$$

Since the EM torque is proportional to the q-axis stator current, the closed-loop gain of the EM torque inner loop is equal to that of the stator current

$$G_T(s) = \frac{T_e}{T_e^*} = \frac{i_{sq}}{i_{sq}^*} = \frac{1}{\tau_i s+1} \tag{3.83}$$

Therefore, the plant model that relates the DC-link power and the output active grid power reference is

$$\wp_s(s) = \frac{\tilde{V}_{dc}^{\,2}}{\tilde{T}_e^*\omega_{g0}} = \frac{2(\tau_s s+1)}{C_{dc}s(\tau_i s+1)} \tag{3.84}$$

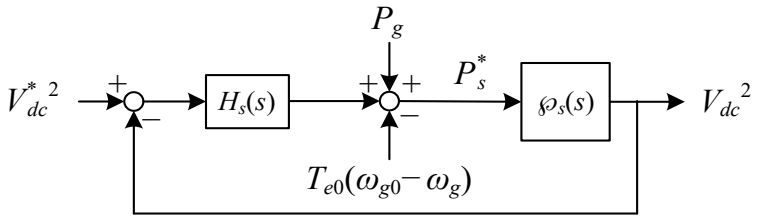

Fig. 3.10. The SEIRI LVRT DC-link voltage control loop.

With this plant model, the DC-link voltage open-loop gain of the control loop that is described in Fig. 3.10 is

$$\ell_s(s) = H_s(s)\wp_s(s) \tag{3.85}$$

Where H_s is the DC-link voltage controller. Assuming H_s is designed as an integrator, the open-loop gain is

$$\ell_s(s) = \frac{2k_{iv}(\tau_s s + 1)}{C_{dc} s^2 (\tau_i s + 1)} \tag{3.86}$$

For the MSC's DC-link voltage control, the best-case scenario for the phase margin occurs when τ_s=0, which occurs when P_{s0} is zero. Using the designed crossover frequency of one-fifth of the inner current loop bandwidth, the phase of the open-loop gain at crossover frequency when τ_s=0 is $\angle \ell_s(j\omega_{cv}) = -169^\circ$, so the phase margin is 11°. Therefore, the phase margin will be even smaller for the worse-case scenario when $\tau_s = \tau_{s\min}$, which occurs when P_{s0} is equal to the rated stator power. Therefore, a lead compensator is again required to ensure stability by increasing the phase margin. The lead compensator is designed as

$$H_s(s) = h_s \frac{s + p_s / \alpha_s}{s + p_s} \tag{3.87}$$

$$\alpha_s = \frac{1 + \sin(\delta_s)}{1 - \sin(\delta_s)}, \quad \alpha_s > 1 \tag{3.88}$$

$$p_s = \sqrt{\alpha_s}\,\omega_{cv} \tag{3.89}$$

where δ_s is the design specific filter angle that increases the phase margin for the case of $\tau_{s\min}$, and the h_s is the designed filter gain that results in unity open-loop gain at the cross over frequency.

3.3.3 Hybrid LVRT Method

The hybrid LVRT method combines the SEIRI LVRT method with the DCC by proportioning the excess power between the two methods. As a reminder, the WECS with a DCC can be modelled by the equivalent circuit in Fig. 3.8, and the dynamic equation of this circuit is given in (3.68). In the case of the standalone DCC and the standalone SEIRI method, the DC-link voltage is closed-loop controlled to regulate the DC-link at the rated condition. However, in the hybrid

case, if both methods utilize closed-loop DC-link voltage control, there may be unexpected conflicts between the two controllers. To avoid this conflict, the SEIRI method is closed-loop controlled, while the DCC method is open-loop controlled.

The open-loop DCC control is done by calculating the duty cycle needed through (3.72) using a desired P_{ch}^{*} that is dissipated by the DCC. One way to set P_{ch}^{*} is by applying a predetermined ratio, α, to the surplus power such as

$$P_{ch}^{*} = \alpha(P_{s0} - P_{g}) \tag{3.90}$$

where P_{s0} is the normal operation stator power. The controller design of the closed-loop SEIRI method is the same as before. However, the SEIRI control loop is modified to Fig. 3.11 to include the impact of the DCC.

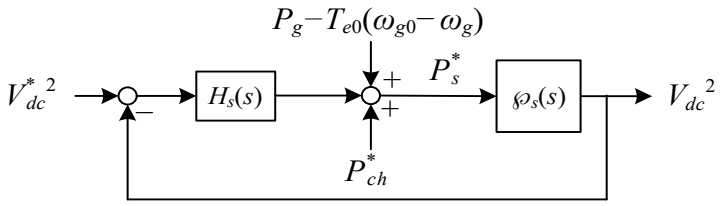

Fig. 3.11. The Hybrid LVRT DC-link voltage control loop

3.4 Evaluation of PMSG LVRT strategies under symmetrical and asymmetrical faults

Simulations are performed on MATLAB/Simulink using the simulation parameter in Table 3.1 to compare the electrical and mechanical performance of the three LVRT methods under symmetrical and asymmetrical grid faults. For asymmetrical fault, the grid power will oscillate at the twice the grid's fundamental frequency when the negative sequence current is set to zero. In this paper, two LVRT scenarios are simulated by reducing the grid voltage to 0.1 pu for 150 ms under one-phase asymmetrical and three-phase symmetrical voltage dips. Once the fault is cleared, the Ireland and UK active ramp rate of 90% of the rated power per second is implemented instead of the E.ON ramp rate of 20% to reduce simulation time [39].

To assess the LVRT methods' lifetime impact, the normal operation bending and torsional stresses are required. The rated power rating is 2.45 MW for the PMSG that is used in the simulation. However, only the shaft parameters for NREL 5 MW is readily available, so the 5 MW shaft parameter will be used to estimate the bending stress for a 2.45 MW WT. For the NREL 5MW, the rotor mass is 110,000 kg, and the center of mass is positioned 1.912 m from the main bearings [41]. From (2.9), the maximum bending moment at the main bearings is M_b=2.063 MNm. The bending and torsional stress-concentration factors are computed for round shafts with a singe fillet using [42], which are K_f=1.618 and K_{fs}=1.305, respectively. The shaft torque is T_s=1.872 MNm from dividing the WT's rated power with the rotational speed of the main shaft. The shaft diameter of the NREL 5 MW WT is 0.8 m, so the bending stress at the top and bottom of the shaft at main bearings is 66.4 MPa using (2.10), and the midrange torsional stress at the outer shell of the shaft using (2.11) is 42.1 MPa.

Next, the modified SN curve for the WT shaft is needed to approximate the damage of the shaft. The WT shaft is assumed to be composed of an AISI 4140 grade steel with a tensile and yield strength of 951 MPa and 834 MPa, respectively [31]. Using the procedure in section 5.B.3 of the GL guidelines, the parameters of the modified SN curve are found to be N_e=1.02×10^6 cycles, $\Delta\sigma_e^*$=202.59 MPa, and m_1=6.389. The resulting modified SN curve in the log scale is shown in Fig. 3.12.

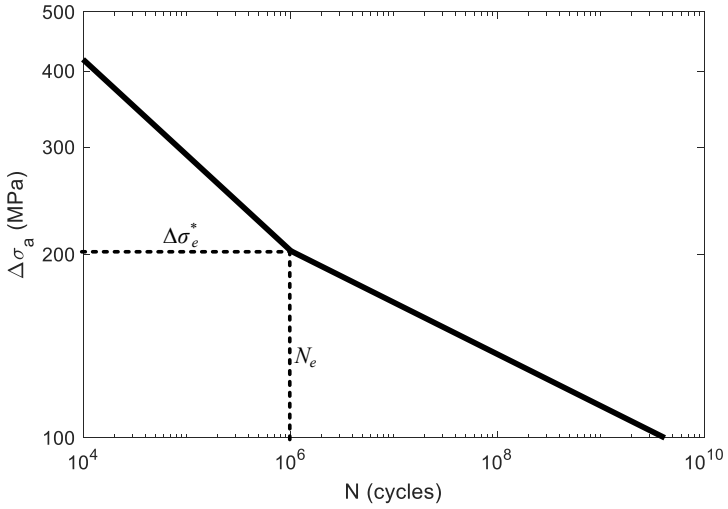

Fig. 3.12. The modified SN curve for 4140 steel using the GL WT guidelines.

3.4.1 Simulation results analysis of the DCC LVRT method

For the DCC LVRT method, the excess power is dissipated by adjusting the duty cycle of the DCC. The crowbar resistance is calculated from (3.72) using the maximum DC-link power as the DC chopper power. The power that charges the DC-link is given by

$$P_{dc} = P_s - P_g \tag{3.91}$$

Under the DCC method, the stator power remains as the rated WT power represented by P_0, so the maximum DC power will occur at the minimum grid power. The grid power can be expressed by

$$P_g = P_{gdc} + P_{gc}\cos(2\omega t) + P_{gs}\sin(2\omega t) \tag{3.92}$$

where P_{gdc} is the average component of the grid power, and P_{gc} and P_{gs} are the amplitudes of the 2nd order grid power harmonics caused by the asymmetrical voltage dip. Assuming that the negative sequence components of the grid current are controlled to zero and that the positive sequence q-axis grid voltage is zero from the PLL, then P_{gdc}, P_{gc}, and P_{gs} can be given by

$$P_{gdc} = \frac{3}{2} v_{gd}^{+} i_{gd}^{+} \tag{3.93}$$

$$P_{gc} = \frac{3}{2}(v_{gd}^{-} i_{gd}^{+} + v_{gq}^{-} i_{gq}^{+}) \tag{3.94}$$

$$P_{gs} = \frac{3}{2}(-v_{gd}^{-} i_{gq}^{+} + v_{gq}^{-} i_{gd}^{+}) \tag{3.95}$$

where v_{gd}^{+} is the positive sequence d-axis grid voltage, v_{gd}^{-} and v_{gq}^{-} are the negative sequence dq-frame grid voltages, and i_{gd}^{+} and i_{gq}^{+} are the positive sequence dq-frame grid currents. Now, substituting (3.93)–(3.95) into (3.92), and then applying the trigonometric identity for $a\cos x + b\sin x = R\cos(x-\alpha)$ yields

$$P_g = \frac{3}{2}\left(v_{gd}^{+}i_{gd}^{+} + \sqrt{v_{gd}^{-\,2} + v_{gq}^{-\,2}}\sqrt{i_{gd}^{+\,2} + i_{gq}^{+\,2}}\cos\left(2\omega t - \alpha_p\right)\right) \tag{3.96}$$

$$\alpha_p = \tan^{-1}\left(\frac{-v_{gd}^{-}i_{gq}^{+} + v_{gq}^{-}i_{gd}^{+}}{v_{gd}^{-}i_{gd}^{+} + v_{gq}^{-}i_{gq}^{+}}\right) \tag{3.97}$$

The minimum grid power can be found by minimizing the DC and AC components. The minimum DC component of the grid power is P_{gdc}=0, which occurs when i_{gd}^{+}=0. Because of the sinusoidal nature of the AC power component, the minimum AC power occurs when the AC amplitude is maximized. Assuming the grid voltage phase amplitudes are V_a=$x\sqrt{2/3}V_0$ V_b=$y\sqrt{2/3}V_0$, and V_c=$z\sqrt{2/3}V_0$, where V_0 is the rated RMS grid voltage and $0 \le x, y, z \le 1$, then

$$v_{gd}^{-} = \frac{-2x + y + z}{6}\sqrt{2/3}V_0 \tag{3.98}$$

$$v_{gq}^{-} = \frac{\sqrt{3}(y - z)}{6}\sqrt{2/3}V_0 \tag{3.99}$$

$$\sqrt{v_{gd}^{-\,2} + v_{gq}^{-\,2}} = \frac{\sqrt{2/3}V_0}{3}\sqrt{x^2 + y^2 + z^2 - xy - xz - yz} \tag{3.100}$$

Now, through current control

$$\sqrt{i_{gd}^{+\,2} + i_{gq}^{+\,2}} = \sqrt{2}I_0 \tag{3.101}$$

where I_0 is the rated RMS grid current and is constant, so the maximum amplitude of the AC power component occurs for the grid voltage conditions that maximizes (3.100), which is when the radicand equates to one, and occurs when one or two phases of the grid voltage drops to 0 pu. Therefore, the minimum AC power is $-\frac{1}{3}P_0$, where P_0=$\sqrt{3}V_0I_0$, and with a zero average grid power, the maximum DC-link power is P_{dc}=$\frac{4}{3}P_0$ from (3.91). By using this as the required DC chopper power

under unity duty cycle in (3.72), the minimum crowbar resistance that is required is R_{ch}=15 Ω, but R_{ch}=12.5 Ω is chosen to allow for potential variance in the power difference between the generator and the grid.

Table 3.1 PMSG simulation Parameters

Variable	Description	Value
	Wind Turbine Parameters	
P_w	Rated Wind Power [MW]	2.45
r	Turbine Blade Length [m]	57.5
ρ	Air Density [kgm^2]	1.225
$C_{p,opt}$	Optimal Rotor Efficiency	0.48
λ_{opt}	Optimal Tip Speed Ratio	8.1
n_t	Rated Turbine Speed [rpm]	12.5
v_w	Rated Wind Speed[m/s]	9.29
	Drive Train Parameters	
J_t	Wind Turbine Inertia [kgm^2]	1.230×10^7
J_g	PMSG Inertia [kgm^2]	1.955×10^3
K_s	Shaft Stiffness [Nm/rad]	6.671×10^8
D_s	Shaft Mutual Damping [Nm/(rad/s)]	3.389×10^6
N_{gb}	Gear Box Ratio	32
	PMSG Parameters	
P_s	Rated Generator Power [MW]	2.45
f_s	Rated Stator Frequency [Hz]	53.33
n_g	Rated Generator Speed [rpm]	400
P	Pole Pairs	8
ψ_r	Rated RMS Rotor Flux [Wb]	4.971
R_s	Stator Winding Resistance [mΩ]	24.21
L_{sd}	*d*-axis Synchronous Inductance [mH]	9.816
L_{sq}	*q*-axis Synchronous Inductance [mH]	9.816
	Grid Parameters	
S_g	Rated Apparent Grid Power [MVA]	2.45
V_g	Rated Grid Voltage [V]	4000
I_g	Rated Grid Current [A]	353.6
f_{gr}	Grid Frequency [Hz]	60
L_g	Inverter Filter Inductance [mH]	3.2
R_g	Inverter Resistance [mΩ]	25
	WECS Parameters	
V_{dc}	DC-link Voltage [V]	7000
C_{dc}	DC-link Capacitance [mF]	2
f_{sw}	Switching frequency [Hz]	3420

The performance of the DCC LVRT method under symmetrical and asymmetrical voltage dip to 0.1 pu is shown in Fig. 3.13 and Fig. 3.14, respectively. When the grid voltage drops to 0.1 pu, all the rated current is allocated towards for reactive power ancillary services according to the E. ON grid code in Fig. 2.1. This done by setting the grid current references of the GSC controller to i_{gd}^{*}=0 pu and i_{gq}^{*}=−1 pu.

For a symmetrical voltage dips to 0.1 pu, the positive sequence *dq*-frame grid voltages are v_{gd}^{+}=0.1 pu and v_{gq}^{+}=0 pu, and the negative sequence grid voltage is zero. From Figs. 3.13 (b)-(c), the *dq*-frame grid currents are controlled to i_{gd}=0 pu and i_{gq}=−1 pu. As a result, the average active grid power is P_g=0 pu and the average reactive power is Q_g=0.1 pu, as shown in Figs. 3.13(f)-(g).

For asymmetrical voltage dips, with phase A dropping to 0.1 pu, the positive sequence *dq*-frame grid voltages are v_{gd}^{+}=0.7 pu and v_{gq}^{+}=0 pu, and the negative sequence *dq*-frame grid voltages are v_{gd}^{-}=0.3 pu and v_{gq}^{-}=0 pu. Because the grid current references are set to i_{gd}^{*}=0 pu and i_{gq}^{*}=−1 pu, the active grid power is still P_g=0 pu, but the average reactive power is Q_g=0.7 pu. Since the negative sequence current is not controlled to minimize the power oscillation, the active and reactive power will oscillate at twice the fundamental frequency with an amplitude of 0.3 pu.

Under both symmetrical and asymmetrical voltage dip conditions to 0.1 pu, the average DC-link power is equal to the rated power of P_0=2.45 MW because the average P_g=0 MW, which results in an average duty cycle of 0.625, as seen in Fig. 3.13(i) and Fig. 3.14(i). However, for asymmetrical voltage dip to 0.1pu, the maximum DC-link power is $^{13}/_{10}P_0$, so the maximum duty cycle is 0.8125 according (3.69), which matches the maximum duty cycle shown in Fig 3.14(i). For both types of voltage dips, the DCC can be maintain the DC-link voltage within 0.5% deviation from its rated value as shown in Fig. 3.13(h) and Fig. 3.14(h).

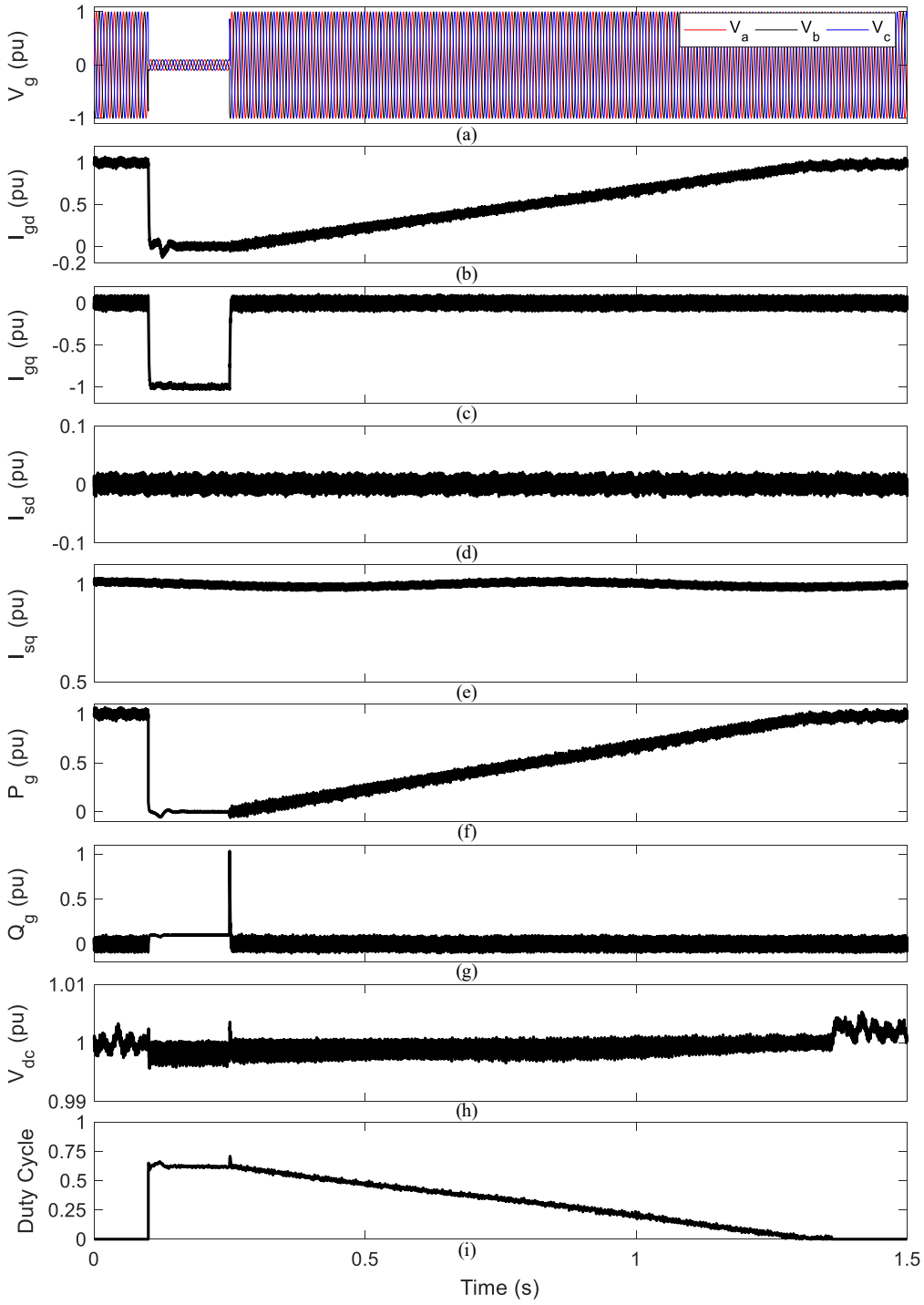

Fig. 3.13. The DCC LVRT electrical simulation results under symmetrical voltage dips to 0.1 pu with R_{ch}=12.5 Ω.

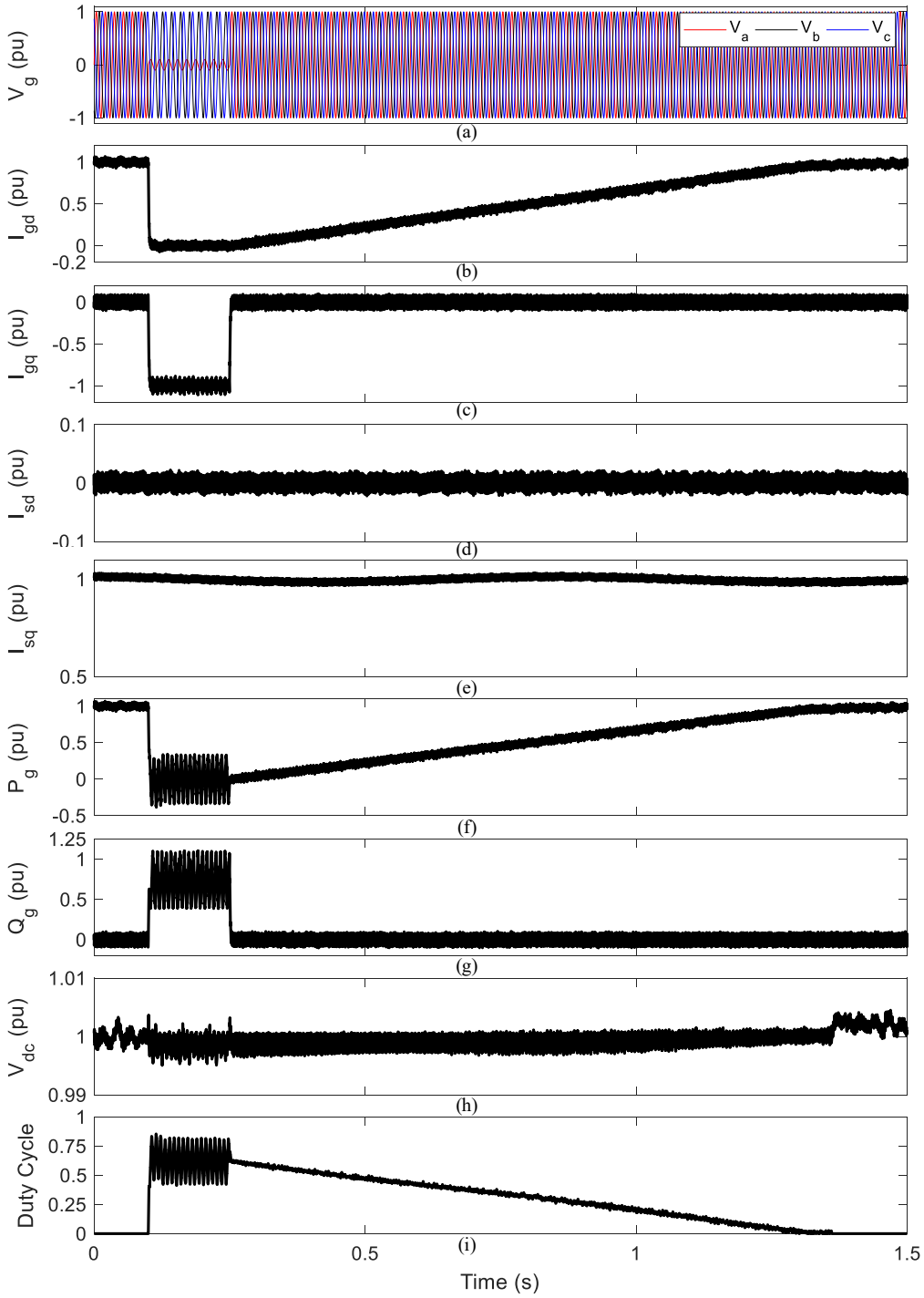

Fig. 3.14. The DCC LVRT electrical simulation results under asymmetrical voltage dips to 0.1 pu with R_{ch}=12.5 Ω.

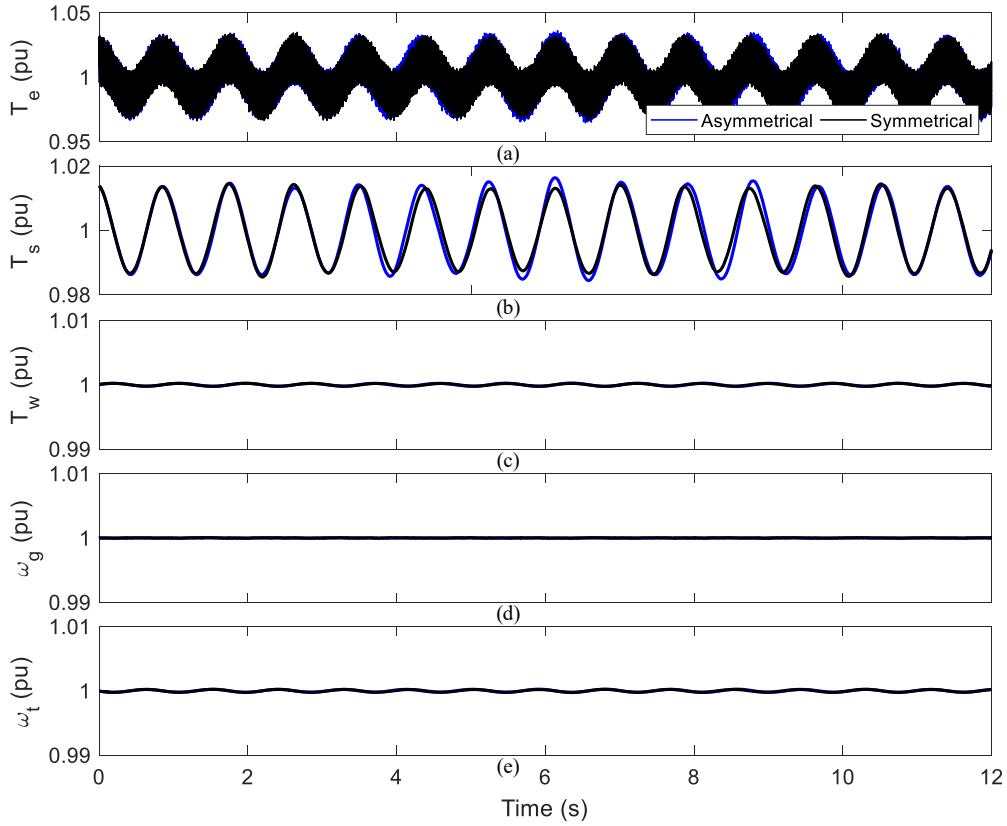

Fig. 3.15. The DCC LVRT mechanical simulation results under asymmetrical (blue) and symmetrical (black) voltage dips to 0.1 pu.

At the machine side, the MSC control is unchanged using the DCC method, so MPPT is still being maintained. Therefore, the stator *q*-axis current is 1 pu to generate the rated EM torque and the stator *d*-axis current is zero with ZDC control.

Once the fault is cleared, a 0.9 pu/s ramp rate is applied on the active grid power through a rate limiter on the *d*-axis grid current. During the grid power ramp, the DC-link will be charged because the stator power does not match the grid power, so the DCC remains on to protect the DC-link from overvoltage during the grid power ramp.

Since the DCC method does not alter stator side current, the stator power and EM torque are unchanged. Therefore, no mechanical transient appears on the drive-train system, as shown by the constant drivetrain torques and speeds in Fig. 3.15. In Fig. 3.15(a)-(b). The minor EM torque and shaft torque oscillations at the

drivetrain's natural frequency are a result of the steady-state drivetrain dynamics.

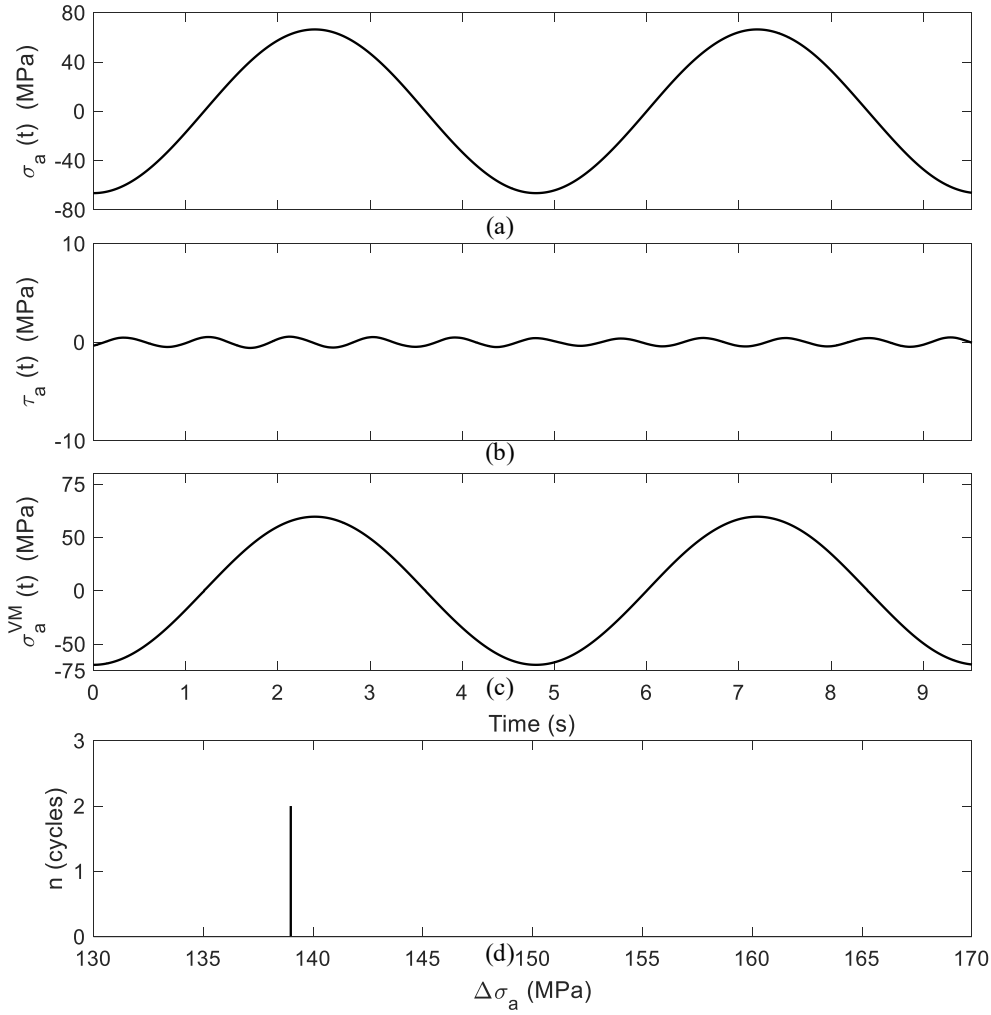

Fig. 3.16. The alternating bending stress, the alternating torque stress, the maximum von Mises stress, and the resultant rainflow count histogram using DCC.

Performing life analysis on the DCC method provides a stress-life benchmark of the WT under normal operation because the DCC method does not impact the mechanical system. Since the shaft torque simulation results are nearly identical under symmetrical and asymmetrical voltage dips to 0.1 pu, stress-life analysis will only be performed for the symmetrical voltage dip case. For a given stress element located at the main bearing, the waveforms of the alternating bending stress, the alternating torsional stress, and the equivalent uniaxial von Mise's stress over two stress cycles (9.6 s) for the DCC PMSG LVRT under a symmetrical voltage dip to

0.1 pu is shown in Fig. 3.16. The maximum alternating bending stress of the stress element at the main bearing is 66.4 MPa. Whereas the alternating torsional stress is approximately zero MPa because no transient appears on the shaft torque. As such, the resultant alternating von Mises's stress is equal to the bending stress. Applying RFC on the von Mises's stress yields two stress cycle with a stress range of 139 MPa, which is slightly larger than twice the maximum alternating bending stress after incorporating the midrange torsional stress of 42.1 MPa. Applying Palmgren-Miner's rule yields an accumulated damage of 2.32×10^{-6}%, which equates to a shaft life reduction of 9.6 s matching the normal operation lifetime reduction.

3.4.2 Simulation results analysis of the SEIRI LVRT method

Under the SEIRI LVRT method, the control of the MSC changes from MPPT to controlling V_{dc}, which reduces the stator power to match the grid power. Like the DCC method, under both symmetrical and one-phase grid voltage dip to 0.1 pu, the grid current is controlled to i_{gd}=0 pu and i_{gq}=−1 pu, as shown in Figs. 3.17(b)-(c) and Figs. 3.18(b)-(c). So, for symmetrical faults, the resultant average active and reactive grid powers are P_g=0 pu and Q_g=0.1 pu, as shown in Figs. 3.17(f)-(g). For one-phase faults, the average active and reactive power of grid are P_g=0 pu and Q_g=0.7 pu. In addition, the active and reactive grid power will oscillate at twice the grid's fundamental frequency with an amplitude of 0.3 pu, as shown in Figs. 3.18(f)-(g).

Under symmetrical voltage dips, the grid power is zero, so the stator power must drop to zero to match the grid power, which is done by reducing the EM torque through i_{sq}. However, the MSC has slower current dynamics because the stator inductance is larger than the grid inductance, which can be seen by comparing i_{gd} and i_{sq} in Fig. 3.17(b)-(e). Therefore, the stator power will reduce at a slower rate than the grid power, which results in a transient power difference between the stator and the grid that charges the DC-link capacitor. From Fig. 3.17(h), the transient charging causes the DC-link voltage V_{dc} to increase by 11% under symmetrical fault conditions. To regulate the DC-link voltage back to its rated value, the stator power becomes negative to transfer the capacitor's power to generator, which is done

under the SEIRI method by reducing i_{sq} to −0.62 pu, as shown in Fig. 3.17(e). Once V_{dc} is regulated back to its rated value, i_{sq} is then regulated back to zero.

For one-phase voltage dips, the average grid power is zero, but there are also power oscillations at the second harmonic. In this case, the stator power must also match the grid power oscillations to mitigate voltage ripples on the DC-link voltage. To do this, the average i_{sq} is still zero, but there is also a current ripple component from the DC-link voltage control, as shown in Figs. 3.18(e). However, some remnant DC-link voltage ripples are still present in Fig. 3.18(h), because the stator current control uses PI-based controllers, so there is inherently some degree of ripple rejection. For the one-phase voltage dip, the transient charging is smaller with the DC-link voltage increasing to only 6% in Fig. 3.18(h). Because the DC-link voltage increase is smaller for one-phase faults, less energy is required to be discharged from the DC-link, so i_{sq} only undershoots to −0.58 pu for one-phase faults, as shown 3.18(e).

Once the fault is cleared, the GSC resumes V_{dc} control with an active power ramp rate of 0.9 pu/s. Unlike the DCC method that applies a rate limiter on the *d*-axis grid current, the SEIRI method applies the rate limiter onto the *q*-axis stator current. Through the GSC DC-link control, the grid power will match the stator power, so the grid active power will also have a ramp rate of 0.9pu/s. In addition, the stator *q*-axis current is set to be allowed to increase up to 1.05 pu, so the stored rotation energy can be transferred to the grid, and the grid power will ramp up to 1.05 pu.

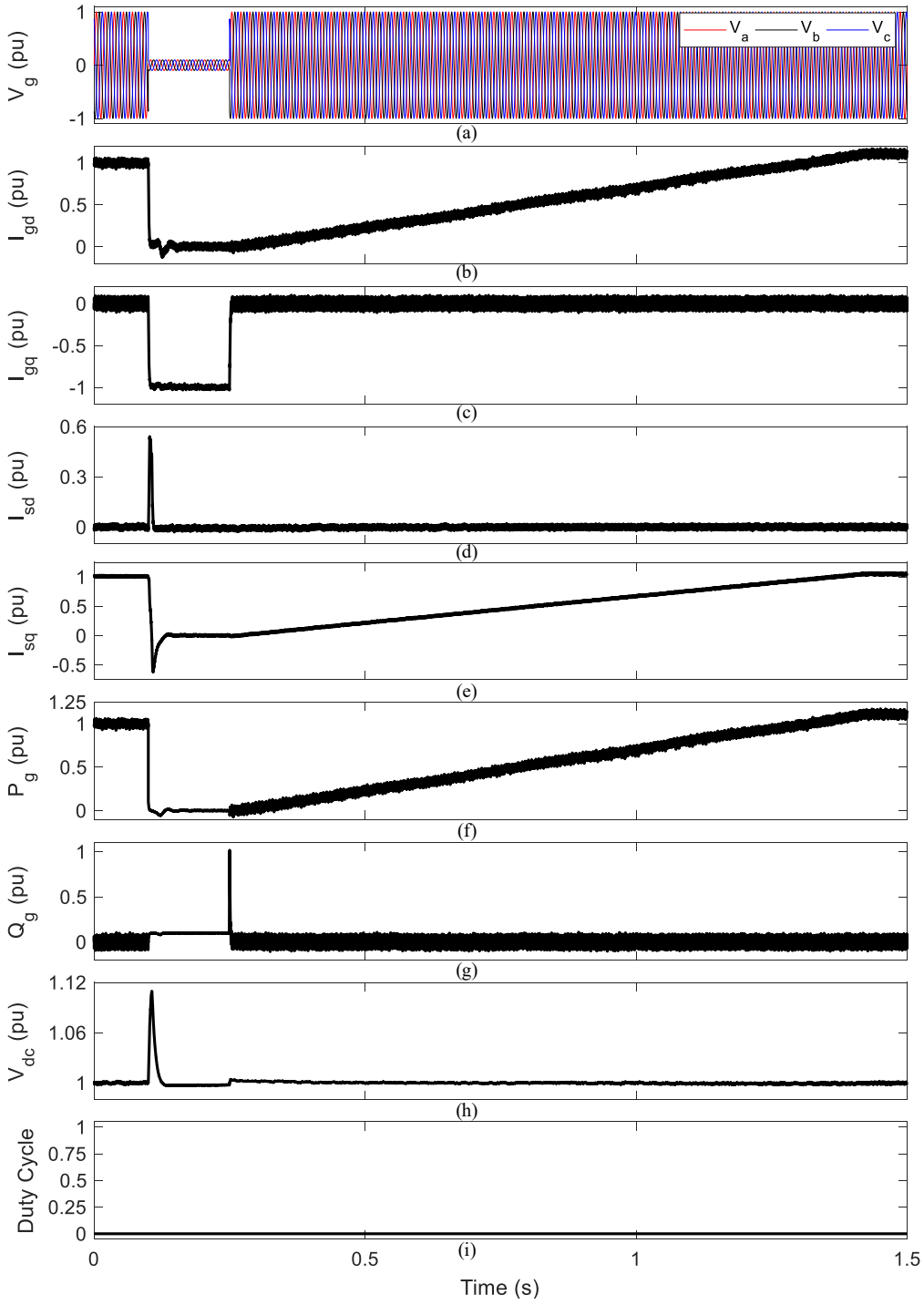

Fig. 3.17. SEIRI LVRT electrical simulation results under symmetrical voltage dip to 0.1pu.

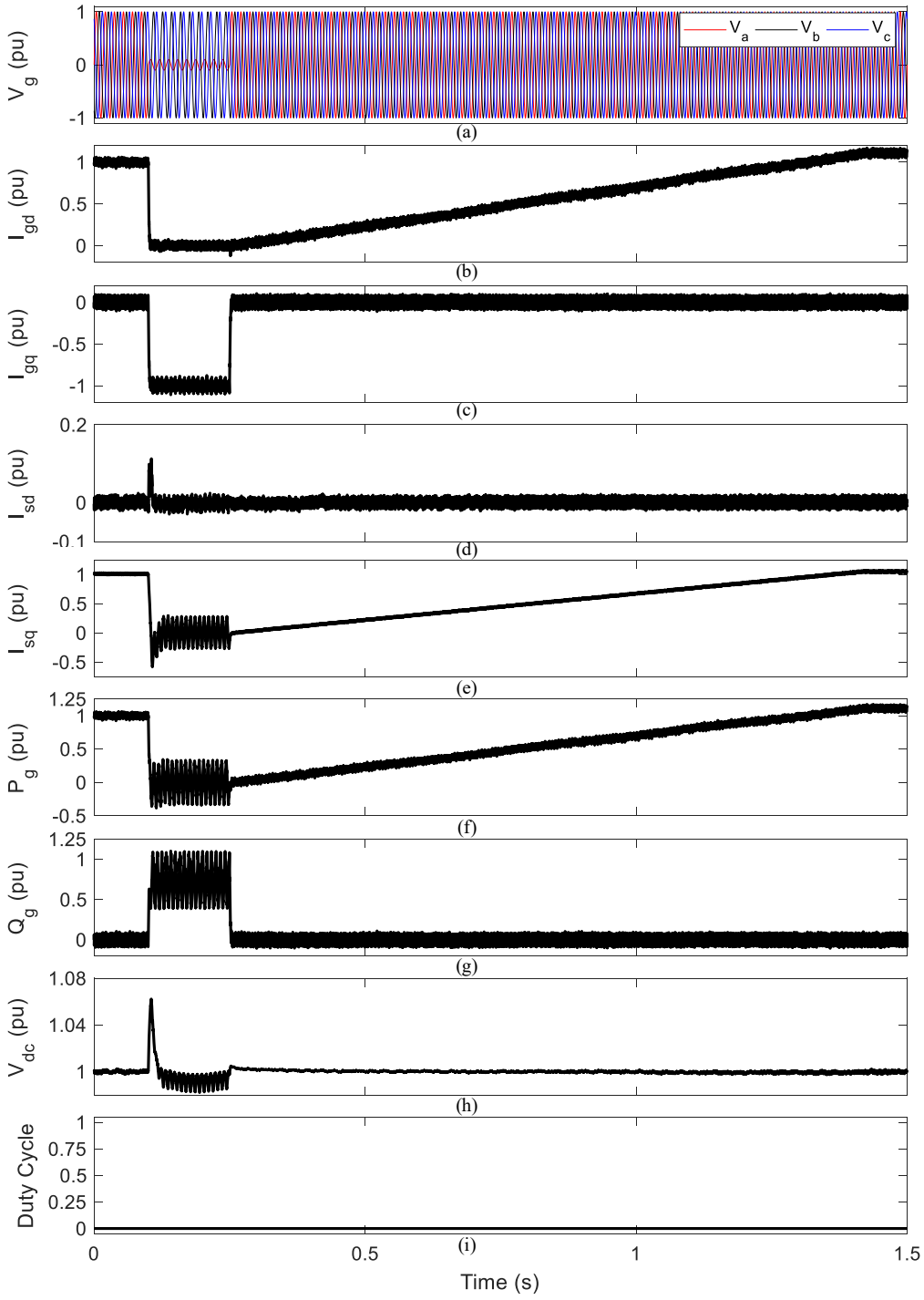

Fig. 3.18. SEIRI LVRT electrical simulation results under asymmetrical voltage dip to 0.1pu.

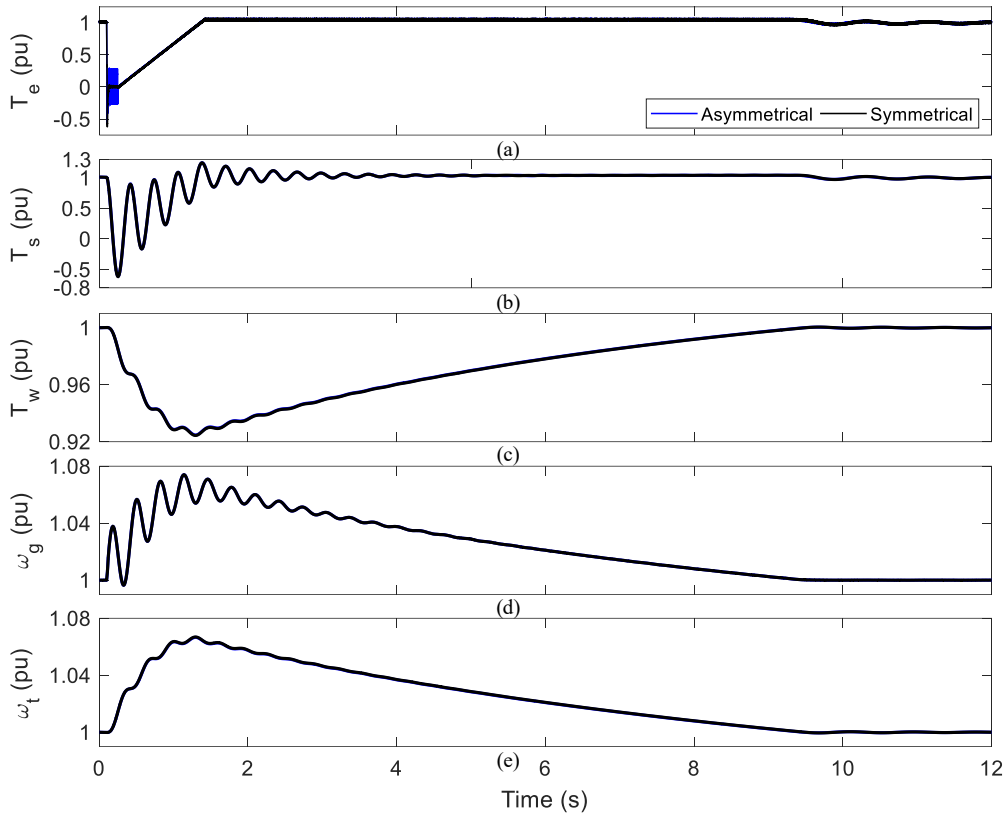

Fig. 3.19. SEIRI LVRT mechanical simulation results under asymmetrical (blue) and symmetrical (black) voltage dip to 0.1 pu.

In terms of mechanical performance, the SEIRI method reduces the average stator power and the EM torque to zero, which causes a mechanical transient on the shaft torque. For symmetrical faults, the EM torque drops from 1 pu to 0 pu to reduce the stator power to zero. For one-phase faults, the average EM torque is 0 pu, but there are also EM torque oscillation to account for the DC-link voltage ripples, as shown in Fig. 3.19(a). Although there are EM torque oscillation during one-phase faults, the mechanical drivetrain responses are nearly identical in Figs. 3.19(b)-(e). The drivetrain acts as a low pass filter with a natural frequency of 3.133Hz, which is much smaller than the frequency of EM torque oscillation at twice the fundamental frequency. Therefore, the oscillation EM torque will be filtered out and will have little impact on the mechanical response of the drivetrain.

In Fig. 3.19(b), when SEIRI LVRT is activated, the shaft torque T_s drops to down to −0.619 pu and −0.612 pu in response to the changes in the EM torque for

symmetrical and one-and two-phase faults, respectively. When the grid voltage is restored, the shaft torque increases at an average ramp rate of 0.9 pu/s, but also oscillates at the drive-train's natural frequency.

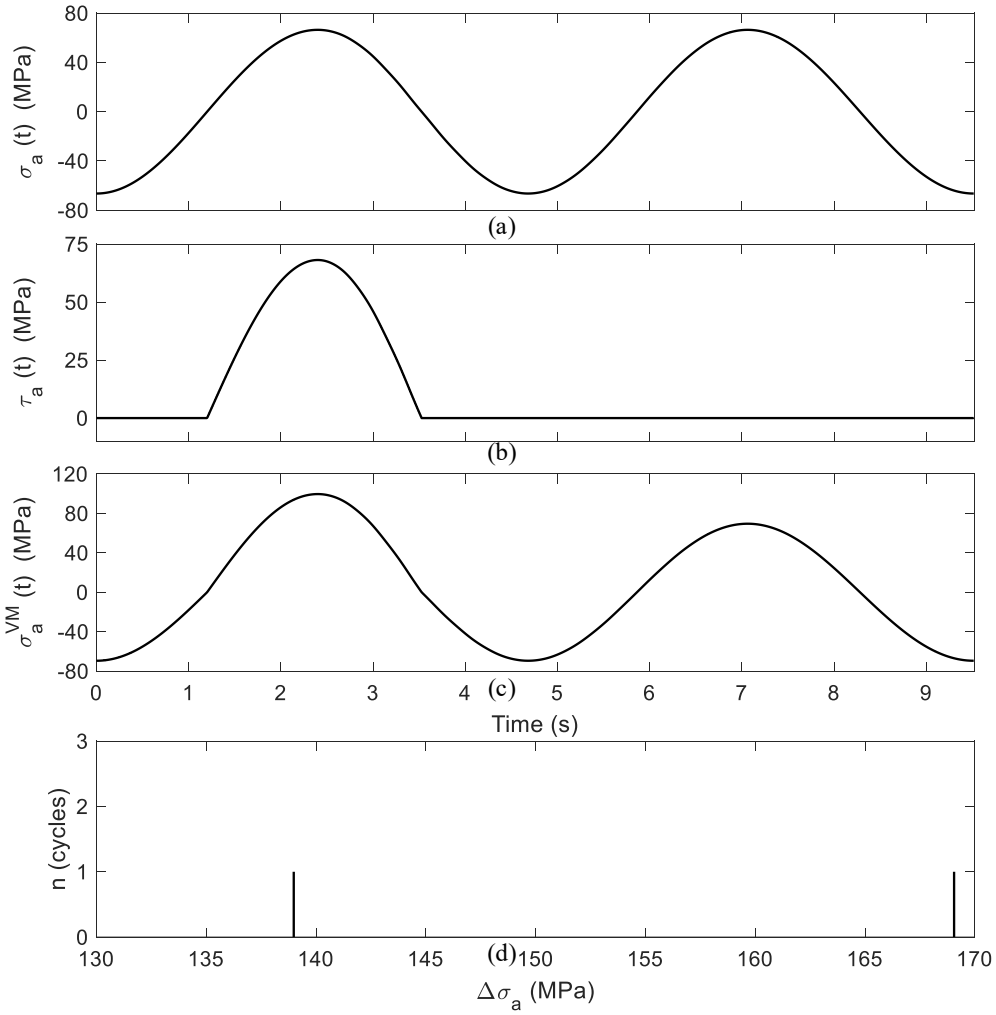

Fig. 3.20. The alternating bending stress, the alternating torque stress, the maximum von Mises stress, and the resultant rainflow count histogram using SEIRI.

During LVRT, the stator power drops to zero, so the power difference in the captured wind power and the stator power accelerates the turbine speed to store the excess power as rotational energy. Additionally, once the fault is cleared, because the stator power is limited by the ramp rate, there is still a power difference between the stator power and the captured wind power causing even more power to be stored as rotational energy. During the entire LVRT process, the rotor speed ω_g increases

by 7.4% and the turbine speed ω_t increases by 6.7% in Figs. 3.19(d)-(e), respectively. MPPT is forfeited from the acceleration of the turbine speed because the OTSR is no longer maintained resulting in additional loss. However, because the wind turbine speed does not accelerate significantly, the wind turbine is still operating relatively close to MPPT conditions, so a significant portion of the power is being stored as rotational energy.

Stress-life analysis will only be performed for the symmetrical voltage dip case because the shaft torques are nearly identical under both conditions. For the SEIRI method, there are significant transients on the shaft torque, so the alternating torsional stress is obtained by substituting the shaft torque response in Fig. 3.19(b) into (2.11) after subtracting the rated shaft torque. Since shaft torque oscillation is faster than the shaft's rotational speed, it is approximated that the minimum shaft torque is applied as one stress half-cycle at the shaft's rotational speed, as shown in Fig. 3.20(b). The alternating bending stress is unchanged with an amplitude of 66.4 MPa, and the maximum alternating torsional stress is 68.1 MPa. Combining the alternating bending and torsional stresses and incorporating the midrange torsion stress results in the alternating von Mises's stress with a maximum of 99.6 MPa, as portrayed in Fig. 3.20(c). Now, applying RFC on the von Mises's stress yields one stress cycle with a stress range of 139 MPa and another stress cycle with a stress range of 169 MPa. Applying Palmgren-Miner's rule yields an accumulated damage of 1.28×10^{-5}%, which is equivalent to a shaft life reduction of 53 s over the two shaft rotations or 9.6 s.

3.4.3 Simulation results analysis of the hybrid LVRT method

There are a few applications for the hybrid method. One potential application is to only activate crowbar to reduce transient overvoltage, while using the SEIRI as the main LVRT method. In addition, if a fully rated DCC is used, the SEIRI method can be turned off to prevent overspeeding, while the DCC maintains the DC-link voltage. Another application of the hybrid method is to predetermine the proportioning of the surplus power between the SEIRI and the DCC methods, which will be used in the following simulation.

For this simulation, the LVRT duration is split into two equal half-intervals. During the first interval, the hybrid method is used by activating both the DCC and the SEIRI LVRT methods. In the second interval, the DCC will be turned off, so only the SEIRI method will be operating. This results in two transients on the DC-link voltage, once at t=0.1 s caused by the initial grid voltage dip, and another at t=0.175 s caused by turning off the DCC. Since the SEIRI method can maintain the DC-link voltage by itself, the DC-link will remain at the rated value despite turning off the DCC.

The size of the DCC resistor will depend on the surplus power allocation ratio, α_p, between the DCC and the SEIRI method. In this simulation, the ratio is set to α_p=0.5, so half of the surplus is dissipated by the DCC, and the remaining half is stored using the SEIRI method. Because half of the excess power is allocated to the crowbar, the DCC resistance can be doubled of the standalone DCC, which will result in the same average duty cycle. However, if it is desired to dissipate the full power oscillation during asymmetrical faults, then an even smaller DCC resistance is needed. Previously, it has been determined that the minimum grid power is a third of the rated power, which occurs when one- or two-phase drops to 0 pu. Therefore, the maximum power that the DCC must be designed to dissipate is

$$P_{ch\mathrm{MAX}} = \alpha_p P_0 + \frac{1}{3} P_0 \tag{3.102}$$

For this simulation, the maximum DCC power under asymmetrical fault is $P_{ch\mathrm{MAX}}$=⅚P_0, so the minimum DCC resistor required is R_{ch}=24 Ω for unity duty cycle operation. In the simulation the DCC resistor is chosen to be 21.6 Ω.

Like the prior two methods, the grid current is controlled to i_{gd}=0 pu and i_{gq}=−1 pu for the voltage dips to 0.1 pu, as shown in Figs. 3.21(b)-(c) and Figs. 3.22(b)-(c). The active and reactive grid powers are P_g=0 pu and Q_g=0.1 pu under symmetrical faults, as shown in Figs. 3.21(f)-(g). Under one-phase voltage dips, the average active and reactive power of grid are P_g=0 pu and Q_g=0.7 pu with a power oscillation amplitude of 0.3 pu, as shown in Figs. 3.22(f)-(g).

During the hybrid interval, for a symmetrical voltage dip to 0.1 pu, the DCC is allocated half the rated power $P^*_{ch}=\frac{1}{2}P_0$, so the theoretical duty cycle is 0.54 with the designed DCC resistance of 21.6 Ω, which approximately matches the simulated duty cycle seen in Fig. 3.21(i). The SEIRI method only needs to absorb the remaining half of the surplus power, so the stator power and EM torque only needs to be reduced to half of its rated value. Therefore, the *q*-axis stator current only drops to 0.5 pu, as seen in Fig. 3.21(e).

For one-phase voltage dips to 0.1 pu, the maximum chopper power is $P^*_{ch}=\frac{4}{5}P_0$, so the theoretical maximum duty cycle is 0.864, which approximately matches the simulated duty cycle seen in Fig. 3.22(i). Because the DCC dissipates the DC-link power ripples, the SEIRI method only needs to remove half of the DC component of the surplus power. From Fig. 3.22(e), the *q*-axis stator current is 0.5 pu like the symmetrical case with minor ripples.

When the DCC is turned off at t=0.175 s, all the surplus power on the DC-link is stored using the SEIRI method. Therefore, the stator power needs to reduce to 0 pu to match the grid power, so the *q*-axis stator current reduces to i_{sq}=0 pu under symmetrical faults, as portrayed in Fig. 3.21(e). For asymmetrical faults, because the DCC is turned off, the SEIRI method must also account for the grid power oscillations. In Fig. 3.22(e), the average *q*-axis stator current reduces to 0 pu, but there is also a 0.3 pu amplitude ripple to eliminate the DC-link power ripples.

Comparing the DC-link voltage between the hybrid and the SEIRI method. One advantage is that the transient charging of the DC-link voltage is reduced because half of the transient power difference is dissipated by the DCC. From Figs. 3.21-3.22(h), the initial DC-link charging has been reduced from 1.08 pu to 1.05 pu and 1.06 pu to 1.03pu for symmetrical and one-phase faults, respectively. This demonstrates how the addition of a smaller DCC can be used to resolve the slower stator dynamics of the SEIRI method.

Like the standalone SEIRI method, the GSC resumes V_{dc} control and an active power ramp rate of 0.9 pu/s is applied using a rate limiter on the *q*-axis stator current when the grid voltage is restored. To transfer the stored energy back to the grid, the *q*-axis stator current can increase to 1.05 pu causing the grid power to ramp up to

1.05 pu.

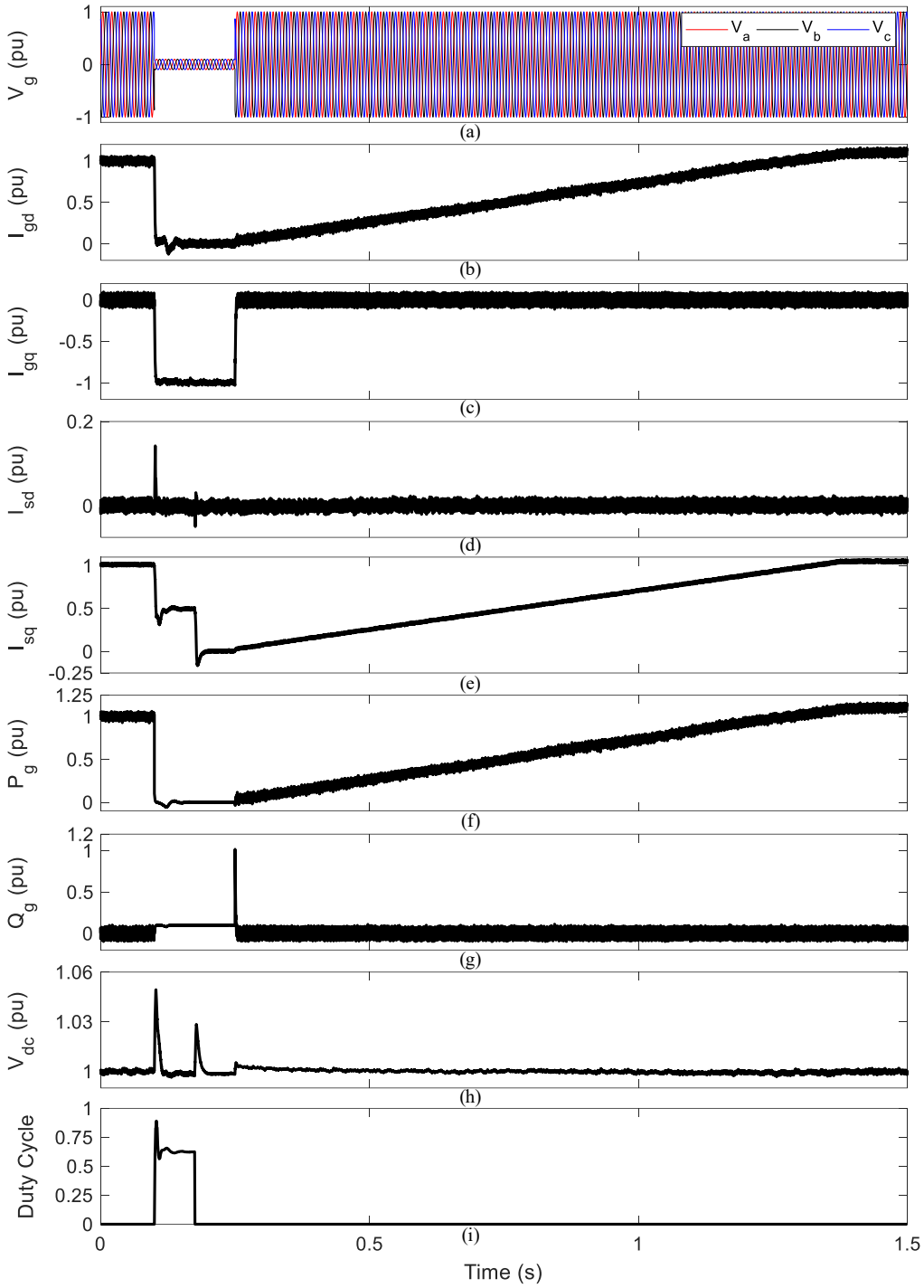

Fig. 3.21. Hybrid LVRT electrical simulation results under symmetrical voltage dip to 0.1pu with R_{ch}=21.6 Ω.

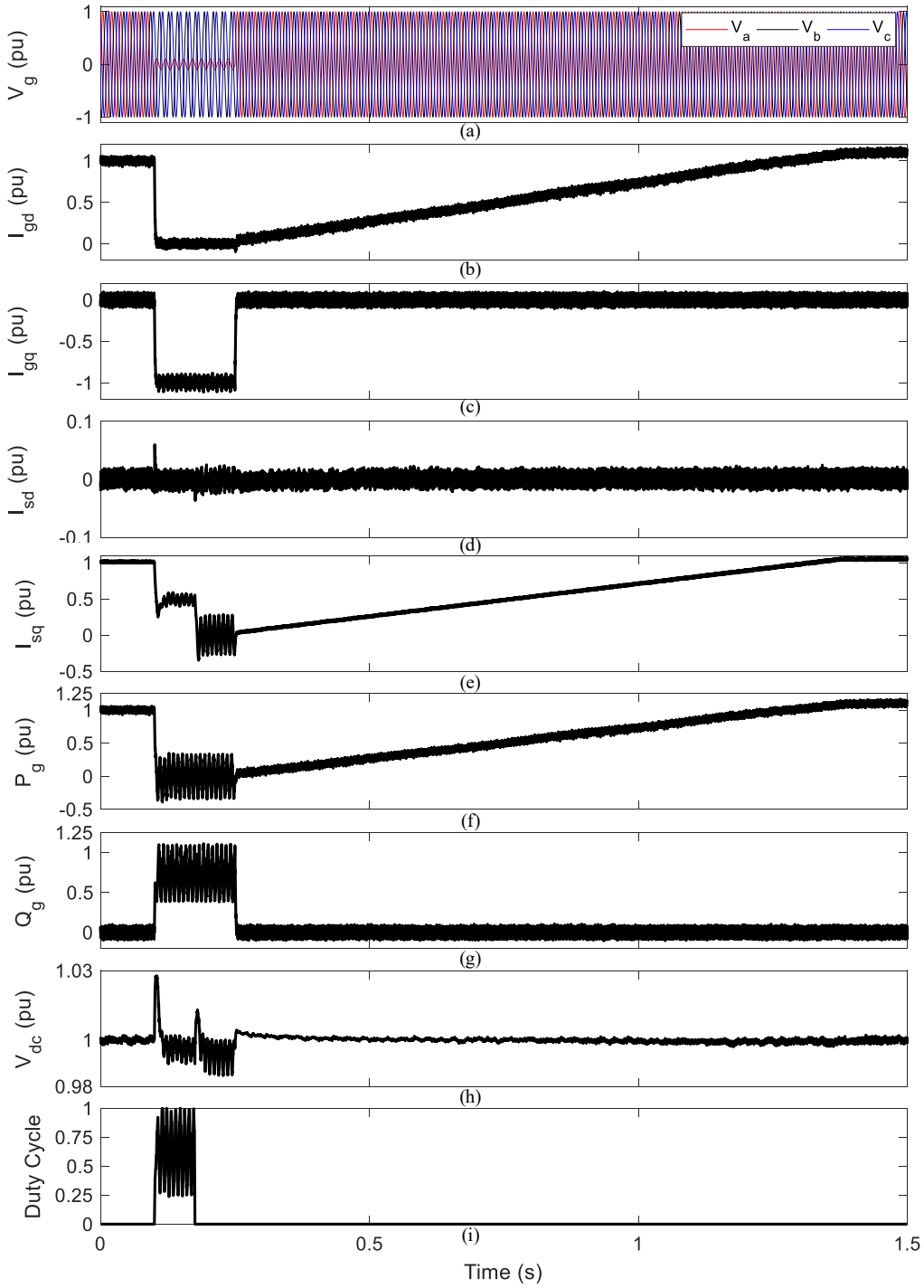

Fig. 3.22. Hybrid LVRT electrical simulation results under asymmetrical voltage dip to 0.1pu with R_{ch}=21.6Ω.

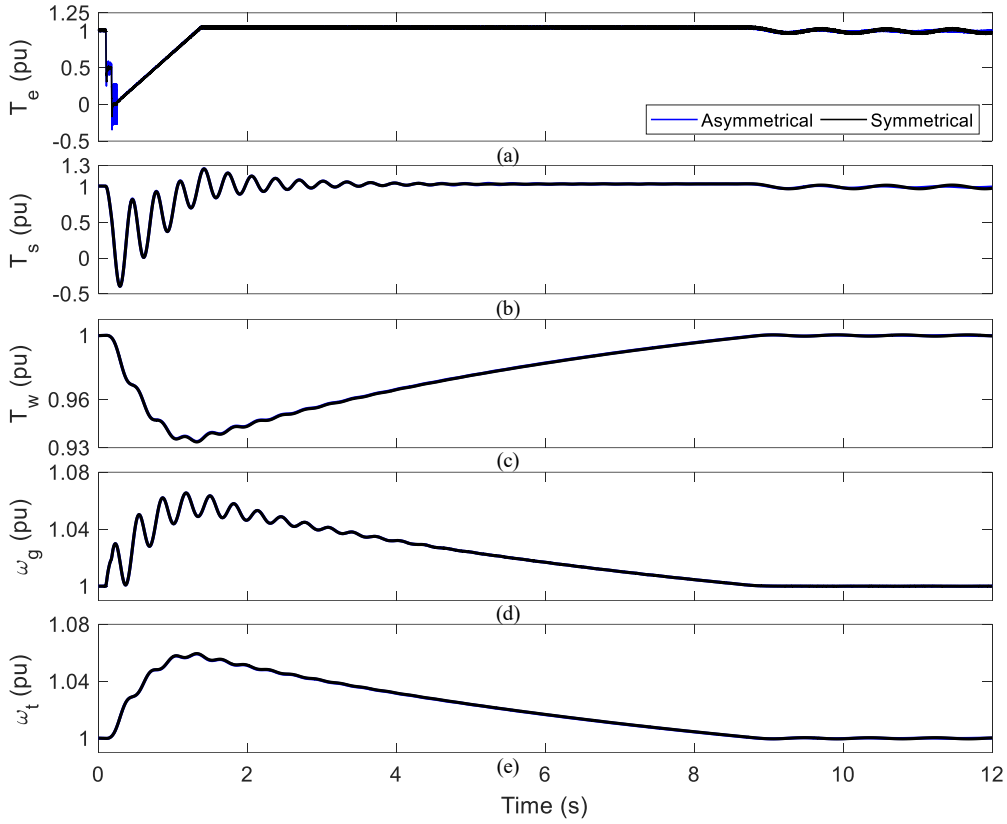

Fig. 3.23. Hybrid LVRT mechanical simulation results under asymmetrical (blue) and symmetrical (black) voltage dip to 0.1 pu

In terms of mechanical performance, the hybrid method first reduces the average stator power and the EM torque to half its rated value, and then to zero. By splitting the reduction of the EM torque to zero over two intervals, the change in EM torque is not as immediate, which reduces the mechanical transients on the drivetrain. From the shaft torque, T_s, in Fig. 3.23(b), the minimum shaft torque using the hybrid LVRT method is −0.395 pu and −0.396 pu for symmetrical and one-phase faults, respectively. Which is significantly lower than the SEIRI method, where the minimum shaft torque of −0.619 pu and −0.612 pu for symmetrical and one-phase fault, respectively. Since the initial shaft torque reduction contributes the most towards the shaft stress, this means that the hybrid method has reduced the mechanical stress on the shaft.

Over the durations of the LVRT and the active power ramping period, surplus power is being stored as rotation energy in the rotor's speed. During the entire

process, the rotor speed ω_g increases by 6.5% and the turbine speed ω_t increases by 6.0% in Figs. 3.23(d)-(e), respectively. The reason the increase in the rotor and turbine speeds are smaller for the hybrid case than the SEIRI method is because the DCC dissipates some of the surplus energy during the hybrid interval, so less electrical power is being converted to rotational energy.

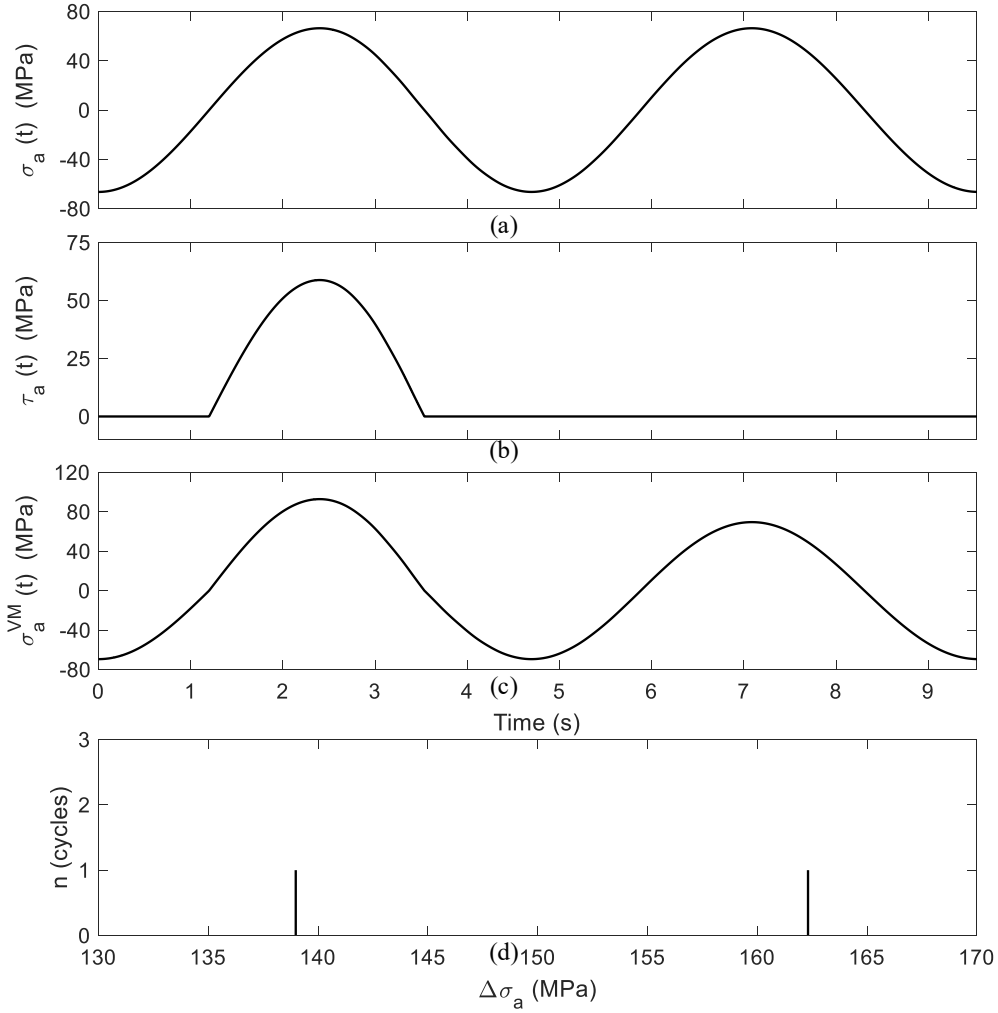

Fig. 3.24. The alternating bending stress, the alternating torque stress, the maximum von Mises stress, and the resultant rainflow count histogram using hybrid method.

Again, for the hybrid case, the shaft torques are nearly identical under both symmetrical and asymmetrical voltage dips to 0.1pu, so the stress-life analysis will only be performed for the symmetrical voltage dip case. Once more, the estimation that the minimum shaft torque will be applied as one stress half-cycle at the shaft's

rotational speed is used. The maximum alternating torsional stress was found to be 58.8 MPa, and the resultant alternating von Mises's stress has a maximum value of 92.8 MPa as portrayed in Fig. 3.24(c). RFC yields one stress cycle with a stress range of 139 MPa and another stress cycle with a stress range of 162 MPa. Applying Palmgren-Miner's rule yields an accumulated damage of 8.36×10^{-6}% equating to a shaft-life reduction of 34.6 s over two shaft rotations.

3.5 Summary

The control and comparison of the DCC, the SEIRI, and the hybrid PMSG LVRT methods are investigated in Chapter 3. From the simulation results, the DCC provides the best electrical performance without DC-link overvoltage. And, because the DCC does not impact the mechanical system, the DCC also has the best mechanical performance among the three methods. From the SEIRI LVRT simulation, the response time of the stator current is much slower than that of the grid current. This causes transient charging of the DC-link and may lead to overvoltage. In addition, the SEIRI method has poor mechanical performance because the EM torque is reduced to maintain the DC-link, which causes mechanical transient in the drivetrain system. The hybrid simulation shows how a small DCC can improve the DC-link overvoltage by absorbing some of the transient power caused by the SEIRI method. In addition, the mechanical transient on the shaft can be reduced by softening the EM torque reduction using the hybrid method.

Chapter 4

DFIG LVRT Methods Comparison

4.1 Introduction

For the DFIG WTs, most of the power is transferred through the stator winding, while only approximately 30% of the rated power is being transferred through the rotor winding. Therefore, only a partially rated WECS is needed to interface the rotor winding to the grid. The most common DFIG WECS topology is the BTB two-level VSC because of its low power requirements. Since the stator winding is connected to the grid, when a grid voltage dip occurs, the stator voltage dips alongside the grid voltage, which induces severe stator and rotor overcurrents. Because the rotor winding is connected to the WECS, the large rotor fault currents can damage the RSC and cause DC-link overvoltage for VSC-based WECS. The DCC is typically used to protect the DC-link from overvoltage, but it is incapable of protecting the RSC from severe rotor fault currents. One way to reduce the rotor fault current is by weakening the machine's flux through control. But conventionally, an RCB is installed on the rotor winding to redirect the rotor fault current away from the RSC. More recently, it has been suggested that the SRCB may be suitable to reduce rotor fault current by adding additional damping, while having the RSC remain connected to the rotor winding.

This chapter will overview the DFIG modelling and its under normal operations control. Then, the LVRT controls of the DCC with flux weakening, the RCB, and the SRCB are presented. Afterwards, each DFIG method will be simulated on MATLAB/Simulink using the simulation parameter given in Table 4.1. Again, the electrical and mechanical performance of each LVRT method will be evaluated under symmetrical and asymmetrical voltage dips to 0.1 pu.

4.2 DFIG modelling and normal operation control

For the DFIG, the rotating magnetic field is generated in the air gap, when the stator and rotor windings of the DFIG are connected to three-phase supplies, and the rotor speed can be controlled through the WECS that is attached to the rotor winding [36]. The stator dynamic of the DFIG is given in the *dq*-frame using stator voltage-oriented control (SVOC) as

$$v_{sd} = R_s i_{sd} + \frac{d}{dt}\lambda_{sd} - \omega_s \lambda_{sq}$$

Equation Chapter (Next) Section 1 (4.1)

$$v_{sq} = R_s i_{sq} + \frac{d}{dt}\lambda_{sq} + \omega_s \lambda_{sd} \tag{4.2}$$

where v_{sd} and v_{sq} are the *dq*-axis stator voltages, i_{sd} and i_{sq} are the *dq*-axis stator currents, R_s is the stator winding resistance, ω_s is the stator frequency. λ_{sd} and λ_{sq} are the *dq*-axis stator flux linkages given by

$$\lambda_{sd} = L_s i_{sd} + L_m i_{rd} \tag{4.3}$$

$$\lambda_{sq} = L_s i_{sq} + L_m i_{rq} \tag{4.4}$$

$$L_s = L_{ls} + L_m \tag{4.5}$$

where L_{ls} is the stator leakage inductance, and L_m is the magnetizing inductance. The rotor-side dynamics in the *dq*-frame are given by

$$v_{rd} = R_r i_{rd} + \frac{d}{dt}\lambda_{rd} - \omega_{sl} \lambda_{rq} \tag{4.6}$$

$$v_{rq} = R_r i_{rq} + \frac{d}{dt}\lambda_{rq} + \omega_{sl} \lambda_{rd} \tag{4.7}$$

$$\omega_{sl} = \omega_s - \omega_r \tag{4.8}$$

where v_{rd} and v_{rq} are the dq-axis rotor voltages, i_{rd} and i_{rq} are the dq-axis rotor currents, R_r is the rotor winding resistance, ω_{sl} is the slip speed. λ_{rd} and λ_{rq} are the dq-axis rotor flux linkages given by

$$\lambda_{rd} = L_r i_{rd} + L_m i_{sd} \tag{4.9}$$

$$\lambda_{rq} = L_r i_{rq} + L_m i_{sq} \tag{4.10}$$

$$L_r = L_{lr} + L_m \tag{4.11}$$

where L_{lr} is the rotor leakage inductance. Because the stator and rotor flux are dependent on both the rotor- and stator-side currents, the rotor- and stator-side dynamics are coupled. Typically, the RSC is directly connected to the rotor winding without an additional filter because the rotor leakage inductance and winding resistance operates as a low-pass filter. Therefore, the rotor-side dynamics can be used to control the RSC. The EM torque can be presented in terms of the stator flux and stator current by

$$T_e = \frac{3}{2} P(i_{sq}\lambda_{sd} - i_{sd}\lambda_{sq}) \tag{4.12}$$

On the grid side, the GSC is connected to the grid through an RL filter to smooth the GSC's modulated output to meet the grid's total harmonic distortion (THD) requirement. The GSC terminal dynamics of the DFIG is identical to the PMSG and is also expressed in the dq-frame using voltage-oriented control (VOC) given in (3.5) and (3.6).

4.2.1 RSC and GSC control

To control the RSC, FCS-MPC will be used on the rotor-side dynamics given in (4.6) and (4.7) because it has a faster control response time and the controller is more intuitive to design. First, solving for the dq-axis stator current time derivatives from (4.1) and (4.2), then substituting that into rotor-side dynamics in (4.6) and (4.7), and finally solving for the dq-axis stator current time derivatives yields

$$\frac{d}{dt}i_{rd} = -\frac{R_r i_{rd}}{\bar{L}} + \frac{v_{rd} + \omega_{sl}\lambda_{rq}}{\bar{L}} - \frac{L_m(v_{sd} - R_s i_{sd} + \omega_s \lambda_{sq})}{L_s \bar{L}} \tag{4.13}$$

$$\frac{d}{dt}i_{rq} = -\frac{R_r i_{rq}}{\bar{L}} + \frac{v_{rq} - \omega_{sl}\lambda_{rd}}{\bar{L}} - \frac{L_m(v_{sq} - R_s i_{sq} - \omega_s \lambda_{sd})}{L_s \bar{L}} \tag{4.14}$$

$$\bar{L} = L_r - \frac{L_m^2}{L_s} \tag{4.15}$$

Applying forward Euler's method to (4.13) and (4.14) and solving for the k+1th instance of i_{rd} and i_{rq} yield

$$\begin{aligned} i_{rd}[k+1] = &\left(1 - \frac{R_r T_{sm}}{\bar{L}}\right) i_{rd}[k] + \frac{T_{sm}}{\bar{L}}\left(v_{rd}[k] + \omega_{sl}\lambda_{rq}[k]\right) \\ &- \frac{T_{sm} L_m}{L_s \bar{L}}\left(v_{sd}[k] - R_s i_{sd}[k] + \omega_s \lambda_{sq}[k]\right) \end{aligned} \tag{4.16}$$

$$\begin{aligned} i_{rq}[k+1] = &\left(1 - \frac{R_r T_{sm}}{\bar{L}}\right) i_{rq}[k] + \frac{T_{sm}}{\bar{L}}\left(v_{rq}[k] - \omega_{sl}\lambda_{rd}[k]\right) \\ &- \frac{T_{sm} L_m}{L_s \bar{L}}\left(v_{sq}[k] - R_s i_{sq}[k] - \omega_s \lambda_{sd}[k]\right) \end{aligned} \tag{4.17}$$

For the two-level VSC, there are six active voltage vectors and two zero voltage vectors. Because the rotor-winding is connected to the RSC, this means there are eight outcomes for both $v_r[k]$ and $i_r[k+1]$. The control law is a cost function that selects the switching state that minimizes the error between the actual rotor current and its reference value.

$$g_r = (i_{rd}[k+1] - i_{rd}^*)^2 + (i_{rq}[k+1] - i_{rq}^*)^2 \tag{4.18}$$

Where i_{rd}^* and i_{rq}^* are the rotor current reference values.

B. Grid-side converter control

For consistency, the control GSC of the DFIG will also utilize FCS-MPC. Since

the GSC terminal dynamic equation of the DFIG is identical to that of the PMSG, the FCS-MPC of the GSC implemented for the PMSG can be used for the DFIG.

4.2.2 Outer control loops under normal operations

A. Rotor-side converter MPPT

During normal operation, the goal of the RSC is identical to that MSC of the PMSG, which is to achieve MPPT by maintain the OTSR through controlling the generator speed. The method to design the generator speed controller for the DFIG follows the same procedure as the PMSG. The generator speed controller is shown in Fig. 3.6, and the PI controller parameter is calculated through (3.42). The rotor speed controller outputs an EM torque reference, which can be used to determine the *d*-axis rotor current references for current control. Using the stator and rotor flux linkages relationships, the EM torque of the DFIG that is given in (4.12) can be rewritten as

$$T_e = \frac{3PL_m}{2L_s}(-i_{rq}\lambda_{sd} + i_{rd}\lambda_{sq}) \tag{4.19}$$

Under the assumption that the *dq*-frame stator flux-linkage time derivatives are zero in (4.1) and (4.2) and that the stator resistance is negligible, then the *dq*-frame stator flux-linkage are

$$\lambda_{sd} \approx \frac{v_{sq}}{\omega_s} \tag{4.20}$$

$$\lambda_{sq} \approx -\frac{v_{sd}}{\omega_s} \tag{4.21}$$

Under stator voltage-oriented control (SVOC), the stator *q*-axis voltage is v_{sq}=0, so $\lambda_{sd} \approx 0$. Now, substituting (4.20) and (4.21) into (4.19) and rearranging for the *d*-axis rotor current yields

$$i_{rd} = -\frac{2\omega_s L_s}{3PL_m v_{sd}} T_e \tag{4.22}$$

From (4.22), the *d*-axis rotor current reference can be obtained from the EM torque reference that has been outputted from the generator speed control.

For the *q*-axis rotor current reference, the stator reactive power Q_s is used, which is given by

$$Q_s = \frac{3}{2}(-v_{sd} i_{sq} + v_{sq} i_{sd}) \tag{4.23}$$

Again, the stator *q*-axis voltage v_{sq}=0. Then, substituting (4.4) into (4.23) for the *q*-axis stator current, and solving for the *q*-axis rotor current yields

$$i_{rq} = \frac{2L_s}{3v_{sd} L_m} Q_s + \frac{1}{L_m} \lambda_{sq} \tag{4.24}$$

Now substituting (4.21) for the *q*-axis stator flux-linkage gives

$$i_{rq} = \frac{2L_s}{3v_{sd} L_m} Q_s - \frac{v_{sd}}{\omega_s L_m} \tag{4.25}$$

From (4.25), the *q*-axis rotor current can be obtained from the stator reactive power reference, which is normally set to zero because the grid reactive power is zero under normal operations

B. Grid-side converter DC-link voltage control

The GSC is used to control the DC-link voltage for the DFIG. For the DFIG the DC-link voltage dynamic is given by

$$\frac{1}{2} C_{dc} \frac{d}{dt} V_{dc}^{\ 2} = -P_r - P_{gr} \tag{4.26}$$

where P_r is the rotor power that is directed towards the rotor winding and P_{gr} is the grid power contributed from the rotor winding. Since, the DC-link dynamic is like the PMSG, the same DC-link controller design procedure can be used with some minor adjustments. For the DFIG, the DC-link controller is shown in Fig. 4.1.

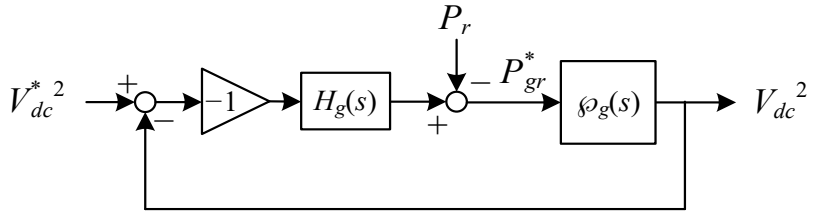

Fig. 4.1. DFIG GSC DC-link voltage control loop.

The overall DC-link voltage plant model is

$$\wp_g(s) = \frac{\tilde{V}_{dc}^{\,2}}{\tilde{P}_{gr}^{*}} = -\frac{2(\tau_g s + 1)}{Cs(\tau_i s + 1)} \tag{4.27}$$

$$\tau_g = \frac{2L_g P_{gr0}}{3V_{gd}^2} \tag{4.28}$$

Then, the lead compensator can be designed using (3.65) – (3.67).

4.3 Review of DFIG LVRT control strategies

For VSC-based DFIG, the objective of LVRT is to protect the RSC devices from overcurrent and the DC-link capacitor from overvoltage. In this thesis, the DCC will be used to protect the DC-link by switching in a resistor in parallel with the DC-link to dissipate the excess power. The LVRT methods to prevent overcurrent that are used in this thesis are the machine flux-weakening method, the RCB, and the SRCB. The machine flux-weakening method is a control-based method that reduces the rotor-side current references. Whereas the RCB is the most common hardware-based LVRT method, which redirects the large fault current away from the RSC and dissipates it with a crowbar circuit. Finally, the SRCB is a more recently proposed hardware-based LVRT method that adds additional

damping to the rotor winding when turned on and reduces rotor fault current.

4.3.1 DC-link chopper and flux weakening LVRT Method

The DFIG WECS with the DCC can be modelled with the same equivalent circuit given in Fig. 3.8 and the electrical dynamics of the equivalent circuit is given in (3.68). However, for the DFIG, the power difference is $\Delta P = -P_r - P_{gr}$. The DCC plant model is still given by (3.69), so the DFIG DCC DC-link control loop is as illustrated in Fig. 4.2. The DCC controller can be designed using (3.70) to achieve unity gain at the control bandwidth of $1/\tau_i$. The machine flux weakening is achieved by suspending the MPPT operation of the RSC and setting the rotor current references to zero.

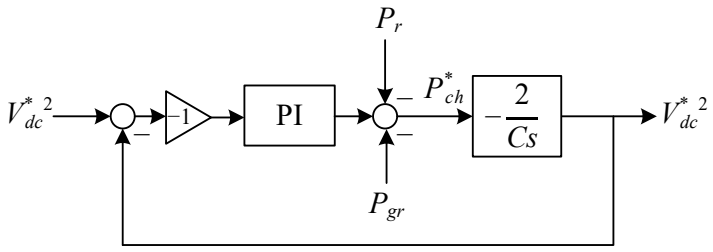

Fig. 4.2. The DFIG DCC LVRT DC-link voltage control loop.

4.3.2 Rotor Crowbar LVRT Method

The RCB is used to prevent large overcurrent from entering the RSC during LVRT, and the RCB resistor is usually chosen to be 20 to 50 times the rotor winding resistance [16]. The activation of the RCB is determined by checking whether the rotor current is above a threshold value. When the fault current is above the threshold value, the RCB is turned on, and the RSC is disabled by removing the gating signal. When the rotor current is below the threshold value, the RCB is turned off, and the RSC is re-enabled. This can be implemented by

$$g_{RCB} = \begin{cases} 1 & I_r \geq I_r^{max} \\ 0 & I_r < I_r^{max} \end{cases} \tag{4.29}$$

Meanwhile, the activation of the DCC has the same controller as the controller

described in Fig. 4.2. However, the feedforward of the rotor power is multiplied by the inverse of the switching state of the RCB, which coordinates the RCB with DCC because when the RCB is activated, the rotor power will be diverted away from the RSC.

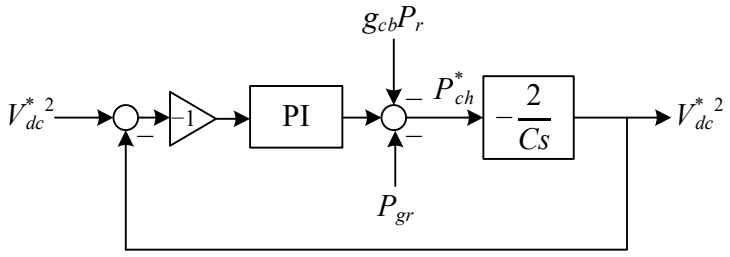

Fig. 4.3. RCB coordinated DCC LVRT DC-link voltage control loop.

4.3.3 Series Rotor Crowbar LVRT Method

The SRCB control is implemented by adjusting the FCS-MPC of the RSC in (4.16) and (4.17). When the SRCB is closed, the dynamic model of the rotor winding is unchanged; however, once the SRCB is opened, the rotor winding resistance will be increased by the SRCB resistance. From this, the FCS-MPC can be modified as

$$\begin{aligned} i_{rd}[k+1] = &\left(1-\frac{\left(R_r+\bar{S}_{SCB}R_{SCB}\right)T_{sm}}{\bar{L}}\right)i_{rd}[k]+\frac{T_{sm}}{\bar{L}}\left(v_{rd}[k]+\omega_{sl}\lambda_{rq}[k]\right) \\ &-\frac{T_{sm}L_m}{L_s\bar{L}}\left(v_{sd}[k]-R_s i_{sd}[k]+\omega_s\lambda_{sq}[k]\right) \end{aligned} \tag{4.30}$$

$$\begin{aligned} i_{rq}[k+1] = &\left(1-\frac{\left(R_r+\bar{S}_{SCB}R_{SCB}\right)T_{sm}}{\bar{L}}\right)i_{rq}[k]+\frac{T_{sm}}{\bar{L}}\left(v_{rq}[k]-\omega_{sl}\lambda_{rd}[k]\right) \\ &-\frac{T_{sm}L_m}{L_s\bar{L}}\left(v_{sq}[k]-R_s i_{sq}[k]-\omega_s\lambda_{sd}[k]\right) \end{aligned} \tag{4.31}$$

where S_{SCB} is the switching state of the SRCB and R_{SCB} is SRCB resistance. Using a two-level VSC, the original eight switching states are considered with the SRCB closed (S_{SCB}=1). Then, two additional switching state are considered in the modified MPC, which opens the SRCB (S_{SCB}=0) and shorts the RSC by either opening all the top switches while closing all the bottom switches or the vice versa.

Table 4.1 DFIG Simulation Parameters

Variable	Description	Value
	Wind Turbine Parameters	
P_w	Rated Wind Power [MW]	2.45
r	Turbine Blade Length [m]	57.5
ρ	Air Density [kgm^2]	1.225
$C_{p,opt}$	Optimal Rotor Efficiency	0.48
λ_{opt}	Optimal Tip Speed Ratio	8.1
n_g	Rated Turbine Speed [rpm]	12.5
v_w	Rated Wind Speed[m/s]	9.29
	Drive Train Parameters	
J_t	Wind Turbine Inertia [kgm^2]	1.235×10^7
J_g	PMSG Inertia [kgm^2]	147.6
K_s	Shaft Stiffness [Nm/rad]	6.671×10^8
D_s	Shaft Mutual Damping [Nm/(rad/s)]	3.389×10^6
N_{gb}	Gear Box Ratio	115
	PMSG Parameters	
P_s	Rated Generator Power [MW]	2.45
f_s	Rated Stator Frequency [Hz]	60
n_g	Rated Generator Speed [rpm]	1440
P	Pole Pairs	3
R_s	Stator Winding Resistance [mΩ]	4.470
R_r	Rotor Winding Resistance [mΩ]	3.109
L_s	Stator Self-Inductance [mH]	1.588
L_r	Rotor Self-Inductance [mH]	1.577
	Grid Parameters	
S_g	Rated Apparent Grid Power [MVA]	2.45
V_g	Rated Grid Voltage [V]	690
I_g	Rated Grid Current [A]	2050
f_{gr}	Grid Frequency [Hz]	60
L_g	Inverter Filter Inductance [mH]	0.945
R_g	Inverter Resistance [mΩ]	2.5
	WECS Parameters	
V_{dc}	DC-link Voltage [V]	1380
C_{dc}	DC-link Capacitance [mF]	10
f_{sw}	Switching frequency [Hz]	3420

4.4 Evaluation of DFIG LVRT strategies under symmetrical and asymmetrical faults

The electromechanical performance of the DCC with the machine flux weakening, the RCB, and the SRCB LVRT methods will be simulated on MATLAB/Simulink. For the DFIG, symmetrical and one-phase asymmetrical voltage dips are tested. The grid voltage dip is simulated by reducing the grid voltage to 0.1 pu for 150 ms. For a severe grid dip to 0.1 pu, the E.ON grid specifies that the grid current references of the GSC should be set to i_{gd}=0 pu and i_{gq}=−1 pu. Once the fault is cleared, an active ramp rate of 0.9 pu/s will be applied on the grid active power.

Once again, the 5 MW shaft parameter will be used to estimate the bending stress for a 2.45 MW WT. The bending stress at the top and bottom of the shaft at main bearings is 66.4 MPa, and the midrange torsional stress at the outer shell of the shaft is 42.1 MPa. The parameters of the modified SN curve are N_e=1.02×10^6 cycles, $\Delta\sigma_e^*$=202.59 MPa, and m_1=6.389, and the SN curve in the log scale can be seen in Fig. 3.12.

4.4.1 Simulation results analysis of the DCC with flux weakening LVRT method

For the DFIG, because the stator winding is directly connected to the grid, the stator voltage drops alongside with grid voltage dips. Based on the dynamic equations of the stator winding given by (4.1) and (4.2), the stator flux will experience a transient response caused by the stator voltage dropping, which results in severe fault currents in both the stator and rotor winding from the relationship between the winding currents and stator flux as described in (4.3) and (4.4).

The machine flux weakening LVRT method reduces the rotor overcurrent by setting the *dq*-frame rotor current references to zero when a voltage dip occurs. From the simulation parameters, the per unit values of the stator and rotor peak currents under normal conditions are 0.818 pu and 0.937 pu, respectively. The simulation results under a symmetrical voltage dip to 0.1 pu is shown in Fig. 4.4.

When the machine flux is weakened under symmetrical voltage dips, the stator and rotor peak currents increase to 2.68 pu and 2.82 pu, respectively. And under asymmetrical voltage dips, the stator and rotor peak currents increase to 2.06 pu and 2.17 pu, respectively. Because the rotor current may increase up by 200% of the rated rotor current, the RSC is still required to be over designed to prevent damaging the RSC devices. Symmetrical faults result in more severe fault currents because the impact on the stator voltage is more severe. For symmetrical faults, when the grid voltage drops to 0.1 pu, the *dq*-frame stator voltages, using VOC, are v_{sd}=0.1 pu and v_{sq}=0 pu. In contrast, when one-phase drops to 0.1 pu, the positive sequence *dq*-frame stator voltages are v_{sd}^{+}=0.7 pu and v_{sq}^{+}=0 pu, and the negative *dq*-frame stator voltages are v_{sd}^{-}=0.3 pu and v_{sq}^{-}=0 pu . Because the *d*-axis stator voltage does not reduce as much under asymmetrical voltage dips, the stator and rotor currents have weaker dynamic responses.

In addition, rotor power will also spike because of the large rotor fault current. Since the GSC is controlled to not output active power, this large rotor power will cause overvoltage of the DC-link capacitor, so a DCC is required. Unlike the design of the PMSG's DCC, the DCC resistance is not as intuitive to design because of the rotor power is undergoing severe transients. In this simulation, the chopper resistance is selected to be a tenth of the rated DC-link impedance, which is given by

$$R_{ch} = \frac{V_{dc}^{\ 2}}{10P_{r0}} \tag{4.32}$$

Even with the DCC in place, for symmetrical voltage dips, the DC-link voltage still raises up to V_{dc}=1.06 pu, while the maximum duty cycle of the DCC is D=0.775, as illustrated in Figs. 4.4(g)-(h). In contrast, because the rotor power is smaller for one-phase voltage dips, the DC-link increases to V_{dc}=1.05 pu, and the maximum DCC duty cycle is D=0.608, as depicted in Figs 4.5(g)-(h).

During the voltage dip to 0.1 pu, the rotor current is controlled to zero meaning the stator current should converge to zero as well. Therefore, the average stator

power and reactive power are both approximately zero, so the grid reactive power can only be supported by the GSC. However, the GSC only transfers approximately 16% of the rated power, so the reactive power support that the DFIG can provide is severely limited. For asymmetrical faults, there are also unpredictable power oscillations in the active and reactive grid powers when the asymmetrical grid voltage is combined with the stator current oscillations.

When the grid voltage is restored, the change in the stator voltage induces another transient response resulting in large stator and rotor overcurrents. Because the grid voltage is restored at this point, the large stator current along with the normal grid voltage causes the grid power to drastically spike to P_g=2.99 pu and P_g=2.4 pu for symmetrical faults and asymmetrical faults, respectively. In addition, the reactive grid power dips to Q_g=−1.82 pu and to Q_g=−1.25 pu for symmetrical faults and asymmetrical faults, respectively. To fulfill the active power ramp rate GCR, when the grid voltage dip is cleared, a rate limiter is applied to the rotor *d*-axis current to limit the rate of the generator's output, and the DCC is activated to prevent charging of the DC-link during the active power ramping.

The mechanical performance of the DFIG under DCC with flux weakening LVRT is shown in Fig. 4.6. Under normal conditions, the rated torque and generator speeds are 0.833 pu and 1.2 pu using the given turbine parameters. When the fault occurs, the rotor current references are set to zero to reduce the flux of the DFIG, which should reduce the EM torque to zero according to [10]. However, the rotor current cannot drop to zero instantly, which reflects in the EM torque, as seen in Fig. 4.6(a). For asymmetrical faults, the additional oscillations in the rotor and stator currents causes the EM torque to not drop as severely compared to the symmetrical case, which is reflected in the reduction in the shaft torque. The shaft torque drops to −0.314 pu under a symmetrical voltage dip but only to −0.089 pu for a one-phase voltage dip. The generator output power is reduced because of the reduction in the EM torque, which means some of the captured wind power is stored in the rotor's speed in the form of kinetic energy. This causes the generator speed to increase from 1.2 pu to 1.28 pu and 1.27 pu for symmetrical and one-phase voltage dips, respectively.

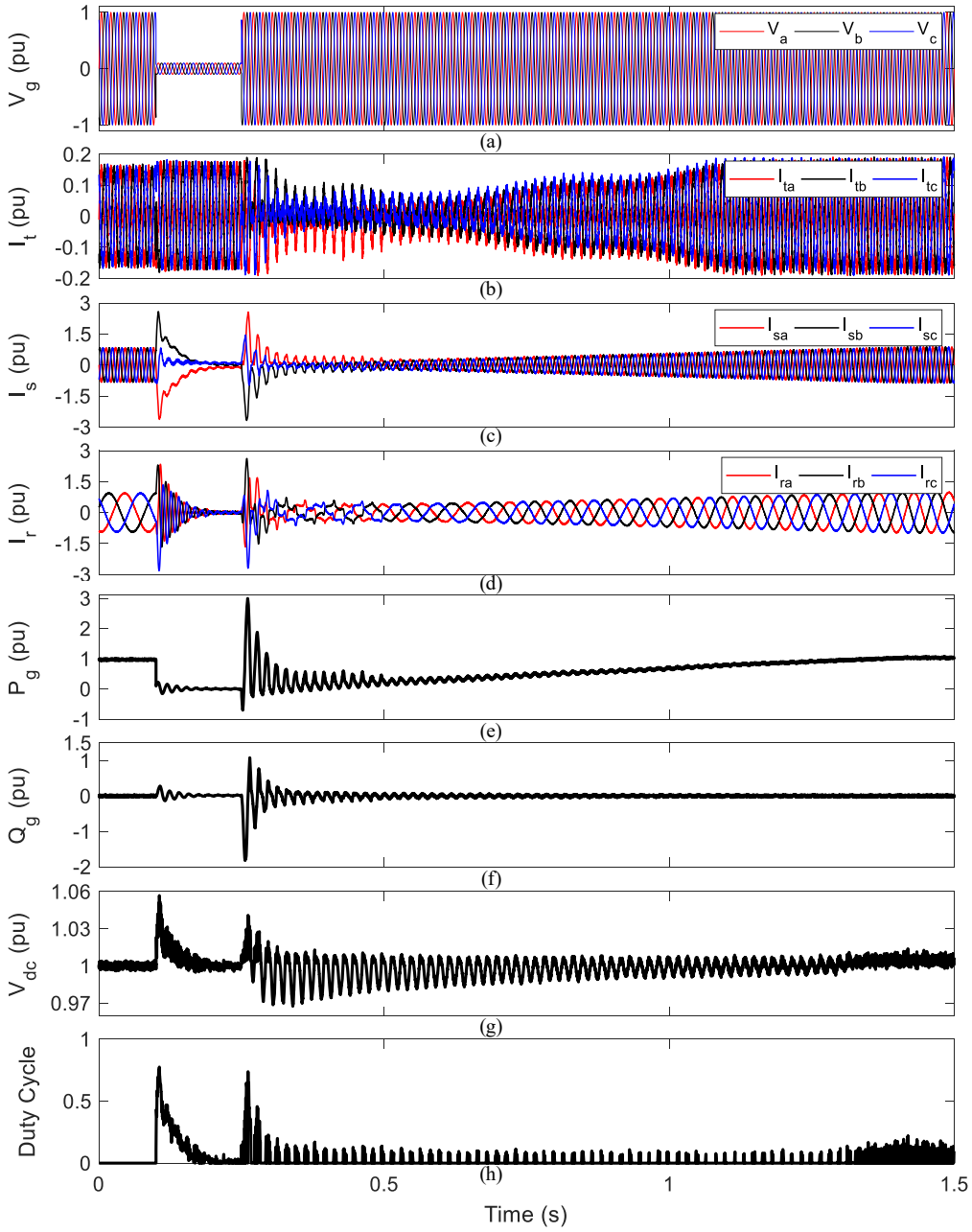

Fig. 4.4. DCC with the machine flux weakening LVRT electrical simulation results under symmetrical voltage dips to 0.1 pu.

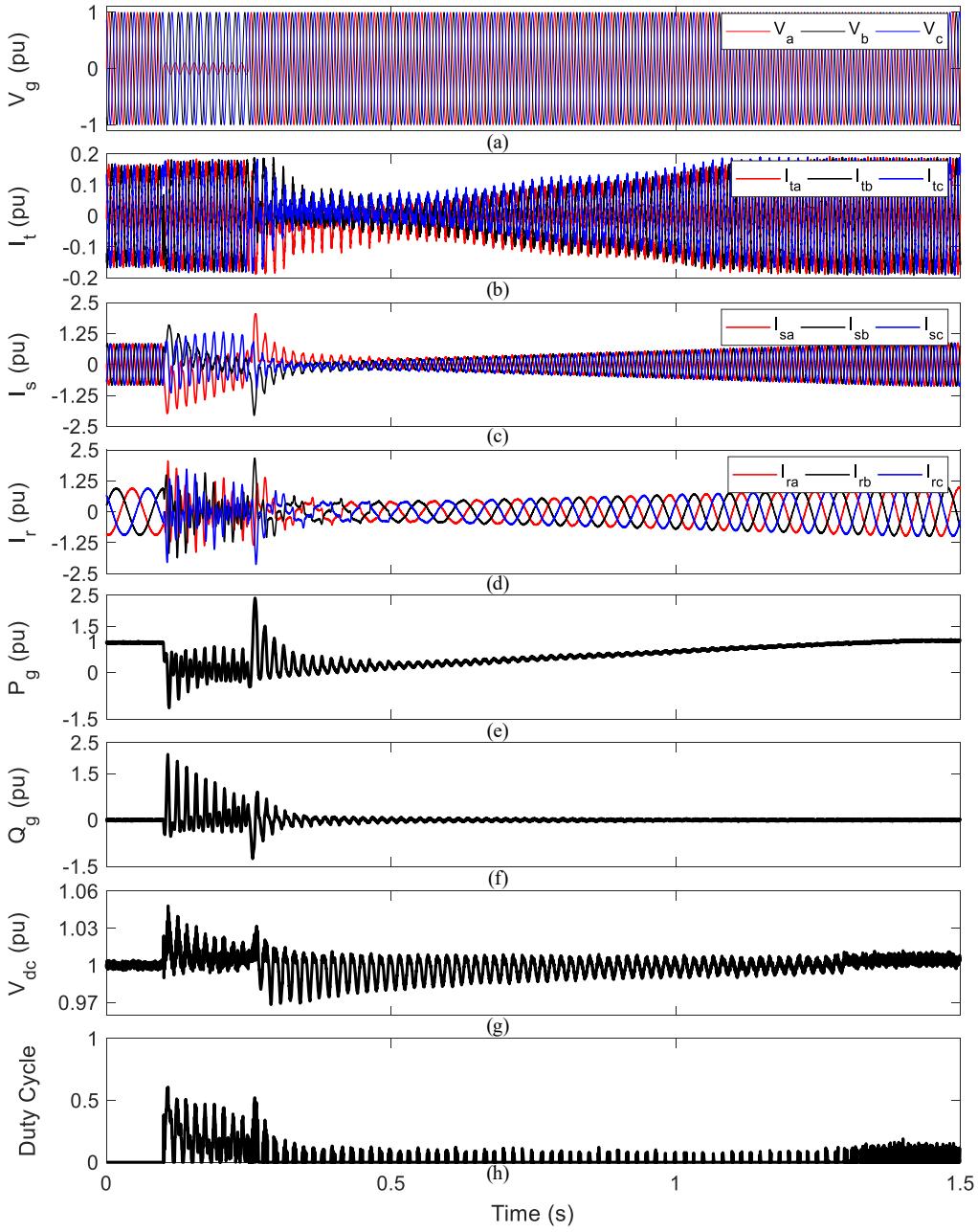

Fig. 4.5. DCC with the machine flux weakening LVRT electrical simulation results under asymmetrical voltage dips to 0.1 pu.

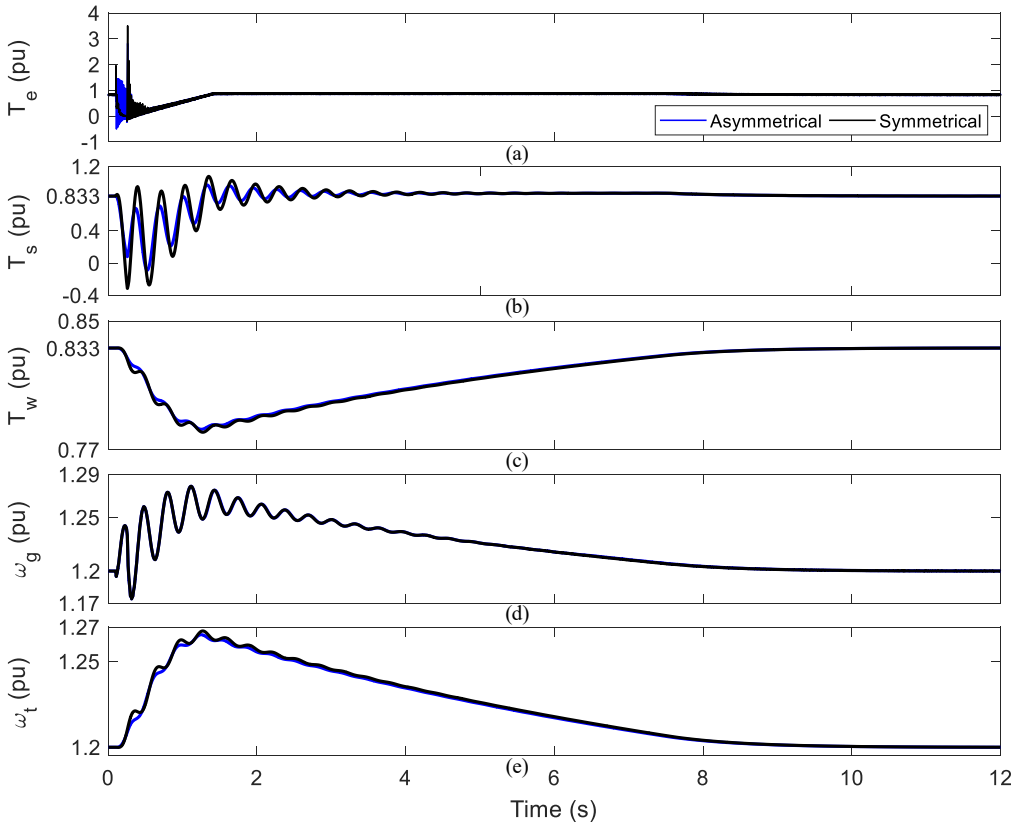

Fig. 4.6. DCC with the machine flux weakening LVRT mechanical simulation results under asymmetrical (blue) and symmetrical (black) voltage dips to 0.1 pu.

For the DCC DFIG LVRT method, the stress-life analysis is performed for both the symmetrical and the one-phase voltage dip case shown in Fig. 4.7 in (black) and (red), respectively. The minimum shaft torques resulting from the two types of voltage dips is applied as one stress half-cycle at the shaft's rotational speed, as seen in Fig. 4.7(b). Where, the maximum alternating torsional stress are 58.0 MPa and 46.6 MPa and the maximum von Mises's stress are 92.2 MPa and 84.9 MPa for symmetrical and one-phase voltage dips, respectively. Under symmetrical voltage dip conditions, RFC yields one stress cycle with a stress range of 139 MPa and another stress cycle with a stress range of 161.7 MPa. For one-phase voltage dips, the stress cycle counting yields one stress cycle with a stress range of 139 MPa and one stress cycle with a stress range of 154 MPa. For symmetrical voltage dips, applying Palmgren-Miner's rule yields an accumulated damage of 8.062×10^{-6}%, and the reduction of the shaft lifetime is 33.4 s. For one-phase voltage dips, the

accumulated damage is 5.144×10^{-6}% corresponding to a life reduction of 21.3 s.

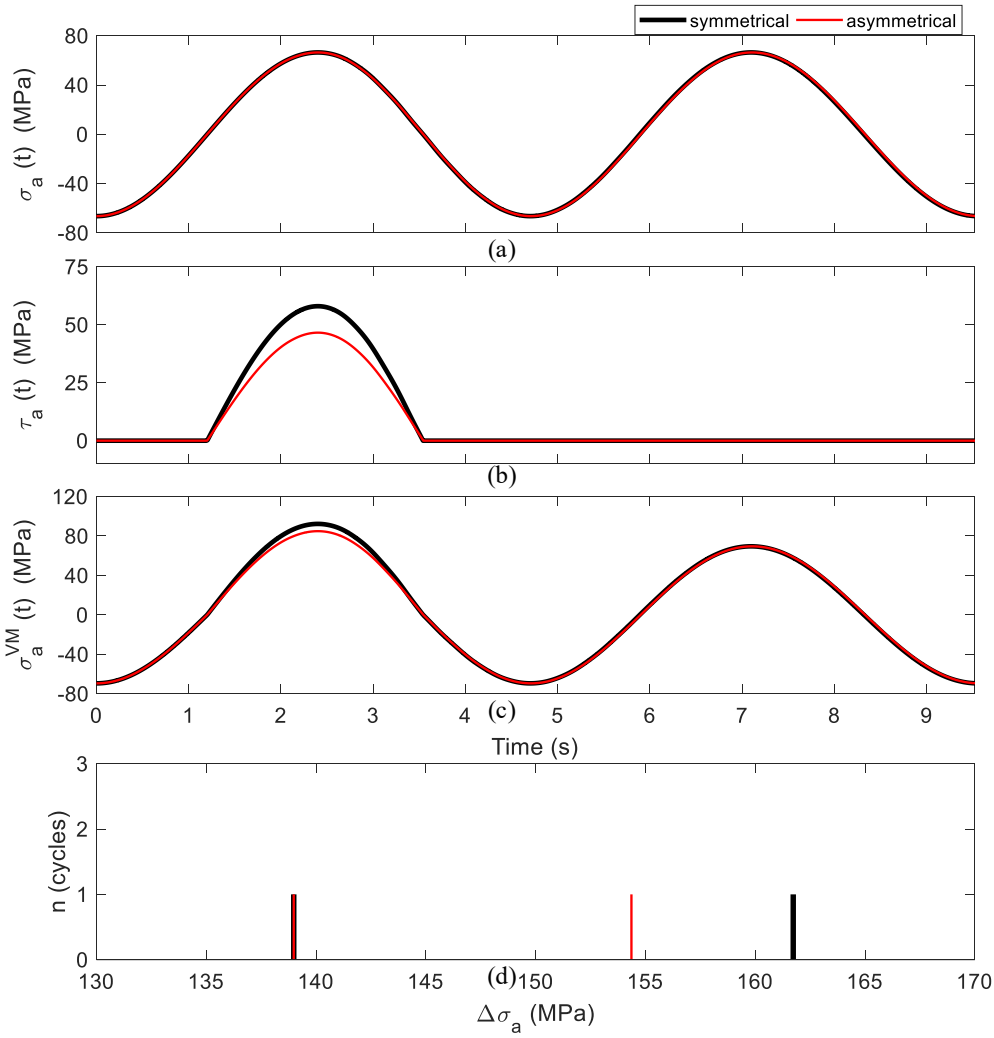

Fig. 4.7. The alternating bending stress, the alternating torque stress, the maximum von Mises stress, and the resultant rainflow count histogram using the DCC with machine flux weakening LVRT method.

4.4.2 Simulation results analysis of the RCB LVRT method

The RCB LVRT method redirects the rotor fault current by turning on the RCB and disabling the RSC when the peak rotor winding current is above a specified threshold value. In this simulation, the threshold value is set to 10% above the rated current. Like the flux weakening LVRT method, with the RCB LVRT method, the drop in the stator voltage causes large stator and rotor fault currents. From Figs. 4.8(c)-(d), the stator and rotor peak currents increase to 2.73 pu and 2.89 pu under symmetrical voltage dips to 0.1 pu, respectively. Under asymmetrical voltage dips,

the stator and rotor peak current increases to 2.06 pu and 2.17 pu, respectively, as seen in Figs. 4.9(c)-(d). Like the flux weakening method, the rotor current still increases substantially, but once the rotor current increases above 10% of the rated rotor current, the RCB turns on to prevent the large overcurrent from entering the RSC. In Fig. 4.8(e), under a symmetrical voltage dip, the maximum current entering the RSC is reduced from 2.89 pu to 1.23 pu. Whereas, under a one-phase voltage dip, the RCB reduces maximum RSC current from 2.17 pu to 1.03 pu. From this, the RSC still needs to be overdesigned by 31.3% to encompass the 1.23 pu overcurrent under symmetrical voltage dips.

A DCC is also used alongside the RCB method to prevent overvoltage of the DC-link voltage, and again the chopper resistance is selected to be a tenth of the rated DC-link impedance. With the DCC in place for symmetrical voltage dips, the maximum DC-link voltage is V_{dc}=1.03 pu, and the maximum duty cycle is D=0.4551 as illustrated in Figs. 4.8(h)-(i). Because the RCB redirects the large rotor fault currents, the power entering the RSC during the voltage dip is reduced resulting in less charging of the DC-link. This means RCB also provides better DC-link overvoltage protection and because the maximum duty cycle is reduced, a smaller DCC can be used.

The activation of the RCB converts the DFIG into a SCIG, so the rotor winding cannot be controlled to have the stator winding output reactive power. So, again only the GSC can provide reactive power compensation, which means the reactive power compensation of the DFIG is severely limited. And like the machine flux weakening LVRT method, there are unpredictable transient power oscillation in the grid's active and reactive power under asymmetrical voltage dips.

Another transient occurs on the stator current when the grid voltage is restored, which results in a large surge in the grid power to P_g=2.60 pu and P_g=2.17 pu for symmetrical faults and asymmetrical faults, respectively. In addition, the reactive power rapidly dips to Q_g=−1.95 pu and Q_g=−1.34 pu for symmetrical faults and asymmetrical faults, respectively.

Fig. 4.10 illustrates the mechanical performance using the RCB for both balanced and one-phase faults. The mechanical performance using the RCB is like

the machine flux weakening method because the stator and rotor currents have similar transient responses. Again, the reduction of the EM torque is not as rapid for asymmetrical voltage dips compared to symmetrical voltage dips. In Fig. 4.10(b), the shaft torque drops to −0.367 pu and −0.066 pu under symmetrical voltage dips and one-phase voltage dips, respectively. When compared to the standalone DCC method, the shaft experiences slightly more stress under symmetrical faults, and slightly less stress under one-phase faults. The excess power between the generator output and the captured wind power during the voltage dip and the active grid power ramping period accelerates the generator speed up to 1.28 pu and 1.27 pu for symmetrical and one-phase faults, respectively, as illustrated in Fig. 4.10(d).

For the RCB LVRT method, the lifetime analyses of the symmetrical and one-phase voltage dips are shown in Fig. 4.11 in black and red, respectively. For symmetrical and one-phase voltage dips, the maximum alternating torsional stress are 60.6 MPa and 45.4 MPa, respectively, and the resulting maximum von Mises's stress are 94.0 MPa and 84.2 MPa, respectively. Under symmetrical voltage dips, RFC yields one stress cycle with a stress range of 139 MPa and another stress cycle with a stress range of 164 MPa. For one-phase voltage dips, the stress cycle counting yields one stress cycle with a stress range of 139 MPa and one stress cycle with a stress range of 154 MPa. For symmetrical voltage dips, applying Palmgren-Miner's rule yields an accumulated damage of 9.047×10^{-6}%, and the reduction of the shaft's lifetime is 37.5 s. For one-phase voltage dips, the accumulated damage is 4.941×10^{-6}%, and the shaft's lifetime reduction is 20.5 s.

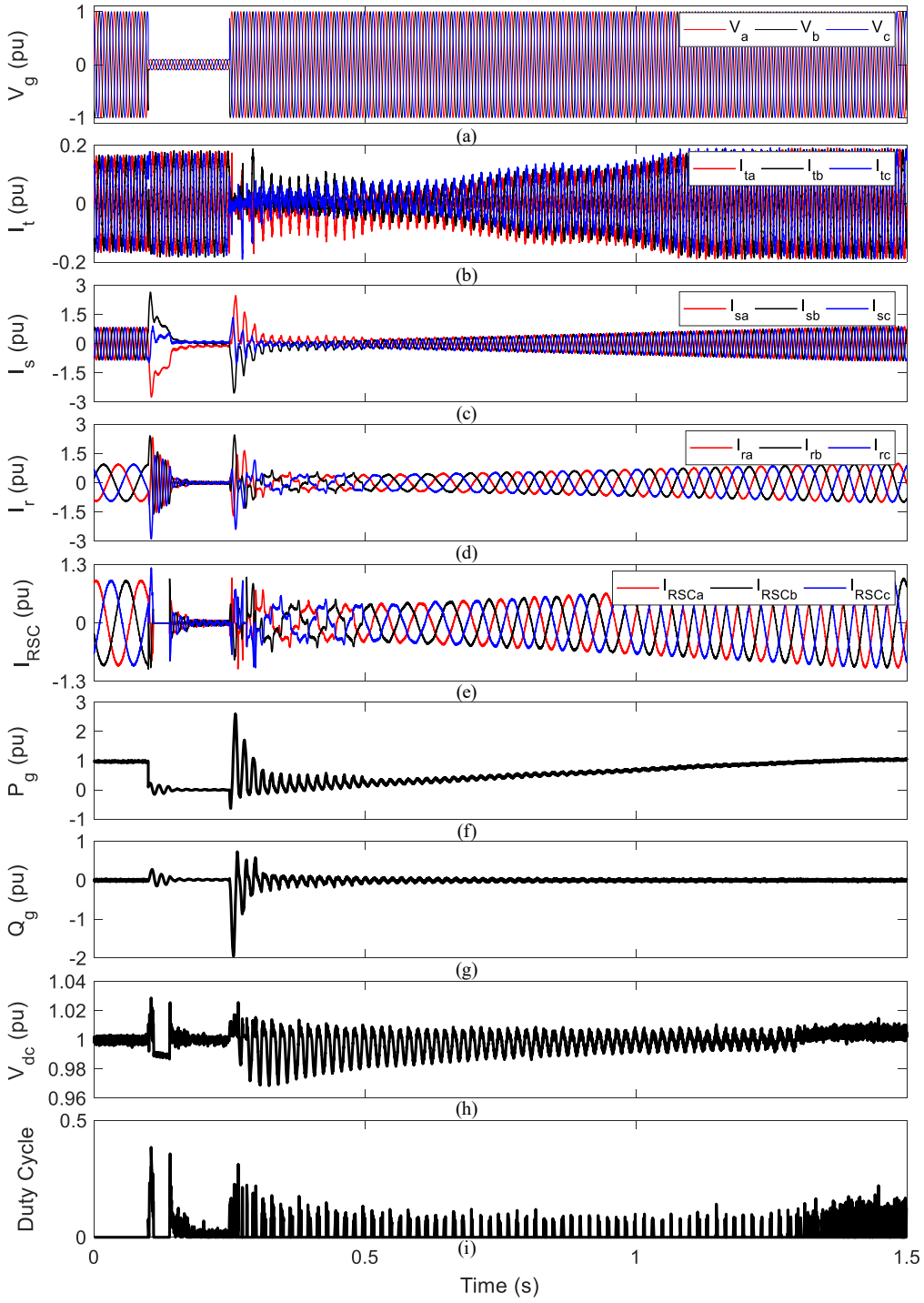

Fig. 4.8. The RCB LVRT electrical simulation results under symmetrical voltage dips to 0.1 pu.

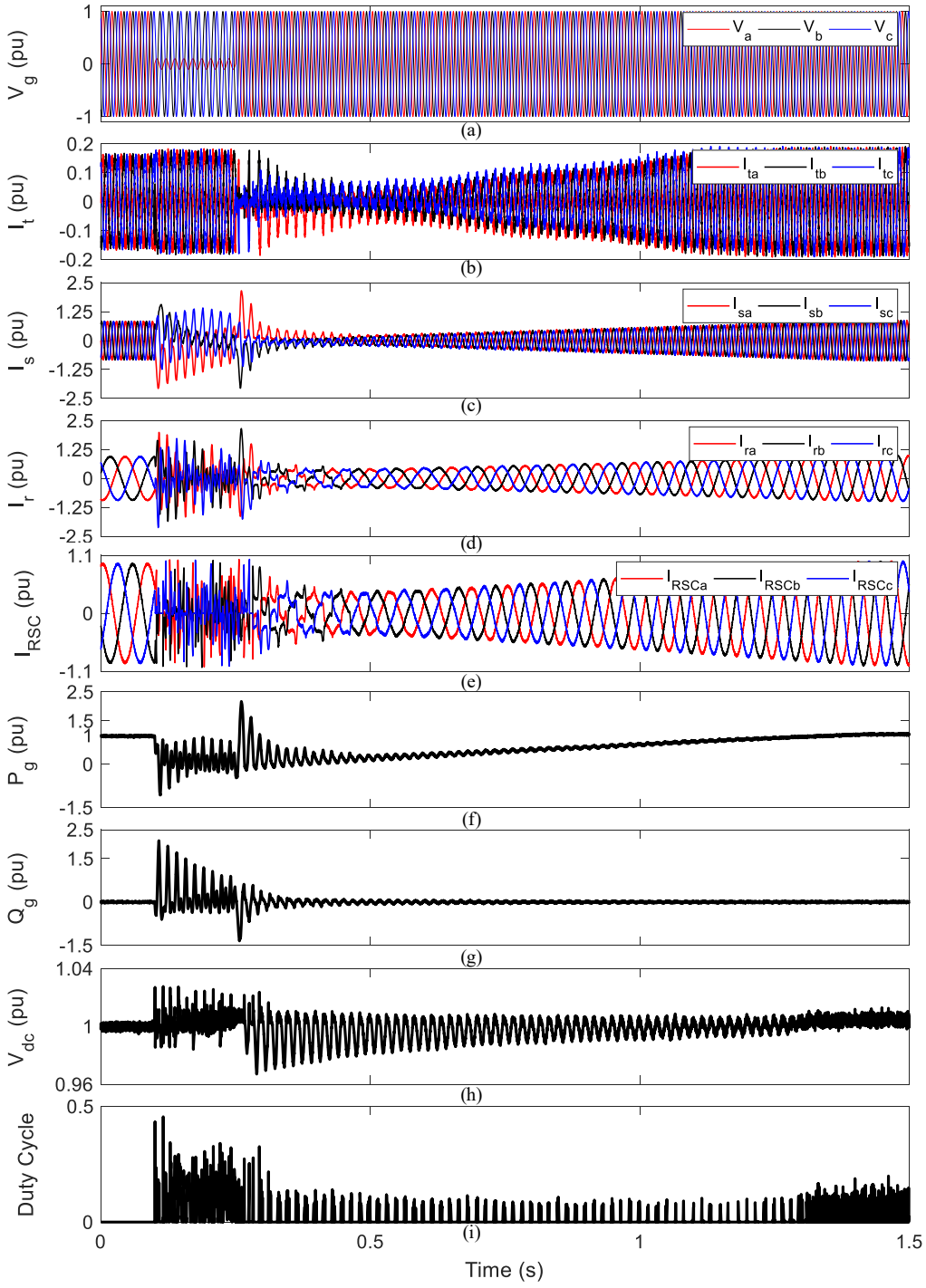

Fig. 4.9. The RCB LVRT electrical simulation results under asymmetrical voltage dips to 0.1 pu.

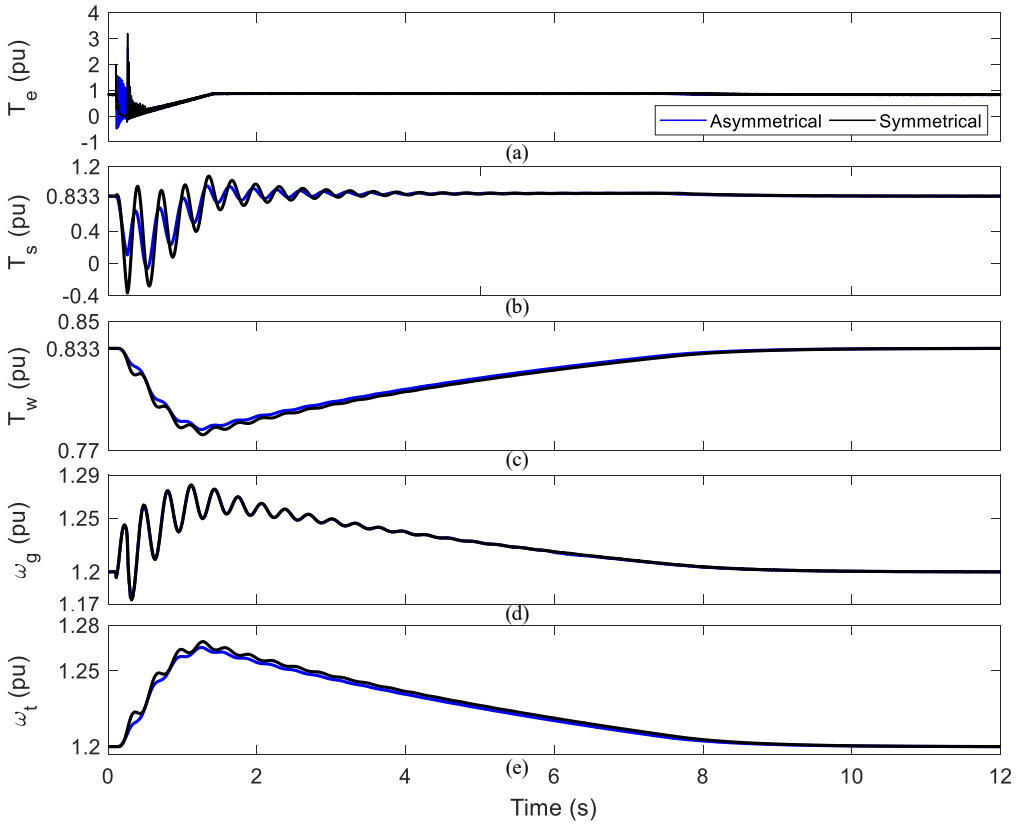

Fig. 4.10. The RCB LVRT mechanical simulation results under asymmetrical (blue) and symmetrical (black) voltage dips to 0.1 pu.

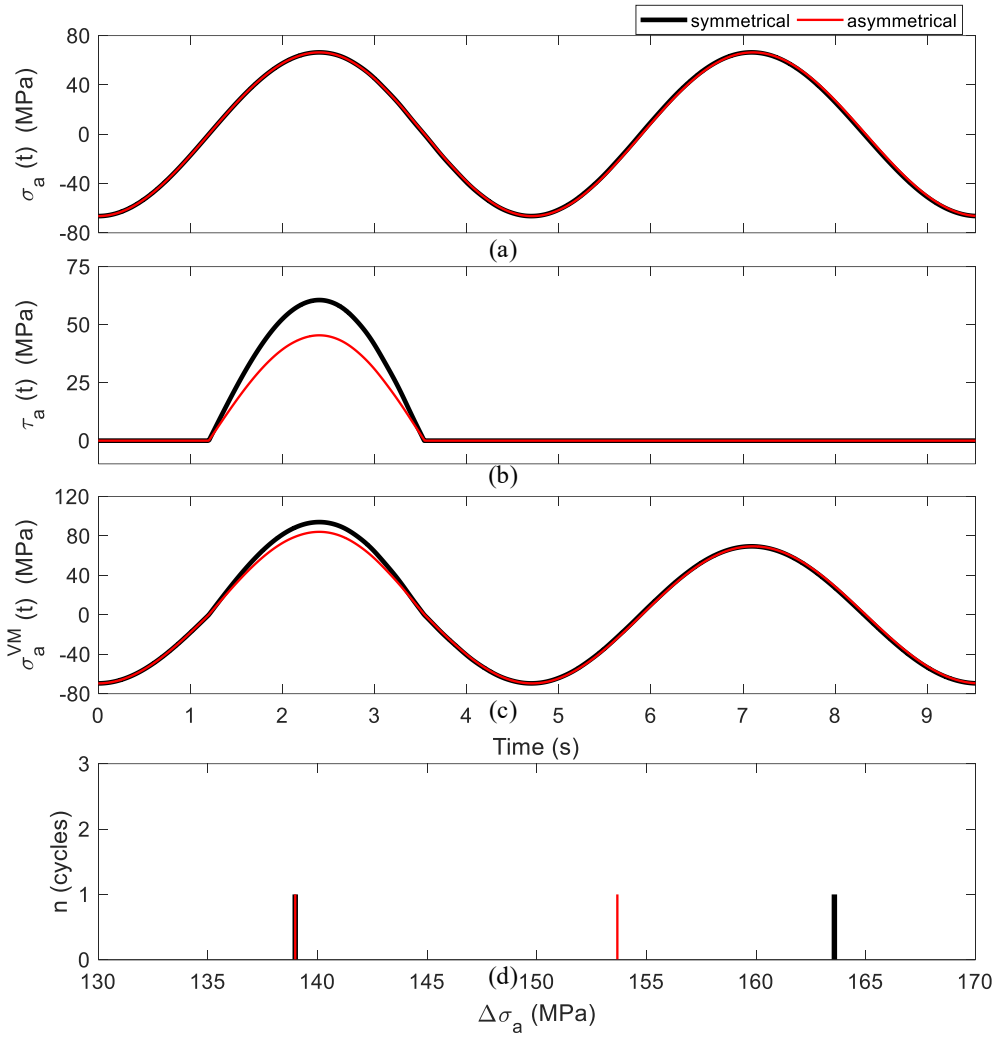

Fig. 4.11. The alternating bending stress, the alternating torque stress, the maximum von Mises stress, and the resultant rainflow count histogram using the RCB LVRT method.

4.4.3 Simulation results analysis of the SRCB LVRT method

Unlike the previous two methods, the stator and rotor currents do not experience severe transients during LVRT because of the damping provided by the additional series resistor. During LVRT, the rotor *dq*-frame current references are both set to zero to reduce the rotor overcurrent. Because the *dq*-frame rotor currents are larger than zero, the SRCB will be turned on and the RSC is shorted. In Fig. 4.12(c)-(d), the maximum stator and rotor peak currents are reduced to 0.366 pu and 0.244 pu during symmetrical and asymmetrical voltage dips, respectively. In Fig. 4.13(c)-(d), the maximum stator and rotor peak currents during one-phase

voltage dips are 0.448 pu and 0.265 pu, respectively.

Unlike the two prior LVRT methods, the one-phase fault currents are larger than the balanced fault currents because during balanced faults, the SRCB is opened for the entire duration because the *dq*-axis rotor currents are always larger than their reference value; however, for one-phase faults, the SRCB will occasionally close during rotor current zero crossings, which removes the additional series resistance and increases the rotor and stator current.

The SRCB also protects the DC-link voltage from overvoltage because the RSC is shorted preventing the rotor power from charging the DC-link. From Fig. 4.12(g), the DC-link is discharged to 0.974 pu because the RSC is immediately disabled cutting off the rotor power, but the *d*-axis grid-side current is unable reduce to zero instantly. Whereas, for asymmetrical faults, the occasional closing of the RSC results in slight charging of the DC-link, so the DC-link voltage does not dip as much.

Although the restoration of the stator voltage causes a second transient response, the SRCB is triggered to prevent the rotor from exceeding the *dq*-frame rotor current references. This also minimizes the stator current transient response, which in turn reduces the grid active power spike and the grid reactive power dip compared to the previous two methods. Since the DC-link voltage can be protect by the SRCB, the DCC is not necessary, but the DCC may assist with preventing DC-link overvoltage when the active power is ramping.

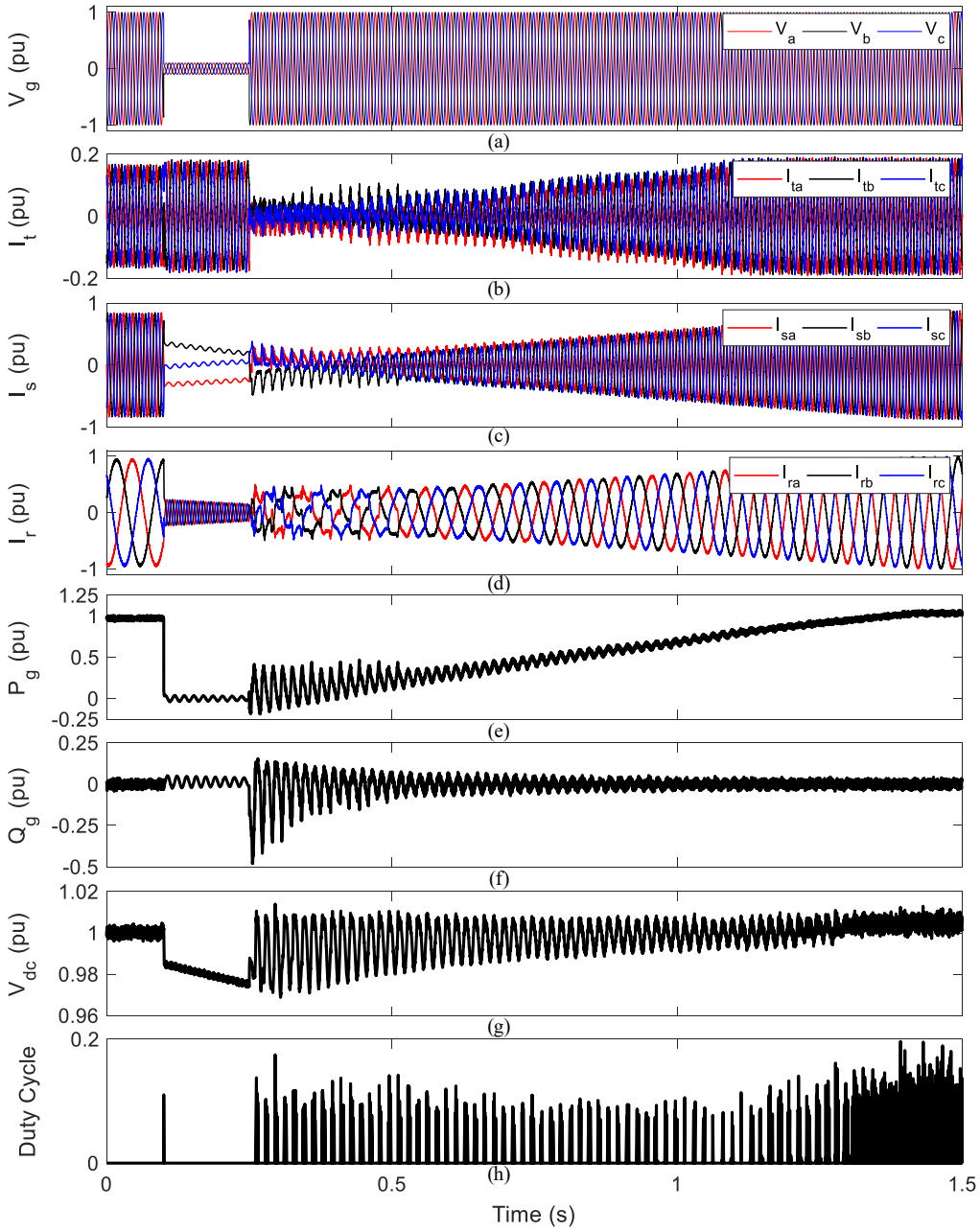

Fig. 4.12. The SRCB LVRT electrical simulation results under symmetrical voltage dips to 0.1 pu.

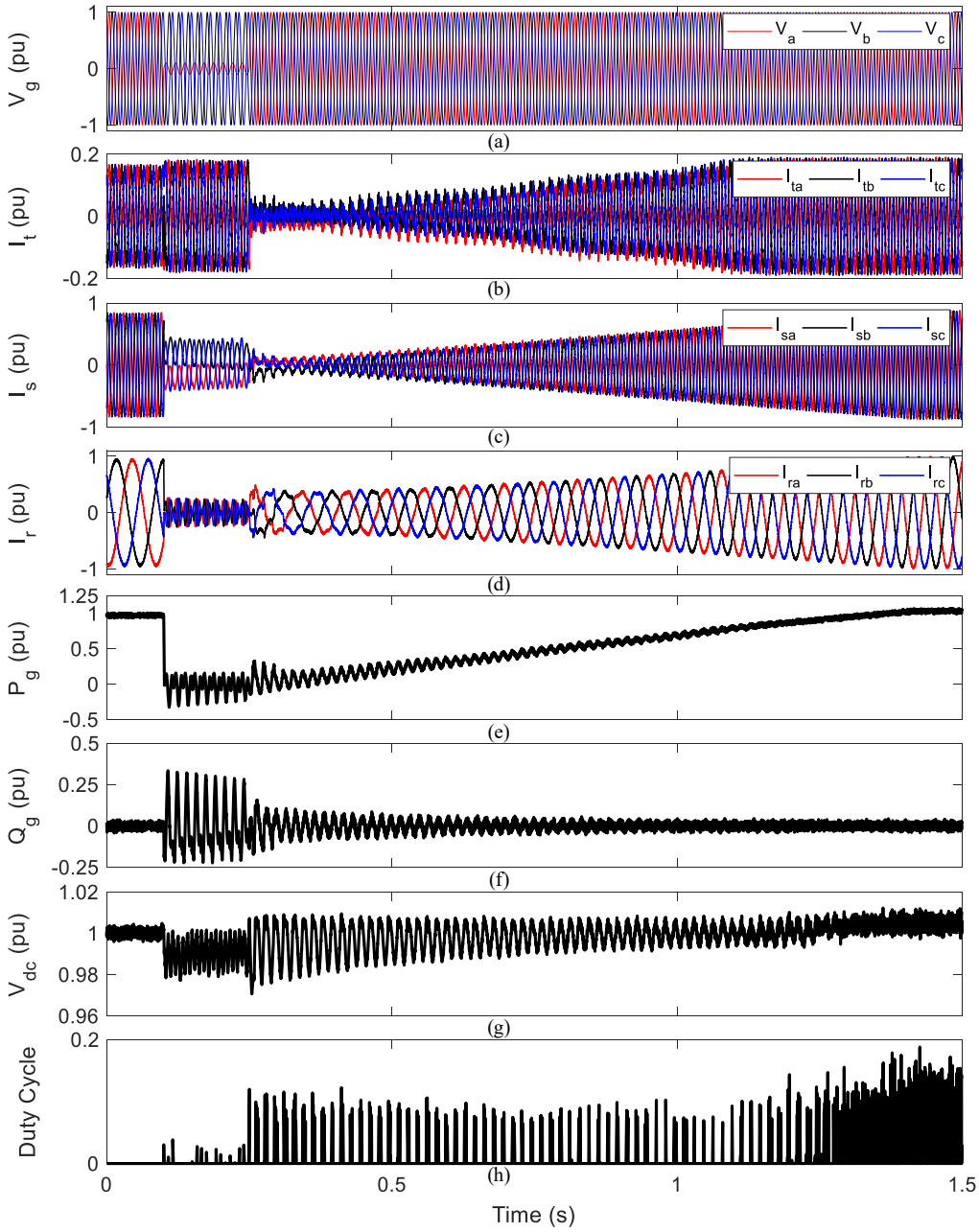

Fig. 4.13. The SRCB LVRT electrical simulation results under asymmetrical voltage dips to 0.1 pu with.

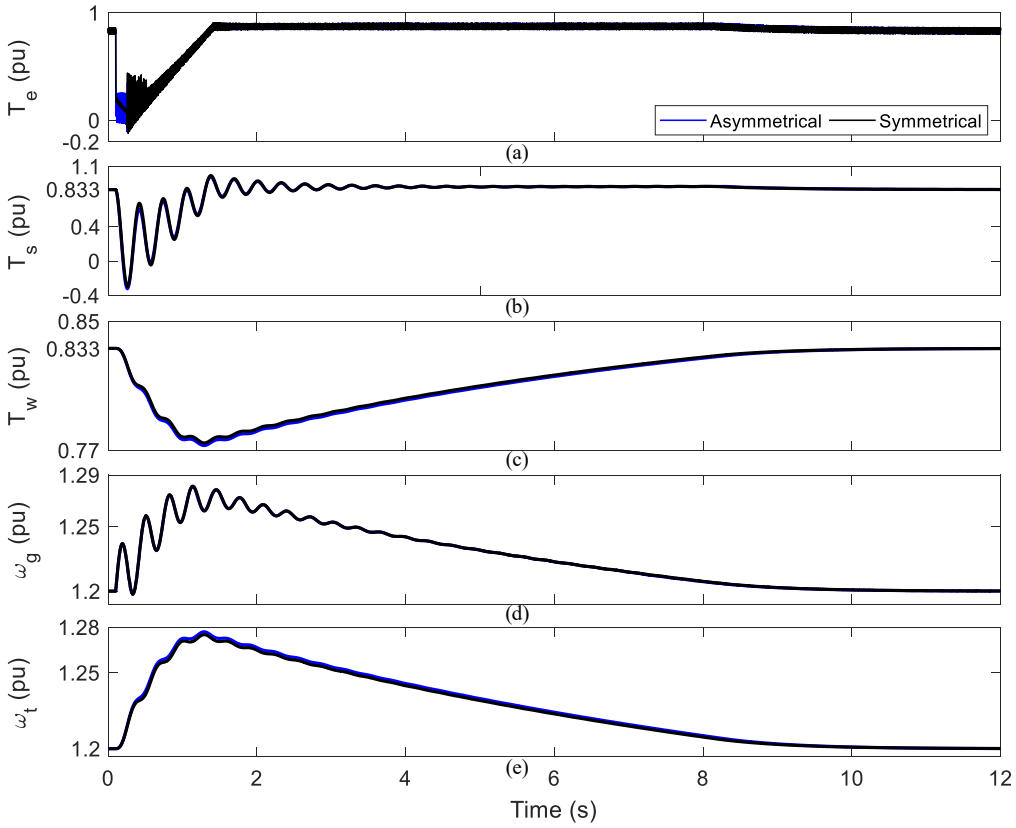

Fig. 4.14. The SRCB LVRT mechanical simulation results under asymmetrical (blue) and symmetrical (black) voltage dips to 0.1 pu.

Compared to the previous two methods, the dynamics under symmetrical and asymmetrical voltage dips are similar because the SRBC method can maintain the rotor current closer to the zero-current reference value for both types of voltage dips. The DFIG's mechanical performance under the SRCB method slightly differs from the previous two methods because the SRCB reduces EM torque drop by damping the rotor and stator currents. So, under symmetrical voltage dips, the minimum shaft torque is only −0.294 pu. However, for asymmetrical voltage dips, the minimum shaft torque is much larger than the previous two methods at −0.321 pu because the rotor current is controlled closer to the zero with the addition series damping. The reason the shaft experiences more stress under asymmetrical faults is because the resulting EM torque reduces slightly faster. As a result, among the three LVRT methods, the SRCB method has the smallest shaft stress under symmetrical faults but has the largest shaft stress under asymmetrical faults. The SRCB will also store

energy in the rotor speed during the voltage dip and the power ramping causing the generator speed to accelerate to a maximum speed of approximately 1.28 pu. The generator speed accelerates the most with the SRCB because unlike the DCC and the RCB method, the EM torque does not rapidly increase when the grid voltage is restored, which slightly decelerates the generator speed.

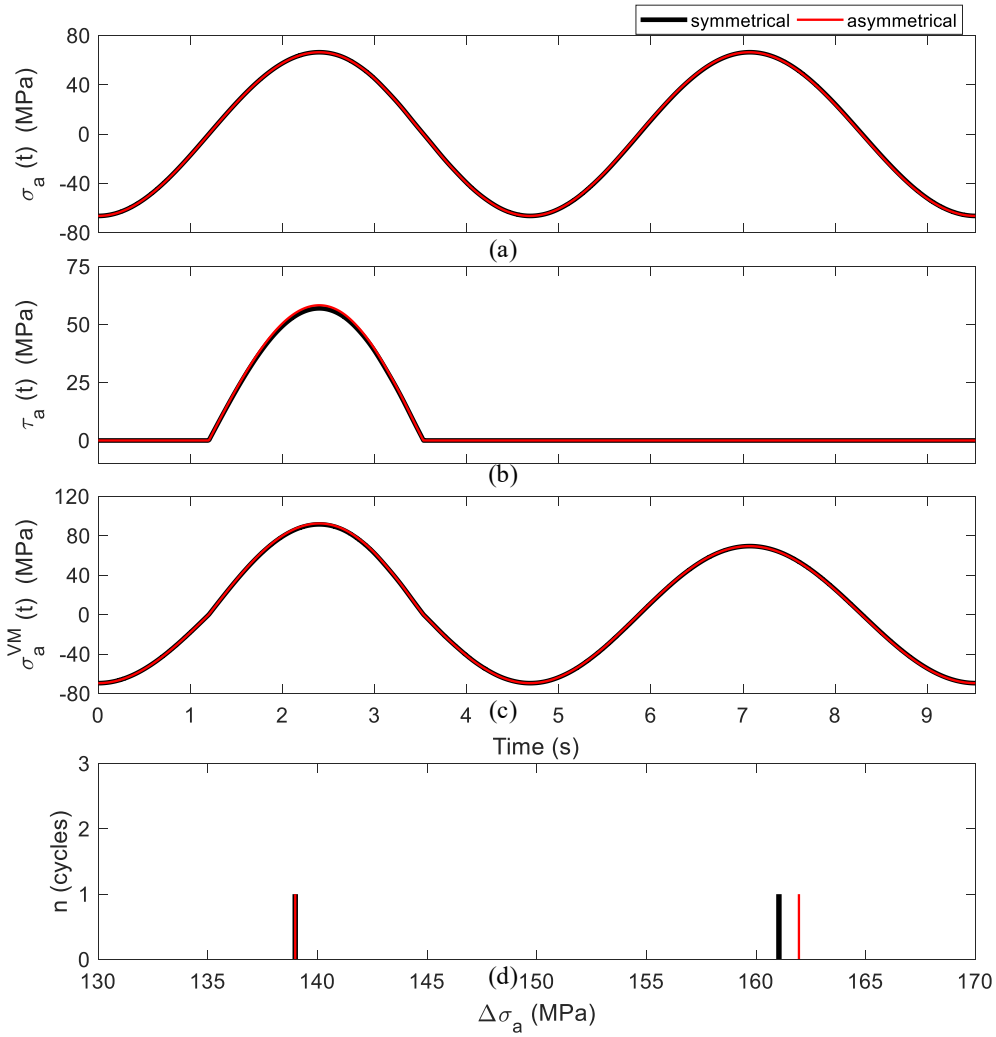

Fig. 4.15. The alternating bending stress, the alternating torque stress, the maximum von Mises stress, and the resultant rainflow count histogram using the RCB LVRT method.

Using the shaft torque simulation results for the SRCB LVRT method, the maximum alternating torsional stress are 57.0 MPa and 58.3 MPa, and the resulting maximum von Mises's stress are 91.6 MPa and 92.5 MPa for symmetrical and one-phase voltage dips, respectively. For symmetrical voltage dip conditions, RFC

yields one stress cycle with a stress range of 139 MPa and another stress cycle with a stress range of 161 MPa. For one-phase voltage dips, the stress cycle counting yields one stress cycle with a stress range of 139 MPa and one stress cycle with a stress range of 162 MPa. Applying Palmgren-Miner's rule yields an accumulated damage of 7.725×10^{-6}% and a reduction of the shaft lifetime of 32.0 s for symmetrical voltage dips. For one-phase voltage dips, the accumulated damage is 8.177×10^{-6}% and the shaft's lifetime reduction is 33.9 s.

4.5 Summary

The control and simulation results of the DCC with machine flux weakening, the RCB, and the SRCB DFIG LVRT solutions has been evaluated in this chapter. The standalone DCC method with the machine flux weakening has the largest DC-link overvoltage and RSC overcurrent because the response time of the machine flux weakening control is not fast enough to mitigate the rotor fault currents. The RCB decreases the RSC overcurrent by preventing the rotor fault current from entering the RSC, which also improves the DC-link performance. The SRCB provides the best WECS overcurrent protection and the best DC-link overvoltage protection. In terms of mechanical performance, all of the presented DFIG LVRT methods have resulted in mechanical transients. The mechanical performance of the three LVRT method are similar under symmetrical voltage dip conditions with the SRCB having slightly smaller shaft torque reduction. However, under asymmetrical conditions, the shaft torque reduction is lessened for the DCC and RCB, but the shaft torque for SRCB is nearly identical to the symmetrical case resulting in the largest mechanical stress.

Chapter 5

LVRT performances comparison between of DFIG and PMSG

5.1 Introduction

The PMSG and the DFIG are both popular variable speed WT with different advantages and disadvantages. The main advantage of the DFIG is that most of the generated power is transferred through the stator winding, so only a partially rated WECS is needed to interface the rotor winding to the grid, which increases efficiency and reduces converter cost. However, the direct stator to grid connection means that grid voltage disturbances will cause a transient response in the stator and rotor inducing large overcurrents. In contrast, the PMSG has a fully rated WECS, where the DC-link decouples the dynamics of the stator from the grid. The disadvantage of the PMSG are that they are usually more expensive because of the large permanent magnets and that the fully rated WECS results in increased converter cost and increased switching loss. Because of the PMSG and DFIG have different features, it will be meaningful to compare the two under grid transients to understand whether the PMSG's advantage of having decoupled machine and grid dynamics outweighs the increased cost and reduced efficiency.

This chapter compares the LVRT electrical and mechanical performance of the PMSG and the DFIG using the LVRT simulation results provided in the previous two chapters. As a reminder, the PMSG LVRT methods consists of the DCC, the SEIRI, and the hybrid method. For the DFIG, the LVRT methods that has been studied are the DCC with machine flux weakening, the RCB, and the SRCB. To compare the mechanical performance of the two types of WT, the two WTs have identical power output and turbine rotor speed. The electrical performance of the

two types of WTs are compared using the metrics of the WECS overcurrent and the DC-link overvoltage. To compare the mechanical performance, the metrics used are the reduction in the shaft torque and the acceleration of the generator speed. Tables 5.1 and 5.2 summarizes the electrical and mechanical simulation results under symmetrical and asymmetrical faults, respectively. Finally, the shaft life reduction caused by each LVRT of the PMSG and DFIG will also be compared.

5.2 Electrical system performance comparison

For the PMSG, the DCC method does not result in DC-link overvoltage under both symmetrical and one-phase faults because the response time of the DCC is fast enough to match the grid current response preventing charging of the DC-link. The SEIRI method reduces the stator power to match the grid power by reducing the q-axis stator current; however, the stator current response time is slower than the grid current, so the difference in the stator and grid power will charge the DC-link. As such, the SEIRI method results in the largest DC-link overvoltage at 11% and 6.3% under symmetrical and one-phase voltage dips, respectively. The hybrid method mitigates the DC-link overvoltage to 5% and 2.8% for symmetrical and one-phase voltage dips by using the DCC to absorb a portion of the transient power difference caused by the SEIRI method.

For the DFIG, the DCC with the machine flux weakening LVRT method results in the largest DC-link overvoltage at 5.7% and 4.8% under symmetrical and one-phase voltage dips, respectively. As a result of the stator voltage suddenly dropping, the rotor power will spike drastically charging the DC-link. Although the DCC dissipates some of the power, the response time of the DCC is not fast enough, so the DC-link will still be slightly charged. The RCB method redirects the large rotor fault currents from entering the RSC preventing the fault current from charging the DC-link. This helps reduce the DC overvoltage down to 2.9% and 2.8% for symmetrical and one-phase faults, respectively. In contrast, the SRCB method does not result in DC-link overvoltage under both symmetrical and one-phase faults because RSC is shorted when the rotor current is larger than its reference, which means the rotor power cannot enter the RSC to charge the DC-link. And since the

RSC closes at the start of the voltage dip, the DC-link will discharge because of the grid current response time.

Table 5.1 Summary of PMSG and DFIG simulation results under symmetrical voltage dips to 0.1 pu

Wind Turbine	LVRT Method	WECS Overcurrent	DC Overvoltage	Shaft Torque Reduction	Generator Speed Acceleration
DFIG	DCC	200.7%	5.67%	137.7%	6.59%
	RCB	31.3%	2.87%	144.0%	6.73%
	SRCB	–	–	135.3%	6.78%
PMSG	DCC	–	–	–	–
	SEIRI	–	11.0%	161.9%	7.41%
	Hybrid	–	4.98%	139.7%	6.56%

Table 5.2 Summary of PMSG and DFIG simulation results under one-phase voltage dips to 0.1 pu

Wind Turbine	LVRT Method	WECS Overcurrent	DC Overvoltage	Shaft Torque Reduction	Generator Speed Acceleration
DFIG	DCC	119.3%	4.81%	110.6%	5.93%
	RCB	9.8%	2.76%	107.9%	5.86%
	SRCB	–	–	138.5%	6.87%
PMSG	DCC	–	–	–	–
	SEIRI	–	6.28%	161.3%	7.38%
	Hybrid	–	2.76%	139.7%	6.54%

Table 5.3 Summary of the average EM torque performance under each LVRT method

Wind Turbine	LVRT Method	Minimum EM Torque	Time of Min EM torque
DFIG	DCC	99.40%	143.3ms
	RCB	99.60%	145.5ms
	SRCB	91.40%	142.8ms
PMSG	DCC	–	–
	SEIRI	162.50%	8.73ms
	Hybrid	116.70%	80.23ms

For the PMSG, none of the LVRT method will result in overcurrent of the WECS, but for inertia-based LVRT, the WECS must be slightly overrated to allow the stored rotational energy to be transferred back to the grid. In contrast, the DFIG will have overcurrent on the WECS because the stator voltage drops result in severe rotor fault currents. The DCC with the machine flux weakening LVRT method has the largest overcurrent on the RSC at 200% and 119% for symmetrical and asymmetrical fault, respectively. As mentioned previously, the RCB LVRT method diverts the large rotor fault current from the RSC, so the overcurrent has been reduced to 31.3% and 9.8% for symmetrical and one-phase faults, respectively. The SRCB LVRT method does not result in overcurrent because the SRCB provides additional damping, which will quickly reduce the rotor current.

From this comparison, the PMSG has far superior dynamic electrical performance than the DFIG. The standalone DCC method has been shown for both types of WTs, but the DCC has far better DC-link protection for the PMSG than for the DFIG. For the PMSG, the DCC provides all the needed protection to prevent DC-link voltage; however, for the DFIG, the standalone DCC will causes charging of the DC-link and major WECS overcurrent. The isolation between the generator and grid dynamics even allows for the hardware-less SEIRI method to be viable for the PMSG. If the overvoltage of the DC-link caused by the SEIRI method is a concern, the hybrid method can be used with smaller crowbar to reduce the transient DC-link charging. In general, the DFIG will require additional hardware to be attached to the rotor winding to prevent overcurrent, such as the RCB and SRCB.

5.3 Mechanical system performance comparison

The mechanical performance of the PMSG under symmetrical and asymmetrical faults are nearly identical because the average EM torque are almost the same. The DCC method has no impact on the mechanical system because the machine dynamics are isolated and the MSC preserves MPPT. The SEIRI method has the most mechanical stress with a 162% shaft torque reduction and a 7.4% generator speed acceleration because the EM torque is drastically reduced to match the stator power with the grid power. The hybrid method splits the reduction of the

full EM torque into two part, which reduces the mechanical stress to 140% shaft torque reduction and the generator speed acceleration to 6.6%.

For the DFIG, all three LVRT methods stores power in the rotor's speed because the EM torque is reduced when controlling the rotor current to zero. This causes the shaft torque to dip and rotor speed to accelerates like the inertia-based PMSG LVRT methods. For the DFIG under symmetrical faults, the shaft torque reductions are 138%, 145%, and 135%, and the generator speed accelerations are 6.6%, 6.7%, and 6.8% for the DCC, the RCB, and the SRCB methods, respectively. And under asymmetrical faults, the shaft torque reductions are reduced to 111%, 108%, and the generator speed accelerations are lessened to 5.9%, 5.9%, for the DCC and the RCB, respectively. For the SRCB under one-phase voltage, the shaft torque and generator speed acceleration are like the symmetrical case at 139% and 6.9%, respectively.

The DCC and the RCB method have similar mechanical performances because its rotor current dynamics are similar. Under the DCC and the RCB LVRT, the symmetrical and asymmetrical faults result in different mechanical performances because under one-phase voltage dips, the oscillation in the rotor and stator current results in a less severe drop in the EM torque. However, for the SRCB, the additional series damping allows the rotor current to have similar current dynamics under both symmetrical faults and asymmetrical faults; therefore, the mechanical performances will be alike as well. Therefore, the shaft torque reduction under asymmetrical faults using the SRCB is much larger than the other two methods.

Although the DFIG has severe transients in both the stator and rotor currents, the resultant EM torque of the DFIG does not reduce as significantly and rapidly compared to the SEIRI method. For example, when using the SEIRI method, the EM torque rapidly dips down by 162.5% after 8.73 ms. Whereas, when using the RCB method under symmetrical faults, the torque dips by 99.6% after 145.5 ms. Therefore, DFIG LVRT method generally has less shaft torque reduction than the SEIRI LVRT methods.

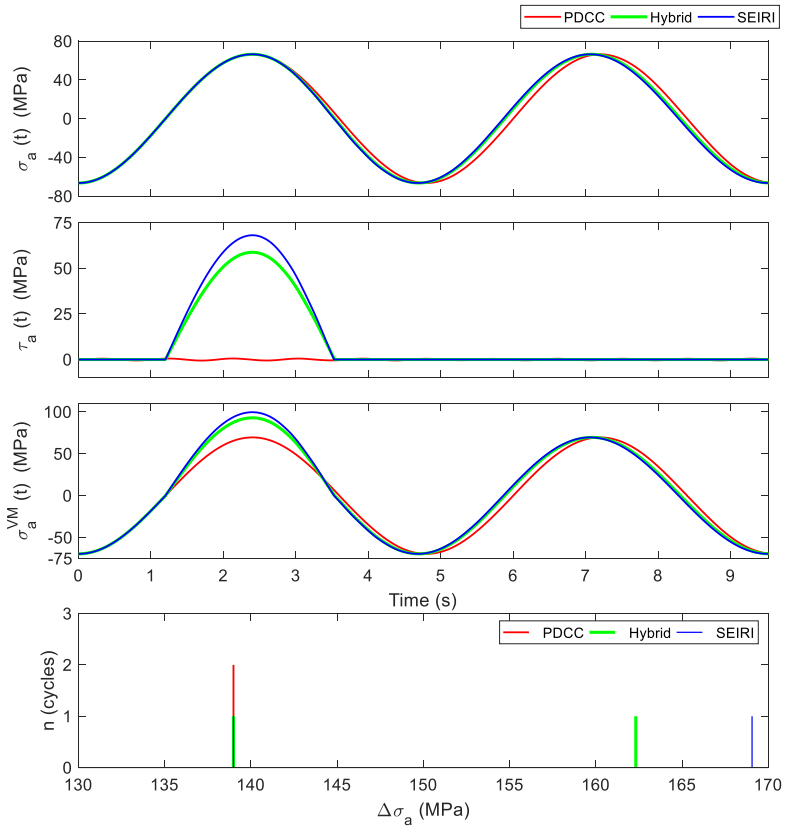

Fig. 5.1. The alternating bending stress, the alternating torque stress, the maximum von Mises stress, and the resultant rainflow count histogram using the DCC (red), the SEIRI (blue), and the hybrid (green) PMSG LVRT methods.

To compare the stress life impact of each method, the stress diagrams for each method, from the previous two chapters, are superimposed in Figs. 5.1-5.3. And the damage percentages and shaft life reductions for each PMSG and DFIG LVRT method are summarized in Table 5.4. Among the DFIG LVRT methods, the RCB method has the largest reduction in the shaft torque at 99.6%, which results in the largest shaft life reduction of 37.49 s. The SRCB method results in lowest shaft torque reduction at 91.4% meanings the shaft life reduction will be the lowest at 32.01 s. However, under one-phase voltage dips, the SRCB now has the largest shaft life reduction of 33.89 s because the shaft torque responses under the SRCB LVRT method are nearly identical under symmetrical and one-phase voltage dips to 0.1 pu. Among the presented LVRT methods between the PMSG and the DFIG, the shaft life reduction is the largest using the SEIRI method with an estimated lifetime reduction of 53 s because the SEIRI method has the largest shaft torque

reduction at 161%. The DCC method has the smallest shaft life reduction at 9.6 s, which is equal to the duration of the two stress cycles under normal operations because the DCC method does not impact the mechanical system. The hybrid method reduces the shaft torque reduction of the SEIRI method by splitting the EM torque reduction into two parts, which mitigates the shaft life reduction of the standalone SEIRI method from 53 s to 34.65 s.

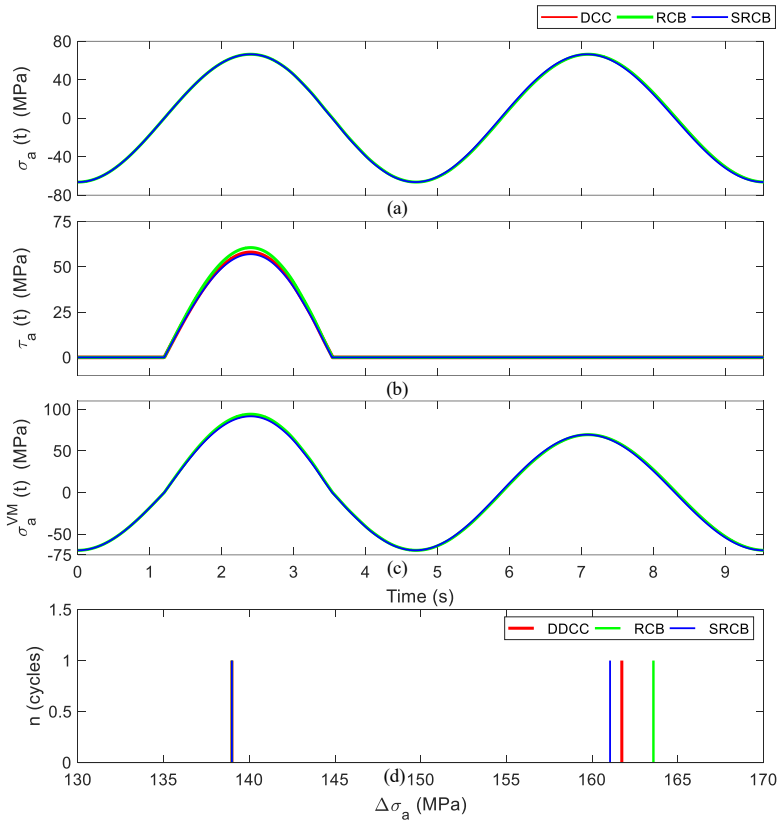

Fig. 5.2. The alternating bending stress, the alternating torque stress, the maximum von Mises stress, and the resultant rainflow count histogram using the DCC (red), the RCB (green), and the SRCB (blue) DFIG LVRT methods under symmetrical faults.

Table 5.4 Accumulated shaft damage and shaft life reduction over 9.6 s

Wind Turbine	Fault Type	LVRT Method	Shaft Damage (%)	Shaft Life Reduction (s)
DFIG	Symmetrical	DCC	8.06×10^{-6}	33.41
		RCB	9.05×10^{-6}	37.49
		SRCB	7.72×10^{-6}	32.01
	One-phase	DCC	5.14×10^{-6}	21.32
		RCB	4.94×10^{-6}	20.48
		SRCB	8.18×10^{-6}	33.89
PMSG	Symmetrical	DCC	2.32×10^{-6}	9.60
		SEIRI	1.28×10^{-5}	53.00
		Hybrid	8.36×10^{-6}	34.65

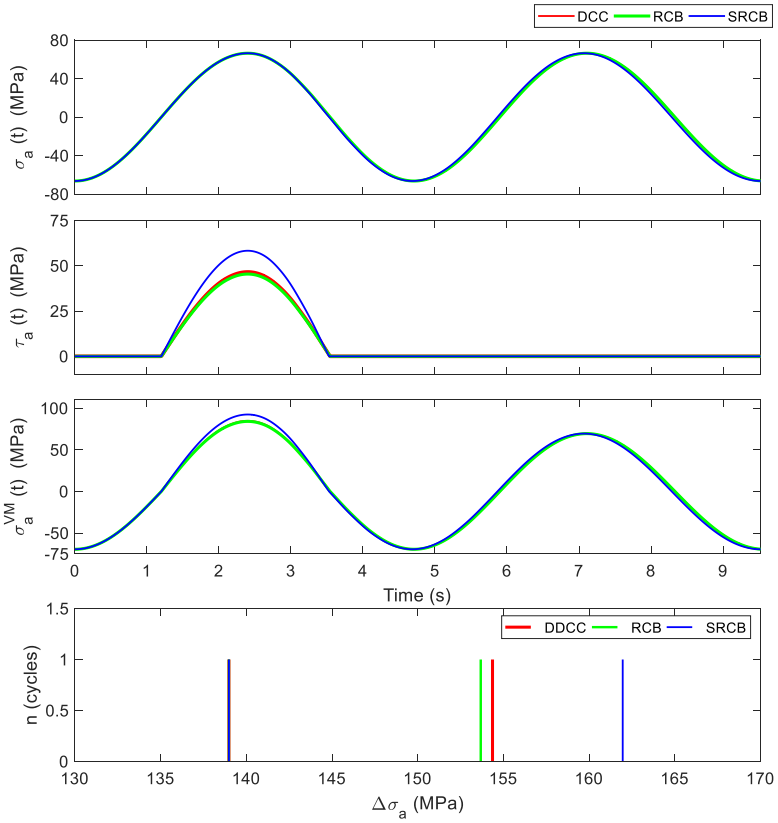

Fig. 5.3. The alternating bending stress, the alternating torque stress, the maximum von Mises stress, and the resultant rainflow count histogram using the DCC (red), the RCB (green), and the SRCB (blue) DFIG LVRT methods under asymmetrical faults.

5.4 Summary

In this chapter, the electrical and mechanical performance of the DFIG and PMSG under each LVRT are compared. For the PMSG, the LVRT methods that has been investigated are the DCC, the SEIRI, and the hybrid methods. And for the DFIG, the LVRT methods that has been analyzed are the DCC with the machine flux weakening, the RCB, and the SRCB methods. Based on the comparison, the PMSG has better dynamic performance than the DFIG, and the DCC method provides the best electrical and mechanical performance for the PMSG. From the comparison of the lifetime impact on the drivetrain's main shaft, the SEIRI method results in the largest reduction in the main shaft's lifetime because it has the largest reduction in the shaft torque. In addition, it has been shown that the hybrid method can help reduce the damage on the main shaft by softening the EM torque reduction.

Chapter 6

Conclusion and Future Work

The main objective of this thesis is to evaluate and compare the stress-life impact of the PMSG and the DFIG LVRT methods to provide wind farm owners and WT manufacturers a more informed decisioned when deciding which LVRT solution and which type of WT is more suitable for their investment. The OMC of WTs covers a large fraction of the capital investment of the wind farms. Therefore, minimizing the damage on WT parts is essential to maximize the profitability of WTs. The LVRT solutions that have been considered for the PMSG are the DCC hardware-based solution, the SEIRI control-based solution, and the hybrid combination of the two. For the DFIG, all the studied LVRT methods require additional hardware, which are the DCC with the machine flux weakening, the RCB, and the SRCB. The electrical performance of these methods is evaluated by considering the overcurrent of the WECS and transmission lines and the overvoltage of the DC-link. The mechanical performance is conducted by analyzing the shaft torque reduction and the generator overspeed and by performing lifetime analysis on the main shaft of the WT.

6.1 Conclusion

The conclusions of this thesis are presented as follows

- Three PMSG LVRT methods were investigated in Chapter 3. The first and most common LVRT solution was the DCC method, which attached a chopper circuit to the DC-link to dissipate the excess generator power during LVRT. The second method was the control-based SEIRI method that was proposed by the research community to eliminate the need for additional hardware while preventing DC-link overvoltage through controlling the DC-link voltage using the MSC. The final method was the hybrid, which combined the SEIRI and the

DCC method by operating the DCC using open-loop control. The main purpose of the hybrid method was to use a smaller DCC to enhance the existing electrical and mechanical performance of the SEIRI. From the simulation of these three LVRT method, it had been shown that the DCC provided the best performance electrical performance because it had fast response time and was capable of preventing the DC-link from increasing beyond its rated value under both symmetrical and asymmetrical voltage dips. By default, the DCC had the best mechanical performance because the DCC did not alter the dynamics of the mechanical system. The SEIRI had the worst electrical performance because the response time of the stator current was much slower than that of the grid current, which would result in charging of the DC-link when the stator power was much greater than the grid power. The SEIRI method also had the poorest mechanical performance because to regulate the DC-link voltage with MSC, the stator power and therefore the EM torque must be reduced, which induced a mechanical transient on the drive-train system. In this thesis, the hybrid was utilized to soften the reduction of the EM torque of the SEIRI method by reducing the EM torque in two steps. This resulted in a smaller transient in the mechanical system, which reduced the stresses on the drivetrain. In addition, the hybrid improved the DC-link overvoltage by having the DCC absorb a portion of the transient power resulting from the slower stator current dynamics of the SEIRI method.

- In chapter 4, the three presented DFIG LVRT solutions had also been evaluated. The first method was the DCC with machine flux weakening, which used a DC chopper circuit to mitigate DC-link overvoltage and reduced the overcurrent of the RSC by controlling the rotor current to zero. The RCB was most conventionally used LVRT method, which attached a crowbar circuit on the rotor winding to redirect large rotor fault currents. The RCB was paired with the DCC to provide better DC-link voltage protection. Lastly, the SRCB was a more recently proposed DFIG LVRT solution, which connected a crowbar circuit in series with the rotor winding. Under normal operations, the SRCB was closed, which bypassed the paralleled crowbar resistors. However, during a

voltage dip, the SRCB opened and the RSC shorted itself, which damped the rotor current and dissipated the rotor power. The standalone DCC method with machine flux weakening had worst electrical performance with the most severe DC-link overvoltage and RSC overcurrent because the flux weakening was not effective enough to mitigate the rotor fault currents, which ended up charging the DC-link. The RCB enhanced the DFIG LVRT performance significantly by preventing the rotor fault current from entering the RSC, which as a result also improved the DC-link performance. However, both previously mentioned methods did not prevent the stator fault currents from entering the transmission system. Therefore, the SRCB showed the best electrical performance. By damping the rotor winding current with the SRCB, the stator current would also be damped because of the coupling between the rotor and stator winding, which removed the risk of the stator fault current entering the transmission system. The SRCB also provided better WECS overcurrent protection and DC-link overvoltage protection than the RCB. For the DFIG, all the presented LVRT method resulted in mechanical transients. From the simulation results, the mechanical performance of the three LVRT method were similar under symmetrical voltage dip conditions, but the SRCB was slightly better with smaller shaft torque reduction. Under asymmetrical conditions, for the standalone DCC and RCB, the shaft torque reduction was lessened because the stator and rotor current oscillation resulted in a slower reduction of the EM torque. However, with the SRCB, the damping provided by the SRCB mitigated the rotor current oscillation, which resulted in similar EM torque reduction as the symmetrical fault case. As a result, the SRCB had the largest mechanical stress under asymmetrical fault conditions.

- The performances of the DFIG and PMSG were compared in chapter 5. To compare the electrical performance of the LVRT methods, the WECS overcurrent and the DC-link overvoltage were evaluated in relative to their normal operation values. Similarly, the relative shaft torque reduction and generator speed acceleration were used to compare the mechanical performances. From the electrical comparison between the PMSG and DFIG,

the PMSG had much better dynamic performance than the DFIG. The DFIG resulted in severe fault currents during a voltage dip; however, for the PMSG, the machine dynamics were not impacted directly by the grid voltage dip, but instead caused by LVRT solutions that required storing power in the rotor's inertia. For example, when using the DCC LVRT solution for the PMSG, there were no visible changes in the PMSG's machine side dynamics. But using the same solution for the DFIG, large stator and rotor fault currents appeared despite the attempt to reduce these currents through control. Because of the superior dynamic performance of the PMSG even the hardware-less SEIRI LVRT solution was possible from an electrical standpoint. From the mechanical performance comparison among the LVRT solutions, the SEIRI method resulted in the most severe shaft torque reduction and largest acceleration in the generator's speed. Interestingly, despite the severe overcurrent that occurred for DFIG, the EM torque did not reduce as much as it did for the PMSG. After performing lifetime analysis of the WT's main shaft, the SEIRI LVRT method resulted in the most accumulated damage on the shaft because it had the largest shaft torque reduction. It had been also demonstrated that by lessening the shaft torque reduction with the hybrid method, the amount of accumulated damage that the shaft experienced could be significantly reduced.

6.2 Future Work

The future works of this thesis are the following: the mechanical stress analysis of the drivetrain gearbox, the use of finite element analysis to provide a more precise analysis of the lifetime impact of each LVRT method, and the comparison of the WECS topologies on LVRT performance.

1) Mechanical stress analysis of the gearbox

This thesis has investigated the impact of the LVRT on the mechanical stress of the main shaft of the drivetrain, but another component that is under stress from mechanical transient is the gearbox. The majority of the WT's OMC is caused by the gearbox because the gearbox is the most expensive component of the drivetrain and the most prone component to malfunction [33]. Therefore, it is important to

analyze the impact of various types of LVRT solutions on the gearbox's lifespan from a financial standpoint.

2) Finite element analysis of the main shaft

Finite element analysis (FEA) is the simulation of physical phenomenon using mathematical modelling and is the one of the most accepted method to performing structural analysis [42]. Ansys nCode DesignLife can be used on the results from FEA to calculate stresses and strains, and then determine the cumulated damage from repetitive loading [43]. This thesis approximates the lifetime impact of the main shaft using classical stress life analysis using RFC, but FEA can provide a more realistic stress life analysis that will be accepted by industrial standards.

3) Investigating the impact of the WECS topology on LVRT performance

Although the two-level VSC is the traditionally used for WECS, the multi-level VSC topologies, the CSC topologies, and the matrix converters are becoming more mature and can be popular options for WECS with various benefits. The two-level VSC is used exclusively in this thesis to compare the performance each LVRT method. Therefore, a future work of this project can be to subject different types of WECS topology to various types of LVRT solutions to understand the benefits of each topology under transient conditions.

References

[1] Global Wind Energy Council (GWEC), Wind Report, 2018. [Online]. Available: https://gwec.net/51-3-gw-of-global-wind-capacity-installed-in-2018/

[2] "Advantages and Challenges of Wind Energy", Energy.gov, 2020. [Online]. Available: https://www.energy.gov/eere/wind/advantages-and-challenges-wind-energy.

[3] "Wind power - Energy Education", Energyeducation.ca, 2020. [Online]. Available: https://energyeducation.ca/encyclopedia/Wind_power.

[4] A. Junyent-Ferr, Y. Pipelzadeh and T. C. Green, "Blending HVDC-Link Energy Storage and Offshore Wind Turbine Inertia for Fast Frequency Response," in *IEEE Transactions on Sustainable Energy*, vol. 6, no. 3, pp. 1059-1066, July 2015

[5] M. Liserre, R. Cárdenas, M. Molinas and J. Rodriguez, "Overview of Multi-MW Wind Turbines and Wind Parks," in *IEEE Transactions on Industrial Electronics*, vol. 58, no. 4, pp. 1081-1095, April 2011

[6] Zhou Peng and He Yikang, "Control strategy of an active crowbar for DFIG based wind turbine under grid voltage dips," *2007 International Conference on Electrical Machines and Systems (ICEMS)*, Seoul, 2007, pp. 259-264.

[7] V. Yaramasu, A. Dekka, M. J. Durán, S. Kouro and B. Wu, "PMSG-based wind energy conversion systems: survey on power converters and controls," in *IET Electric Power Applications*, vol. 11, no. 6, pp. 956-968, 7 2017.

[8] A. Calle-Prado, S. Alepuz, J. Bordonau, P. Cortes and J. Rodriguez, "Predictive Control of a Back-to-Back NPC Converter-Based Wind Power System," in *IEEE Transactions on Industrial Electronics*, vol. 63, no. 7, pp. 4615-4627, July 2016.

[9] L. Shi, S. Sun, L. Yao, Y. Ni and M. Bazargan, "Effects of wind generation intermittency and volatility on power system transient stability," in *IET Renewable Power Generation*, vol. 8, no. 5, pp. 509-521, July 2014

[10] V. Yaramasu, B. Wu, S. Alepuz and S. Kouro, "Predictive Control for Low-Voltage Ride-Through Enhancement of Three-Level-Boost and NPC-Converter-Based PMSG Wind Turbine," in *IEEE Transactions on Industrial Electronics*, vol. 61, no. 12, pp. 6832-6843, Dec. 2014.

[11] S. Alepuz, A. Calle, S. Busquets-Monge, S. Kouro and B. Wu, "Use of Stored Energy in PMSG Rotor Inertia for Low-Voltage Ride-Through in Back-to-Back NPC Converter-Based Wind Power Systems," in *IEEE Transactions on Industrial Electronics*, vol. 60, no. 5, pp. 1787-1796, May 2013.

[12] K. Kim, Y. Jeung, D. Lee and H. Kim, "LVRT Scheme of PMSG Wind Power Systems Based on Feedback Linearization," in *IEEE Transactions on Power Electronics*, vol. 27, no. 5, pp. 2376-2384, May 2012.

[13] R. A. Ibrahim, M. S. Hamad, Y. G. Dessouky and B. W. Williams, "A review on recent low voltage ride-through solutions for PMSG wind turbine," *International Symposium on Power Electronics Power Electronics, Electrical*

[14] P. Xing, L. Fu, G. Wang, Y. Wang and Y. Zhang, "A compositive control method of low-voltage ride through for PMSG-based wind turbine generator system," in *IET Generation, Transmission & Distribution*, vol. 12, no. 1, pp. 117-125, 2 1 2018.

[15] M. Wang, Y. Tian, X. Feng and G. Chen, "A hybrid LVRT control scheme for PMSG wind power system," *Proceedings of The 7th International Power Electronics and Motion Control Conference*, Harbin, 2012, pp. 1173-1177.

[16] A. M. A. Haidar, K. M. Muttaqi and M. T. Hagh, "A Coordinated Control Approach for DC link and Rotor Crowbars to Improve Fault Ride-Through of DFIG-Based Wind Turbine," in *IEEE Transactions on Industry Applications*, vol. 53, no. 4, pp. 4073-4086

[17] D. Xie, Z. Xu, L. Yang, J. Østergaard, Y. Xue and K. P. Wong, "A Comprehensive LVRT Control Strategy for DFIG Wind Turbines With Enhanced Reactive Power Support," in *IEEE Transactions on Power Systems*, vol. 28, no. 3, pp. 3302-3310

[18] J. Liang, W. Qiao and R. G. Harley, "Feed-Forward Transient Current Control for Low-Voltage Ride-Through Enhancement of DFIG Wind Turbines," in *IEEE Transactions on Energy Conversion*, vol. 25, no. 3, pp. 836-843

[19] Z. Zou, J. Liao, Y. Lei, Z. Mu and X. Xiao, "Postfault LVRT Performance Enhancement of DFIG Using a Stage-Controlled SSFCL-RSDR," in *IEEE Transactions on Applied Superconductivity*, vol. 29, no. 2, pp. 1-6

[20] J. Vidal, G. Abad, J. Arza and S. Aurtenechea, "Single-Phase DC Crowbar Topologies for Low Voltage Ride Through Fulfillment of High-Power Doubly Fed Induction Generator-Based Wind Turbines," in *IEEE Transactions on Energy Conversion*, vol. 28, no. 3, pp. 768-781

[21] M. F. M. Arani and Y. A. I. Mohamed, "Assessment and Enhancement of a Full-Scale PMSG-Based Wind Power Generator Performance Under Faults," in *IEEE Transactions on Energy Conversion*, vol. 31, no. 2, pp. 728-739, June 2016.

[22] D. R. Joshi and S. H. Jangamshetti, "A Novel Method to Estimate the O&M Costs for the Financial Planning of the Wind Power Projects Based on Wind Speed—A Case Study," in *IEEE Transactions on Energy Conversion*, vol. 25, no. 1, pp. 161-167, March 2010.

[23] L. Yang, Z. Xu, J. Ostergaard, Z. Y. Dong and K. P. Wong, "Advanced Control Strategy of DFIG Wind Turbines for Power System Fault Ride Through," in *IEEE Transactions on Power Systems*, vol. 27, no. 2, pp. 713-722

[24] S. Xiao, G. Yang, H. Zhou and H. Geng, "An LVRT Control Strategy Based on Flux Linkage Tracking for DFIG-Based WECS," in *IEEE Transactions on Industrial Electronics*, vol. 60, no. 7, pp. 2820-2832

[25] S. B. Naderi, M. Negnevitsky and K. M. Muttaqi, "A Modified DC Chopper for Limiting the Fault Current and Controlling the DC-Link Voltage to Enhance Fault Ride-Through Capability of Doubly-Fed Induction-Generator-Based Wind Turbine," in *IEEE Transactions on Industry Applications*, vol. 55, no. 2, pp. 2021-2032

[26] M. Abdelrahem, M. H. Mobarak and R. Kennel, "Model predictive control for low-voltage ride through capability enhancement of DFIGs in variable-speed

wind turbine systems," *2016 9th International Conference on Electrical and Computer Engineering (ICECE)*, Dhaka, 2016, pp. 70-73.

[27] Z. Xu and Z. Pan, "Influence of different flexible drive train models on the transient responses of DFIG wind turbine," *2011 International Conference on Electrical Machines and Systems*, Beijing, 2011, pp. 1-6.

[28] P. Ashwini, and Thosar Archana, "Mathematical modeling of wind energy system using two mass model including generator losses." *International J. Emerg. Trends Electr. Electron 12*, 2016, pp. 18-23.

[29] J. Licari, C. Ugalde-Loo, J. Liang, J. Ekanayake, and N. Jenkins. (2012). "Torsional Damping Considering both Shaft and Blade Flexibilities", *Wind Engineering*, vol. 36. pp. 181-196

[30] Y. Guo, T. Parsons, K. Dykes and R. King, "A systems engineering analysis of three-point and four-point wind turbine drivetrain configurations", *Wind Energy*, vol. 20, no. 3, pp. 537-550, 2016.

[31] Budynas, R., Nisbett, J. and Shigley, J. (n.d.). *Shigley's mechanical engineering design*, *9th ed* Mc Graw Hill: 2010.

[32] D. Ion, "The Equivalent Stress Concept in Multiaxial Fatigue," in *Journal of Engineering Studies and Research*, vol. 17, no. 2, pp. 53-62, 2011

[33] J. Berglind, "Fatigue-Damage Estimation and Control for Wind Turbines", PhD thesis, Aalborg University, 2015

[34] Y. Lee and T. Tjhung, "Rainflow Cycle Counting Techniques", in *Metal fatigue analysis handbook*, Y. Lee, M. Barkey and H. Kang, Ed. Waltham, MA: Butterworth-Heinemann, 2012.

[35] *Guideline for the Certification of Wind Turbines*, Germanischer Lloyrd, 2010

[36] B. Wu, Y. Lang, N. Zargari and S. Kouro, "Wind Generators and Modelling," in *Power Conversion and Control of Wind Energy Systems*, IEEE, 2011, pp.1-23

[37] A.Yazdani; R. Iravani, "Voltage-Sourced Converters in Power Systems: Modeling, Control, and Applications" , 1, Wiley-IEEE Press, 2010

[38] Y. Xia, K. H. Ahmed and B. W. Williams, "Wind Turbine Power Coefficient Analysis of a New Maximum Power Point Tracking Technique," in *IEEE*

Transactions on Industrial Electronics, vol. 60, no. 3, pp. 1122-1132, March 2013.

[39] M. Tsili and S. Papathanassiou, "A review of grid code technical requirements for wind farms," in *IET Renewable Power Generation*, vol. 3, no. 3, pp. 308-332, Sept. 2009.

[40] Dvorak, P., 2020. *Extreme Torsional Loads Damage More Than Wind Turbine Gearboxes*. [online] Windpower Engineering & Development. Available at: https://www.windpowerengineering.com/extreme-torsional-loads-damage-more-than-wind-turbine-gearboxes/

[41] J. Jonkman, S. Butterfield, W. Musial and G. Scott, "Definition of a 5-MW Reference Wind Turbine for Offshore System Development", National Renewable Energy Laboratory, Colorado, 2009.

[42] "Stress Concentration Factor Finder," eFatigue. [Online]. Available: https://www.efatigue.com/constantamplitude/stressconcentration/

[43] English, T., McFadden, C., McFadden, C., McFadden, C. and Papadopoulos, L., 2020. *Finite Element Analysis Is The Foundation Of All Mechanical Engineering Simulation*. [online] Available at: https://interestingengineering.com/what-is-finite-element-analysis-and-how-does-it-work#:~:text=Finite%20Element%20Analysis%20or%20FEA,a%20variety%20of%20other%20disciplines.

[44] Ansys.com. 2020. *Ansys Ncode Designlife: Product Fatigue Life Failure Prediction| Ansys*. [online] Available at: https://www.ansys.com/products/structures/ansys-ncode-designlife